Summer 2010

Multi-surface, multi-object optimal image segmentation: application in 3D knee joint imaged by MR

Yin Yin
University of Iowa

MULTI-SURFACE, MULTI-OBJECT OPTIMAL IMAGE SEGMENTATION: APPLICATION IN 3D KNEE JOINT IMAGED BY MR

by

Yin Yin

An Abstract

Of a thesis submitted in partial fulfillment of the
requirements for the Doctor of Philosophy degree
in Electrical and Computer Engineering
in the Graduate College of
The University of Iowa

July 2010

Thesis Supervisor: Professor Milan Sonka

ABSTRACT

A novel method called LOGISMOS – Layered Optimal Graph Image Segmentation of Multiple Objects and Surfaces – for simultaneous segmentation of multiple interacting surfaces belonging to multiple interacting objects is reported. The approach is based on representation of the multiple inter-relationships in a single n-dimensional graph, followed by graph optimization that yields a globally optimal solution.

Three major contributions for LOGISMOS are made and illustrated in this thesis: 1) multi-object multi-surface optimal surface detection graph design, 2) implementation of a novel and reliable cross-object surface mapping technique and 3) pattern recognition-based graph cost design.

The LOGISMOS method's utility and performance are demonstrated on a knee-joint bone and cartilage segmentation task. Although trained on only a small number of nine example images, this system achieved good performance as judged by Dice Similarity Coefficients (DSC) using a leave-one-out test, with DSC values of 0.84 ± 0.04, 0.80 ± 0.04 and 0.80 ± 0.04 for the femoral, tibial, and patellar cartilage regions, respectively. These are excellent values of DSC considering the narrow-sheet character of the cartilage regions. Similarly, very low signed mean cartilage thickness errors were observed when compared to manually-traced independent standard in 60 randomly selected 3D MR image datasets from the Osteoarthritis Initiative database – 0.11 ± 0.24, 0.05 ± 0.23, and 0.03 ± 0.17 mm for the femoral, tibial, and patellar cartilage thickness, respectively. The average signed surface positioning error for the 6 detected surfaces ranged from 0.04 ± 0.12 mm to 0.16 ± 0.22 mm, while the unsigned surface positioning error ranged from 0.22 ± 0.07 mm to 0.53 ± 0.14 mm.

The reported LOGISMOS framework provides robust and accurate segmentation of the knee joint bone and cartilage surfaces of the femur, tibia, and patella. As a general segmentation tool, the developed framework can be applied to a broad range of multi-object multi-surface segmentation problems.

Following the LOGISMOS-based cartilage segmentation, a fully automated meniscus segmentation system was build using pattern recognition technique. The leave-one-out test for the nine training images showed very good mean DSC 0.80 ± 0.04. The signed and unsigned surface positioning error when compared to manually-traced independent standard in the 60 randomly selected 3D MR image datasets is 0.65 ± 0.20 and 0.68 ± 0.20 mm respectively.

Abstract Approved: _____

Thesis Supervisor

_____

Title and Department

_____

Date

MULTI-SURFACE, MULTI-OBJECT OPTIMAL IMAGE SEGMENTATION: APPLICATION IN 3D KNEE JOINT IMAGED BY MR

by

Yin Yin

A thesis submitted in partial fulfillment of the
requirements for the Doctor of Philosophy degree
in Electrical and Computer Engineering
in the Graduate College of
The University of Iowa

July 2010

Thesis Supervisor: Professor Milan Sonka

Graduate College
The University of Iowa
Iowa City, Iowa

CERTIFICATE OF APPROVAL

PH.D. THESIS

This is to certify that the Ph.D. thesis of

Yin Yin

has been approved by the Examining Committee for the thesis requirement for the Doctor of Philosophy degree in Electrical and Computer Engineering at the July 2010 graduation.

Thesis Committee: _____
Milan Sonka, Thesis Supervisor

_____
Gary E. Christensen

_____
Punam K. Saha

_____
Xiaodong Wu

_____
Donald D. Anderson

ACKNOWLEDGEMENTS

I would like to express the deepest appreciation to my advisor, Professor Milan Sonka, whose encouragement and expertise greatly helped me to conduct this research. Without his guidance and persistent help this dissertation would not have been possible.

I am indebted to Dr. Donald D. Anderson for his constant support in knee orthopedic knowledge and independent knee validation standard collection.

I am sincerely grateful to other committee members, Professor Gary E. Christensen, Professor Punam K. Saha and Professor Xiaodong Wu. I really appreciate their great comments on the research. Many of my ideas in "cross-object surface mapping", "robust cost design" and "graph structure formation" were inspired from the discussions with them. Especially, discussions with Prof. Saha regarding distance transforms greatly helped me for the invention of ELF-based constraint-point cross-object surface mapping technique.

The work was supported, in part, by NIH grants R01 EB004640 and P50 AR055533.

The contribution of R. Williams, C. Van Hofwegen, N. Laird and N. Muhlenbruch, who provided the knee-joint manual tracings, is gratefully acknowledged.

My former and current colleagues in the University of Iowa also provided thoughtful ideas and help during my research, which I appreciate. I especially thank Mona Garvin, Honghai Zhang, Fei Zhao, Kyungmoo Lee, Richard Downe, Xin Dou, Kunlin Cao, Kai Ding and Qi Song.

Last but not least, I want to thank to my family members, for their love and support throughout this work. I affectionately dedicate this thesis to them.

TABLE OF CONTENTS

LIST OF TABLES

Table

LIST OF FIGURES

Figure

CHAPTER 1
MULTI-SURFACE MULTI-OBJECT SEGMENTATION PROBLEM

Medical image segmentation is a continuously evolving field. Due to the anatomical complexity and possible presence of pathologies, segmentation tools for general purpose tasks are difficult to derive. The medical image analysis objects of interest are typically three-dimensional, and they frequently consist of 3D regions separated by interacting surfaces, e.g., endo- and epicardial heart surfaces (Fig. 1.1a), multi-layer structure of human retina (Fig. 1.1b), inner and outer vascular walls (Fig. 1.1c), etc. These are *intra-object* interactions.

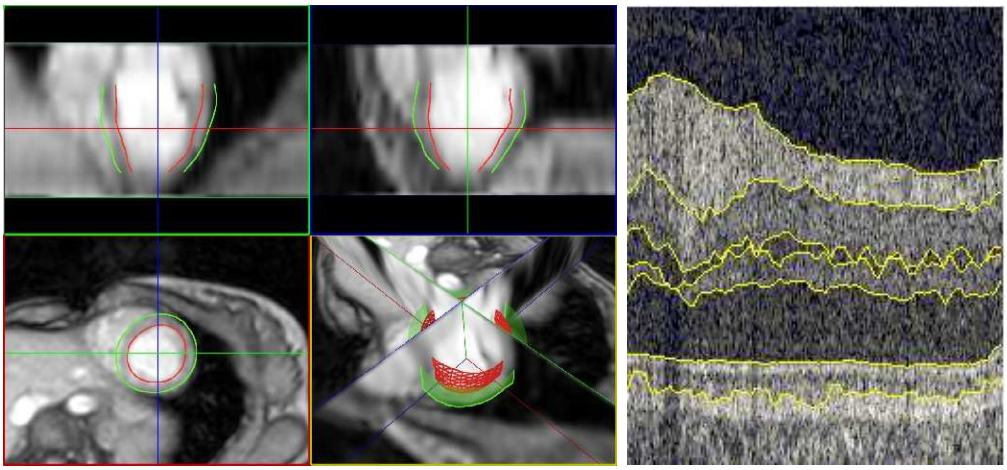

(a) (b)

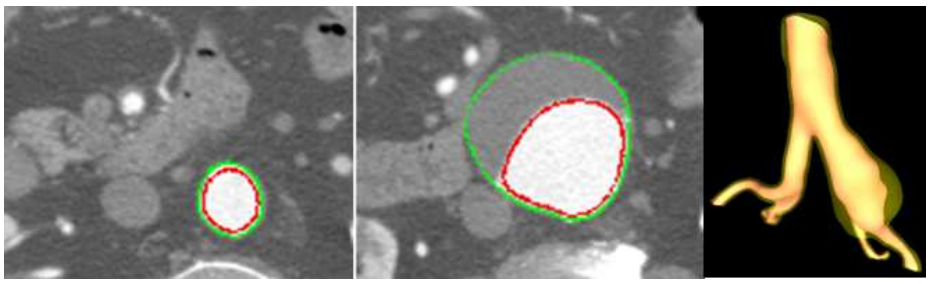

(c)

Figure 1.1: Intra-object interaction examples: (a) Endo- and epicardial ventricular surfaces (b) Multi-layer retinal structure (c) Inner and outer vascular walls

Similarly, organs typically occur in pre-specified anatomical relationships and it seems advantageous to consider such relationships when segmenting the medical images, e.g., the mutual positions of left and right cardiac ventricles (Fig. 1.2a), of the prostate and bladder (Fig. 1.2b), of the femoral and tibial knee cartilages (Fig. 1.2c), etc. These are *inter-object* relationships.

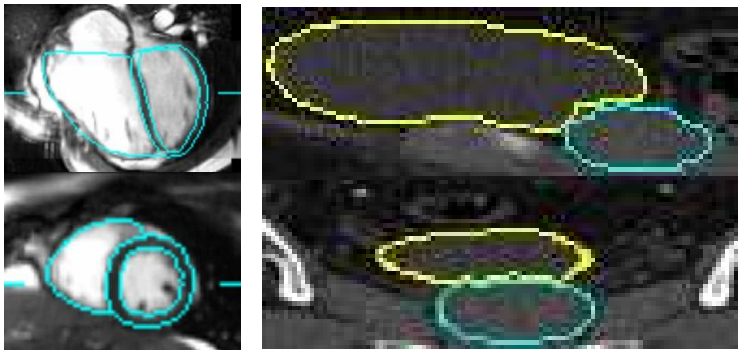

(a) (b)

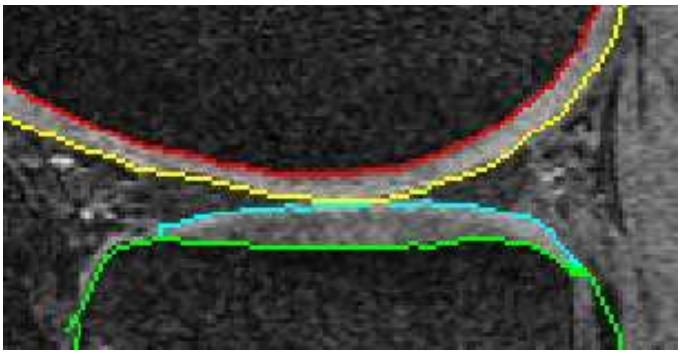

(c)

Figure 1.2: Inter-object relationship examples: (a) Mutual positions of left and right cardiac ventricles (b) Mutual positions of the prostate and bladder (c) Mutual positions of the femoral and tibial cartilages

Yet, most of the contemporary methods – even if they are increasingly frequently working inherently in 3D – concentrate on segmenting a single surface of individual organs or objects of interest [85,86]. We argue that whenever the anatomic structures

are inter-related, by intra-object or inter-object relations, a segmentation system can benefit from incorporation of the interacting information.

In the first chapter of my dissertation, I will review the contemporary related works of n-dimensional multi-surface and multi-object segmentation methods.

1.1 Multi-Surface Segmentation Algorithms

Multi-surface segmentation is commonly used for measuring the thickness of the vescular walls for aorta, or measuring the thickness of knee or ankle cartilage. In these cases, the intra-object surfaces are highly inter-related. If a single surface detection algorithm is used to segment desired surfaces one-by-one, the previous segmentation error may be accumulated to the consequent segmentations.

The multi-surface segmentation algorithms consider the intra-object relationship of multiple surfaces. The most popular multi-surface segmentation algorithms include *Active Shape Model* (ASM) [10]/*Active Appearance Model* (AAM) [9] and *optimal surface detection* [62].

1.1.1 ASM and AAM for multi-surface detection

1.1.1.1 Active shape model (ASM) segmentation

The basic idea of active shape model is to describe a shape by a trained mean shape plus variants for each mode on the shape:

$$\mathbf{S} = \bar{\mathbf{S}} + \mathbf{\Phi}_s \mathbf{b}_s \tag{1.1}$$

where $\mathbf{S}$ is a new shape vector composed by N n-dimensional points: $\mathbf{S} = [\mathbf{X}_1, \mathbf{X}_2, ...\mathbf{X}_N]^T$. Similarly, the mean shape $\bar{\mathbf{S}} = [\bar{\mathbf{X}_1}, \bar{\mathbf{X}_2}, \ldots, \bar{\mathbf{X}_N}]^T$. $\mathbf{\Phi}_s \mathbf{b}_s$ is the mode vector between $\mathbf{S}$ and $\bar{\mathbf{S}}$. For example, $\mathbf{\Phi}_s$ can be a $N \times N$ identity matrix, then $\mathbf{b}_s$ will be a position displacement vector $\mathbf{b}_s = [b_1, b_2, \ldots, b_N]^T$. However, a full size $\mathbf{b}_s$ is not useful to simplify the relationship between a new shape with prior knowledge $\bar{\mathbf{S}}$. In that case, a $N \times M$ ($N \gg M$) matrix $\tilde{\mathbf{\Phi}}_s$ and a M vector $\tilde{\mathbf{b}}_s$ is used

to approximate $\mathbf{S}$:

$$\tilde{\mathbf{S}} = \bar{\mathbf{S}} + \tilde{\mathbf{\Phi}}_s \tilde{\mathbf{b}}_s \tag{1.2}$$

The solution can be reduced to answer the following two questions:

- How to compute $\bar{\mathbf{S}}$ and ϕ_s before a new shape is given?
- How to compute $\tilde{\mathbf{b}}_s$ after a new shape is given?

$\bar{\mathbf{S}}$ and ϕ_s are computed from a group of existing shape datasets. The process is called training process and the shape dataset is called training dataset. After aligning these training shapes – e.g. by *Procrustes analysis* [38] – the average point locations for these aligned shapes form the mean shape.

Principal Component Analysis (PCA) [48], which is very suitable for shape analysis, is a powerful tool to keep the most important information from a dataset according to its variants . $\tilde{\mathbf{\Phi}}_s$ can be designed as M eigenvectors which correspond to the first M largest variances. Then the new shape can be synthesized by finding a vector $\mathbf{b}_s$ to control $\bar{\mathbf{S}}$ at M orthogonal directions with largest variances. So that

$$\mathbf{S} \approx \bar{\mathbf{S}} + \tilde{\mathbf{\Phi}}_s \tilde{\mathbf{b}}_s \tag{1.3}$$

If given a new shape $\mathbf{S}$, $\tilde{\mathbf{b}}_s$ can be easily computed by

$$\tilde{\mathbf{b}_s} = \tilde{\mathbf{\Phi}}_s^{-1}(\mathbf{S} - \bar{\mathbf{S}}) \tag{1.4}$$

1.1.1.2 Active appearance model (AAM) segmentation

Although ASM is relatively fast and simple, it does not incorporate regional intensity/texture information in parameters. As a result, it is not robust and may not converge to a good solution.

A model combining these variables, similar as ASM, may be analyzed by PCA,

so that:

$$\mathbf{g} \approx \bar{\mathbf{g}} + \mathbf{\Phi}_g \mathbf{b}_g \tag{1.5}$$

Where $\mathbf{g}$ represents regional information vector. If we concatenate formulas 1.4 and 1.5 with a weighting matrix $\mathbf{W}$, we can use all information in one model and reduce the parameters.

$$\mathbf{b} = \begin{bmatrix} \mathbf{W}_s \mathbf{\Phi}_s^T (\mathbf{S} - \bar{\mathbf{S}}) \\ \mathbf{\Phi}_g^T (\mathbf{g} - \bar{\mathbf{g}}) \end{bmatrix} \tag{1.6}$$

The AAM is given by a PCA of $\mathbf{b}$

Reference [104] provides an overview of ASM and AAM methods. The author also provides an application of using AAM to segment 4D cardiac MR images. In that work, the algorithm created a left ventricle model with inner and outer surfaces and it detected two surfaces simultaneously.

1.1.2 Optimal multi-surface detection

The idea of optimal surface detection comes from finding *optimal net surface* problem in a proper ordered graph [95] which is further implemented to solve surface segmentation problem in medical image applications. Use of this method in the medical image segmentation area closely followed to solve multiple coupled surface segmentation problems [34, 41, 60–62, 106].

Out of these publications, [62] is considered a pioneering paper in which Li *et al.* explained and verified how to optimally segment single and multiple coupled flat surfaces represented by a volumetric graph structure. This work was further extended to optimally segment multiple coupled closed surfaces of a single object [61]. Later, Garvin *et al.* introduced in-region cost concept [41] and applied it to 8-surface segmentation of retinal layers from OCT images [34]. Lee *et al.* utilized this concept for 3D dual-surface inner/outer aortic wall segmentation [59]. The rationale and extensions of this algorithm will be described in detail in Chapter 4 and 5.

1.2 Multi-Object Segmentation Algorithms

Multiple object segmentations include intra-object segmentations and inter-object segmentations. In intra-object segmentation, the subjects concerned are from one source, usually 3D volumetric data plus time forming 4D data. The example is like different phases of cardiac pulsation. Most n-dimension segmentation algorithms can be applied in this situation.

Here we are focusing on inter-object segmentation. In this case, the subjects are from different sources and they are related in 3D space. Similar to multi-surface segmentation, the segmentation result will not be optimal if these objects are segmented individually without considering their interacting relationships. Multi-object segmentation algorithms can be summarized into the following categories: deformable model segmentation, atlas-based segmentation, multi-agent approach and statistical classification.

1.2.1 Deformable model segmentation

As indicated by its name, this segmentation method starts with a deformable initial model. The segmentation result is generated by the evolvement of the model's boundary. A widely used technique for the model evolvement is to minimize an energy term, which is composed by internal energy and external energy. The internal energy penalizes the shape variance between the new shape and the priori shape knowledge, while the external energy attracts the model to the shape information independent location. For instance, Lorenz *et al.* built a comprehensive deformable model [66] which included the four cardiac chambers and the trunks of the connected vasculature, as well as the coronary arteries and a set of cardiac landmarks. Litvin *et al.* incorporated relative inter-object distances as a feature for the model, so that their models can segment well-trained coupled multiple objects [64].

1.2.2 ASM & AAM

The theories of ASM and AAM have been introduced in Section 1.1. If multiple objects are positioned with relatively fixed positions, it may be plausible to create one combined AAM model and segment the objects together. Freedman *et al.* had a combined prostate and rectum wall AAM [27, 28]. They matched the overlapping blocks between initial guess and true objects by histogram distribution. The appearance information was extracted from histogram distribution of these overlapping blocks.

Bruijne and Nielsen designed a shape particle model based on ASM for ribs [7]. They randomly permuted and perturbed the particle on the 2D chest X-ray images. The algorithm will converge when the maximum posteriori probability of a shape set given by an image is reached, so that all rib segmentation is done. Detecting similar objects with unknown number is the major contribution of their work. Although the work was applied in 2D, it could be easily extended in 3D.

1.2.3 Atlas-based segmentation

Atlas segmentation maps a gray-level image I to a labeled image A by a transformer T. The label on A is called atlas. Unlike deformable models, the atlas changes its shape under T, which is usually retrieved by an image-to-image registration method. Manual labeling by experts is a common way to get the original atlas. The experiments of Rohlfing *et al.* showed that using multiple atlas classifiers was better than a single atlas classifier [80]. Although their experiments segmented 22 anatomical structures for bee brains in confocal microscopy images, as well as 43 anatomical structures for human brain MR images, the creation of their initial atlas was really time consuming and tedious.

1.2.4 Multi-agent approach

Fleureau *et al.* proposed a novel technique for segmenting n-dimensional multi-object images in a semi-interactive way. They called it a multi-agent approach [22,23].

In this framework, two kinds of agents are defined, which are situated agents (workers) initialized by interactive selection from users and communicating agents (controllers) which decide if a region should be acquired by any one of the workers. The situated agents learn local information of intensity and texture and request to acquire neighboring pixels if certain criteria are met. The communicating agents judge the request by segmentation map and travel map [22, 23].

The authors used this method to extract cardiac structures in multi-slice computed tomography images. The results are promising but yet to be fully verified.

The initialization process of multi-agent approach is similar to the graph cuts [4] and random walks [39] approaches. All of these approaches require user selecting multiple training points for each objects in question, although the final optimization processes are quite different.

1.2.5 Statistical classification

Multi-object segmentation and delineation problems can be nicely solved by statistical classifiers. For instance, Folkesson's fully automatic voxel classification method used two KNN classifiers to distinguish femoral and tibial cartilages [24]. The major drawback of the statistical methods is the computational complexity needed to extract features and classify each voxel in a 3D image. Dam accelerated the classification process [13]. His method required about 15 minutes to segment femoral and tibial cartilages in a 170×170×110 MR image with *sample-expand* and *sample-surround* algorithms.

1.3 Chapter Summary

Although every method proved to be successful in one specific multi-object or multi-surface segmentation application, few methods showed their generality for a "multiple surfaces on multiple objects segmentation" problem. A good example of this problem is from cartilage segmentation of a knee joint. As seen in Fig. 1.3, a

knee joint includes femur, tibia, patella, some ligaments, meniscus, muscle, synovial fluid, etc. Overall, it is a very complex structure.

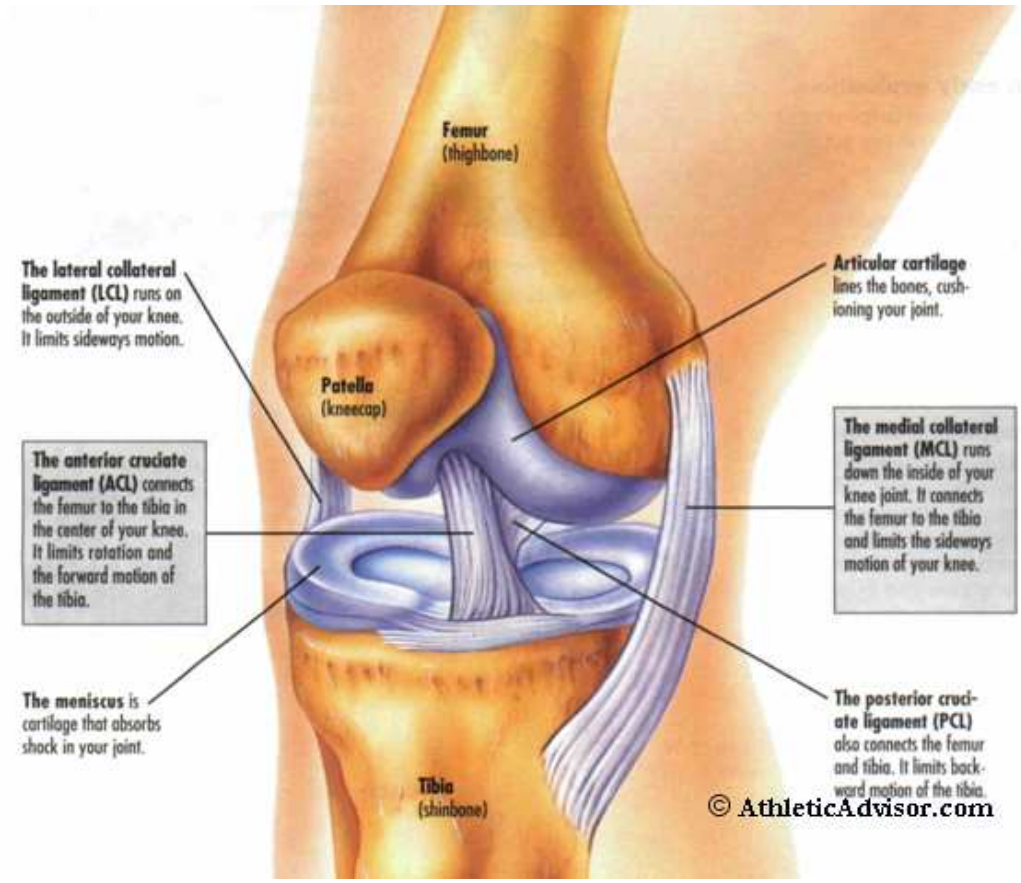

Figure 1.3: The anatomy of a knee joint. From www.AthleticAdvisor.com

In order to segment bone and cartilage surfaces from this structure, we may benefit from incorporating interacting bone and cartilage relationships (intra-object interaction). Furthermore, the adjacent cartilages could be contacted, resulting in no obvious boundary information under any medical imaging modalities (CT, MR, etc.). Under this circumstance, if the inter-object relationship between adjacent cartilage surfaces is not considered, the segmentation result will not be accurate.

The same argument can be equally applied to other interacting bone-cartilage

structures, like ankle joint, hand, etc.

In order to design a general multi-object multi-surface segmentation system, the possible extensions for the methods outlined in this chapter were considered. However, most of them are quite difficult for the extension.

While ASM/AAM proved to be suitable for either multi-object or multi-surface segmentation, it is difficult to design a general multi-object multi-surface segmentation system based on ASM/AAM due to the large training set size requirements in higher-dimensional spaces. The atlas-based segmentation needs a powerful registration method both for overall labeled template set as well as individual labeled template in the set. Since this registration is hard to derive, the atlas-based segmentation for general objects cannot be expected to be accurate. The multi-agent approach seems still immature. Despite lack of sufficient validation, the large amount of user interaction and difficulty to incorporate priori shape information are also a big concern for us. The same thing is also true for the similar approaches like graph cuts segmentation and random walks segmentation. The statistical classification methods, in theory, can segment as many objects as possible. However, the drawbacks for long computation time and no global shape information incorporated are also prominent.

The optimal surface detection based on graph search approach is most promising. A framework for multiple closed surfaces on single object was designed and proved to be successful [61]. The challenge for incorporating inter-object interaction is how to find and connect corresponding graph columns between interacting pre-segmented surfaces. In the following chapters, I will propose a possible solution to map two adjacent surfaces and generate a general n-D multi-object multi-surface segmentation framework. This framework will be applied for a 3D knee bone-cartilage surface delineation application. Finally, based on cartilage segmentation result, a meniscus segmentation system is designed, implemented and validated.

CHAPTER 2
KNEE OSTEOARTHRITIS STUDY USING MEDICAL IMAGING

2.1 Osteoarthritis

Knee osteoarthritis(OA) is a group of knee diseases and mechanical abnormalities which causes joint degradation. In the United States, there are about 27 million people being affected by OA, and about 80% of the US population will have OA by age 65. Furthermore, hospitalizations for OA had rised to 0.7 million in 2006.

OA incurs knee cartilage losses and serious pain to the patient. Although many pharmaceutical companies involved in OA treatment drug research, so far, there is no disease modifying OA drug obtained regulatory approval. In severe cases, joint replacement surgery may be required.

2.2 Imaging Techniques and Osteoarthritis Initiative

Evaluation of cartilage degeneration is important in the orthopedic surgery because the degeneration usually occurs first before the pain in knee is felt. Cartilage volume, cartilage thickness and cartilage surface area are most commonly measured parameters to evaluate joint cartilage degeneration. Medical imaging technique provides a precise and non-invasive methods to evaluate these parameters. While in computed tomography (CT) images, bone structure can be better depicted, the soft tissues including knee cartilage are clearer in magnetic resonance (MR) images.

In order to create a public resource for identifying, characterizing and validating knee OA biomarkers, the National Institutes of Health (NIH) sponsored a research project called Osteoarthritis Initiative (OAI) [73], which is available for public access at http://www.oai.ucsf.edu/. There are a total of 4796 men and women, aged 45 to 79 years, who either have or are at increased risk of developing knee OA being enrolled in the project. All participants have annual radiography and MR imaging (MRI) of the knee and clinical assessments of disease activity available over a period of four years. As the MRI acquisition time increases exponentially with the increase

of spatial resolution, the total acquisition time for each clinical visit is limited to 75 mins. Among all the acquired MRI protocols, 3 Tesla (T) sagittal 3D DESS (dual echo steady state) WE (water-excitation) sequences spent the most time (about 21.2 mins for both knees) and have highest spatial resolution (0.7 mm slice thickness $\times$ 0.37 mm $\times$ 0.46 mm). These are many reasons to elect this protocol. For example, 3T may offered better signal level which could be traded for increased signal-to-noise ratio (SNR), spatial resolution or imaging speed when compared with 1.5T although the latter is more routinely available in clinical and research settings. Unlike true T2 and T1 weighted images, the contrast of DESS is quite unique. It is found that 3D DESS with selective WE provides better cartilage delineation for morphological measurements (e.g. total joint cartilage thickness and volume) and faster acquisition speed than 3D fat-suppressed 3D fast low-angle shot (FLASH) or 3D spoiled gradient-recalled echo (SPGR) with equivalent image contrasts, although FLASH and SPGR had been more extensively evaluated for quantitative cartilage measurements [73]. Fig. 2.2 shows a example slice of a 3D sagittal DESS MR volume where we can clearly see the cartilage-capsule and cartilage-cartilage interfaces (which are usually difficult to discriminate with 3D FLASH WE), as well as the interfaces between cartilage and adipose, bone and meniscus.

2.3 Previous Knee Cartilage Segmentation Works

Delineate cartilage directly on medical images by radiologists is tedious and time-consuming especially in 3D. Automated segmentation of articular cartilage in the knee has been researched for decades. Many MR image analysis approaches have been developed with varying levels of automation. An excellent overview of previously reported approaches to articular cartilage MR image acquisition and quantitative analysis is given in [20].

Lynch used *region growing* segmentation with manual initialization [67,68]. Carballido-Gamio developed a semi-automated approach based on *Bezier splines* [33]. Similarly,

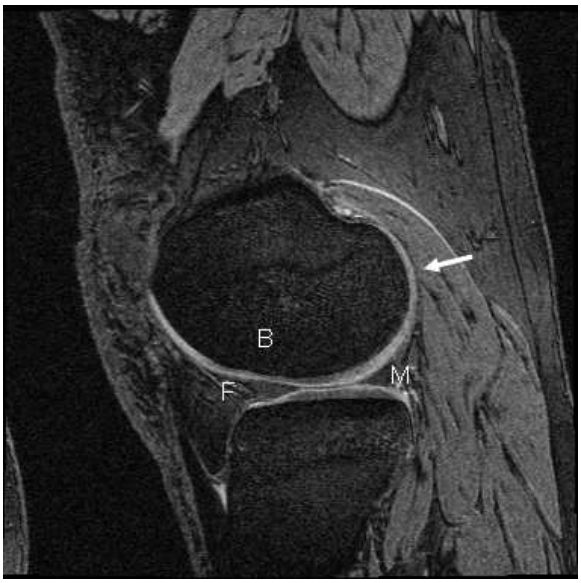

Figure 2.1: A sample slice of a 3D sagittal DESS WE volume. The interfaces of cartilage-cartilage, cartilage-capsule (arrow), cartilage-bone (B), cartilage-meniscus (M) and cartilage-adipose (F) are clearly imaged.

Raynauld and König both selected *active contour* approaches [55, 79]. These methods generally depend upon user interactive processes to select initial contours and frequently require human-expert correction of the final results.

A higher level of automation has been achieved using *Statistical Shape Models* (SSM) or *Active Shape Models* (ASM). For instance, Solloway reported cartilage segmentation based on ASM [82, 83]. Kapur adopted the strategy to first segment the more easily identifiable femur and tibia bones by region growing, and then detect cartilage voxels using a *Bayesian classifier* [50]. Pirnog combined ASM and Kapur's strategy to produce a fully automated segmentation of patellar cartilage [75].

Fripp designed an automated segmentation system based on SSM [31]. In this work, when given a pre-segmented bone-cartilage interfaces, it took about an hour to segment the cartilage surface on an MR image with size 512×512×70. More recently, Fripp *et al.* [32] employed atlas-based bone registration and bone-cartilage interfaces (BCI) were segmented by *Active Shape Models*. The cartilage surfaces

were detected along BCIs using active surface models. This system achieved very good segmentation results but required optimization of a large set of parameters and suffered from long segmentation times. Based on similar statistical shape modeling principles, a method for defining anatomical correspondence enabling regional analysis of cartilage morphology was reported in [93].

Folkesson's fully automatic voxel classification method used two KNN classifiers to distinguish femoral and tibial cartilage regions [24]. The results established that multiple binary classifiers performed better than a multiple-class classifier, and it illustrated the importance of different features for cartilage segmentation. However, like other pure pattern recognition based segmentation systems, their method suffered from slow performance. Dam *et al.* accelerated the process with *sample-expand* and *sample-surround* algorithms [13]. His method required about 15 minutes to segment femoral and tibial cartilages in a 170×170×110 MR image with so called *sample-expand* and *sample-surround* algorithms. Warfield's template moderated (ATM), spatially varying statistical classification (SVC) algorithm combined nonlinear registration and KNN classification [92]. Other employed approaches include *Watershed Transform* by Grau or Ghosh [36, 40].

An excellent overview of previously reported approaches to articular cartilage MR image acquisition and quantitative analysis is given in [20].

2.4 Chapter Summary

Knee cartilage segmentation as a clinically relevant segmentation problem is gaining considerable importance in recent years. The segmentation result can provide quantification of cartilage deterioration for the diagnosis of OA and optimization for surgical planning of knee implants. Although most previous knee segmentation works were performed on 1.5T FLASH and SPGR MR images, it was suggested from OAI dataset to use 3T DESS MR images instead. The sagittal 3D 3T DESS WE images in OAI have high-resolution, good delineation of articular cartilage, fast ac-

quisition time and high SNR. Considering the complimentary image sources for over four thousand participates with baseline and four year's follow-up radiographs and MR images as well as continuous support from NIH and contributions of biomarkers from other researchers, we believe that it is important and progressive to set up our knee segmentation experiments on the sagittal 3D 3T DESS WE images in OAI.

CHAPTER 3
AIMS AND CONTRIBUTIONS

Substantial effort has been devoted to developing automated or semi-automated image segmentation techniques in 3D [86]. Recently, we have reported a layered graph approach for optimal segmentation of single and multiple interacting surfaces of a single n-dimensional object [62, 95]. Despite a pressing need to solve multi-object segmentation tasks that are common in medical imaging (e.g., multiple organ segmentations), the literature discussing such methods is very limited.

We report a novel approach called LOGISMOS, or Layered Optimal Graph Image Segmentation of Multiple Objects and Surfaces. While our method is motivated by the clinical need to accurately segment multiple bone and cartilage surfaces in osteoarthritic joints, including knees, ankles, hips, etc., the LOGISMOS approach is very general, and its applicability is much broader than solely orthopaedic applications. Therefore, the dissertation first introduces the LOGISMOS method in general terms while avoiding application-specific details. This is followed by the example application of knee joint cartilage segmentation, in which detailed description is provided of all aspects that need to be considered when using LOGISMOS for a specific segmentation task. In the orthopaedic application, a typical scenario includes the need to segment surfaces of the periosteal and subchondral bone and of the overlying articular cartilage from MRI scans with high accuracy and in a globally consistent manner (Fig. 3.1). Other examples include simultaneous segmentation of the prostate and bladder surfaces for radiation oncology guidance [84], segmentation of two or more cardiac chambers from volumetric image data, or other segmentation tasks requiring segmentation of multiple objects positioned in close proximity, each of the objects possibly exhibiting more than one surfaces of interest.

In addition, to better assist radiologist to research OA, a pattern recognition based meniscus segmentation approach is described as an extension of LOGISMOS-based

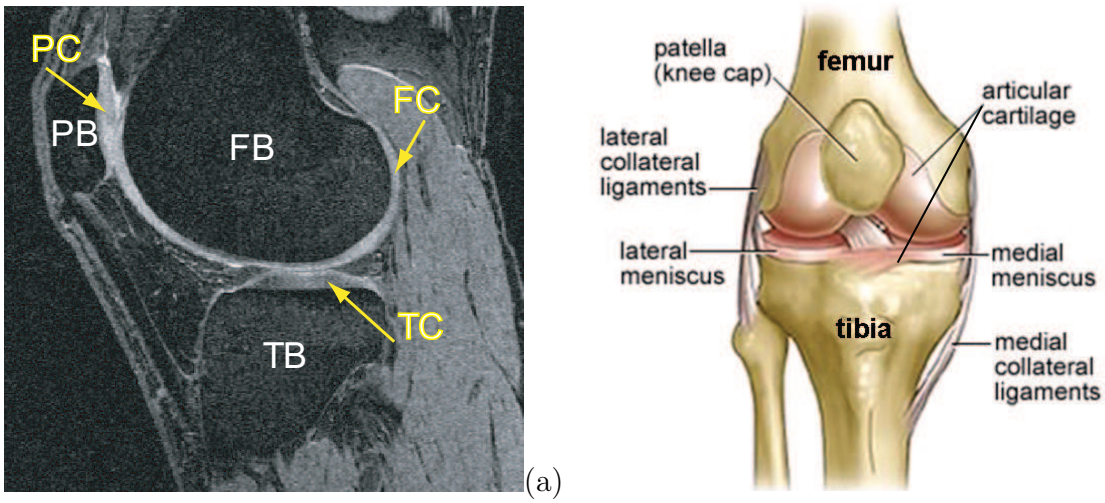

(a)
(b)

Figure 3.1: Human knee. (a) Example MR image of a knee joint – femur, patella, and tibia bones with associated cartilage surfaces are clearly visible. FB = femoral bone, TB = tibial bone, PB = patellar bone, FC = femoral cartilage, TC = tibial cartilage, PC = patellar cartilage. (b) Schematic view of knee anatomy; adapted from http://www.ACLSolutions.com.

knee bone-cartilage segmentation.

3.1 Aims of the Work

Considering the pressing need for segmenting multiple surfaces belonging to multiple coupled objects as well as the need from knee OA research, we listed the aims of our research below.

1. Develop and implement a general segmentation framework, which can incorporate both inter-surface and inter-object information in the solution finding process.

2. Develop a method for knee bone/cartilage segmentation from 3D MR images based on the general segmentation framework.

3. Develop a method for segmentation of menisci as an extension of the bone/cartilage segmentation.

4. In a medium-size study using MR knee images from the Osteoarthritis Initiative dataset, assess performance of the developed methods.

3.2 Contributions of the Work

As stated before, the optimal surface detection algorithm had been successfully utilized for segmenting multiple coupled surfaces belonging to one object [61]. The idea is suitable to be extended to segment multiple surfaces belonging to multiple mutually interacted objects. In order to achieve our aims, the following contributions were made.

1. Multi-object graph arcs were formulated and the arcs to incorporate inter-object information were built between adjacent knee cartilage surfaces.

2. A novel non-intersected search direction along electric lines of force motivated path to avoid graph column intersection problem was developed and this direction was implemented for knee bone pre-segmentation.

3. A constraint-point cross-object surface mapping technique was designed to generate one-to-one and all-to-all corresponding vertex pairs in the interacting regions between mutually coupled objects and the vertex pairs between adjacent knee bone pre-segmented surfaces were successfully found.

4. The way to directly embed pattern recognition techniques into graph cost was illustrated and the costs for bone and cartilage detection graphs were assigned by the inverse of probabilities provided by classifiers trained by problem-specific features collected in a training dataset.

5. An automated 3D knee bone volume of interest detection method was implemented by extending Viola and Jones well-known face recognition work.

6. A graph structure to segment different number of surfaces at different regions

was designed and knee cartilage/non-cartilage regions were effectively detected and applied to this graph.

7. A general multi-surface, multi-object segmentation framework – LOGISMOS (Layered Optimal Graph Image Segmentation of Multiple Objects and Surfaces) as well as a LOGISMOS-based fully-automated knee bone-cartilage segmentation system for 3D MR images were developed and implemented.

8. An automatic meniscus segmentation system for 3D MR images was implemented as an extension of our bone-cartilage segmentation.

9. The performance assessment of our bone-cartilage and meniscus segmentation systems was provided in a medium-size study using MR knee images from the Osteoarthritis Initiative dataset.

The listed contributions are novel and constitute a non-trivial extension of the previously reported method [61]. So far, to the best of our knowledge, the contributions listed here have not been reported by other researches.

CHAPTER 4
LOGISMOS – LAYERED OPTIMAL GRAPH IMAGE SEGMENTATION OF MULTIPLE OBJECTS AND SURFACES

The reported multi-object multi-surface segmentation method is a general approach for optimally segmenting multiple surfaces that mutually interact within individual objects and/or between objects. The problem is modeled by a complex multi-layered graph in which solution-related costs are associated with individual graph nodes. Intra-surface, inter-surface, and inter-object relationships are represented by context-specific graph arcs. The multi-object multi-surface segmentation reported here is a non-trivial extension of our previously reported method for optimal segmentation of multiple interacting surfaces [62].

The LOGISMOS approach starts with an object pre-segmentation step, after which a single graph holding all relationships and surface cost elements is constructed, and in which the segmentation of all desired surfaces is performed simultaneously in a single optimization process. While the description given below specifically refers to 3D image segmentation, the LOGISMOS method is fundamentally n-dimensional. Fig. 4.1 shows a flowchart of LOGISMOS framework.

4.1 Object Pre-Segmentation

The LOGISMOS method begins with a coarse pre-segmentation of the image data, but there is no prescribed method that must be used. The only requirement is that pre-segmentation yields robust approximate surfaces of the individual objects, having the same (correct) topology as the underlying objects and being sufficiently close to the true surfaces. The definition of "sufficiently close" is problem-specific and needs to be considered in relationship with how the layered graph is constructed from the approximate surfaces. Note that it is frequently sufficient to generate a single pre-segmented surface per object, even if the object itself exhibits more than one mutually interacting surfaces of interest. Depending upon the application, level sets, de-

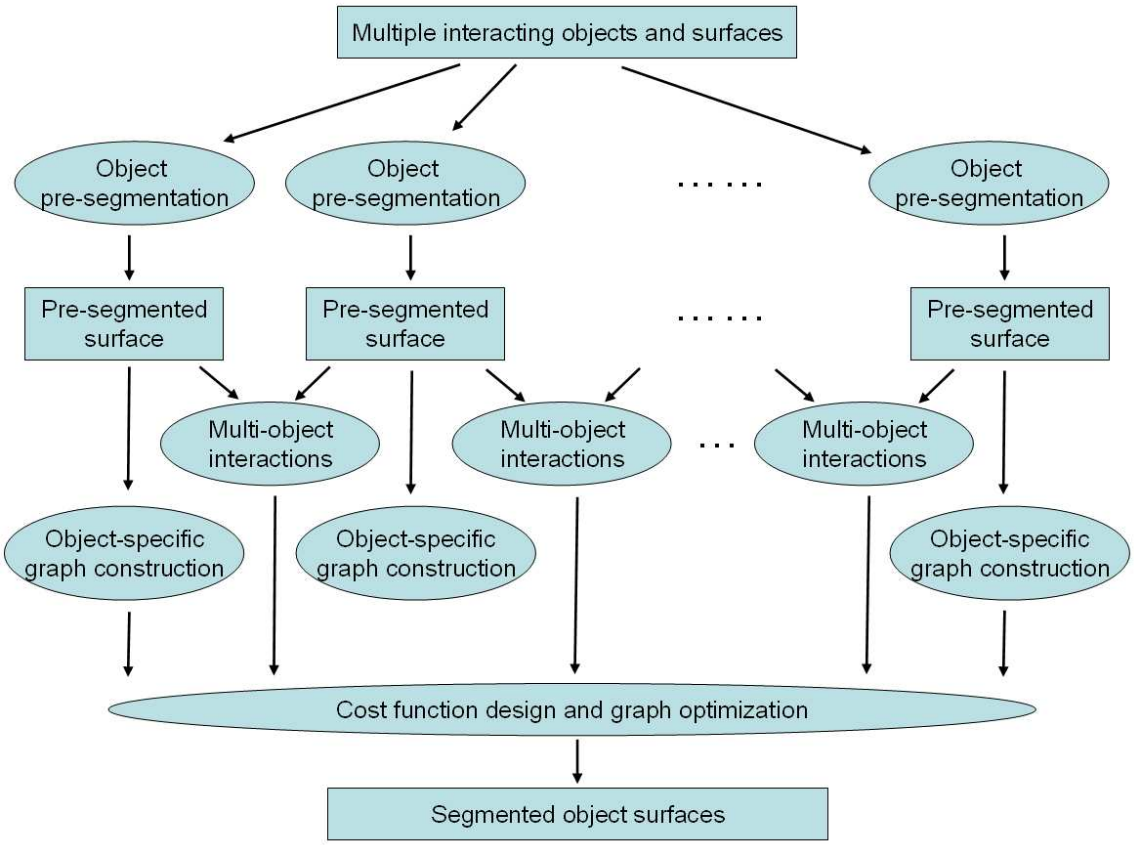

Figure 4.1: The flowchart of LOGISMOS framework.

formable models, active shape/appearance models, or other segmentation techniques can be used to yield object pre-segmentations.

4.2 Construction of Object-Specific Graphs

To represent a single or multiple interacting surface segmentation as a graph optimization problem, the resulting graph must be a properly-ordered multi-column graph, so that the segmentation task can be represented as a search for a V-weight net surface as defined in [95].

A graph $G = (V, E)$ is a collection of vertices V and arcs E. If an arc $e_1 \in E$ connects a vertex $v_1 \in V$ with $v_2 \in V$, v_1 and v_2 are called adjacent and the arc can be written as $< v_1, v_2 >$. In a graph with undirected arcs, $< v_1, v_2 >$ and $< v_2, v_1 >$ are equivalent.

In a multi-column graph, an undirected graph $B = (V_B, E_B)$ in $(d-1)$-D is called the base graph and represents the graph search support domain. An undirected graph $G = (V, E)$ in d-D is generated by B and a positive integer K, where each vertex $v_i \in V_B$ has a set V_i of K vertices in V. V_i is also called the *i-column* of G. An i-column and a j-column are adjacent if v_i and v_j are adjacent in B. If each node in G was assigned a cost value, then finding a net with minimum cost is called a V-weight net problem. The construction of a directed graph $\tilde{G} = (\tilde{V}, \tilde{E})$ from G was reported in [95], where lemmas were presented showing that a V-weight net $\mathcal{N}$ in G corresponds to a non-empty closed set $\mathcal{S}$ in $\tilde{G}$ with the same weight. An example of this process can be seen in Fig. 4.2. Here, G and $\tilde{G}$ have the same graph structure. The cost on a vertex in G is converted to a cost on correspondent vertex in $\tilde{G}$ by subtracting the vertex cost immediate below. This is called *cost translation* [62]. Consequently, an optimal surface segmentation problem can be converted to solving a minimum closed set problem in $\tilde{G}$. Since any vertex in a closed set should not have directed edges pointing to another vertex outside the set, the directed graph arcs between two graph columns constrain the vertical distance of the vertices belonging to adjacent columns

on $\mathcal{N}$. Because $\mathcal{S}$ in $\tilde{G}$ has global minimum sum of cost, the corresponding $\mathcal{N}$ in G guarantees global optimality. When $\mathcal{N}$ represents a surface in image segmentation application, the approach is called *optimal surface detection* [62]. Finding a minimum closed set in $\tilde{G}$ can be performed by a minimum s-t algorithm [11]. Especially, when G is properly-ordered, the optimal V-weight net in G can be computed in $T(n, m_B K)$, where n is the number of vertices in V, m_B is the number of arcs in E, and T is the time for finding a minimum s-t cut in an edge-weighted directed graph.

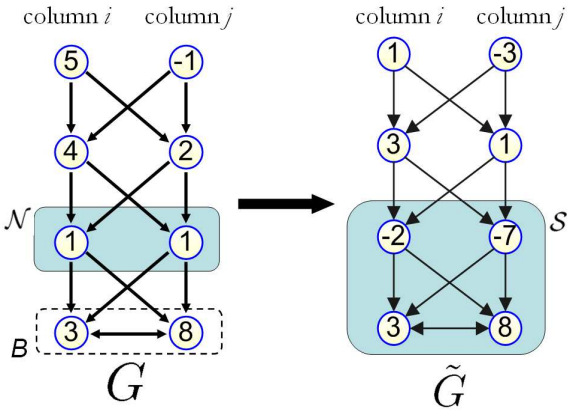

Figure 4.2: The process of converting finding V-weight net $\mathcal{N}$ in G problem into finding non-empty closed set $\mathcal{S}$ in $\tilde{G}$ with the same weight. Here $K = 4$.

As stated before, the inter-column graph arcs can constrain the vertical distance between two vertices belonging to adjacent graph columns. If columns i and j are used to detect adjacent positions of one surface, these inter-column graph arcs control the surface smoothness. If these two columns represents location detection for different surfaces, then the inter-column graph arcs are also called *inter-surface arcs* [62], which define the separation constraint between the two coupled surfaces. The details of how to build optimal surface detection graph in image segmentation applications are discribed in Chapter 5.

If the object-specific graph is constructed from a result of object pre-segmentation as described above, the approximate pre-segmented surface may be meshed and the graph columns constructed as normals to individual mesh faces. The lengths of the columns are then derived from the expected maximum distances between the pre-segmented approximate surface and the true surface, so that the correct solution can be found within the constructed graph. The present approach to multi-surface graph construction for multiple closed surfaces was introduced in [61]. Maintaining the same graph structure for individual objects, the base graph is formed using the pre-segmented surface mesh $\mathcal{M}$. V_B is the vertex set on $\mathcal{M}$ and E_B is the edge set. A graph column is formed by equally sampling several nodes along normal direction of a vertex in V_B. The base graph is formed by connecting the bottom nodes by the connection relationship of E_B. In the multiple closed surface detection case, this base graph is duplicated each time when searching for an additional surface. The duplicated base graphs are connected by undirected arcs to form a new base graph which ensures that the interacting surfaces can be detected simultaneously. Additional directed *intra-column arcs*, *inter-column arcs* and *inter-surface arcs* incorporate surface smoothness Δ and surface separation δ constraints into the graph.

4.3 Multi-Object Interactions

When multiple objects with multiple surfaces of interest are in close apposition, a multi-object graph construction is adopted. This begins with considering pairwise interacting objects, with the connection of the base graphs of these two objects to form a new base graph. Note however, that more than one surface may need to be detected on each object, with such surfaces being mutually interacting as described above. Object interaction is frequently local, limited to only some portions of the two objects' surfaces. Here we will assume that the region of pairwise mutual object interaction is known. A usual requirement may be that surfaces of closely-located adjacent objects do not cross each other, that they are at a specific maximum/minimum distance, or

similar. Object-interacting surface separation constraints are implemented by adding *inter-object arcs* at the interacting areas. Inter-object surface separation constraints are also added to the interacting areas to define the separation requirements that shall be in place between two adjacent objects. The inter-object arcs are constructed in the same way as the inter-surface arcs. The challenge in this task is that no one-to-one correspondence exists between the base graphs (meshes) of the interacting object pairs. To address this challenge, corresponding columns i and j need to be defined between the interacting objects. The corresponding columns should have the same directions. Considering signed distance offset d between the vertex sets V_i and V_j of the two objects, inter-object arcs A^o between two corresponding columns can be defined as:

$$\begin{aligned} A^o = \{&\langle V_i(k), V_j(k-d+\delta^l)\rangle | \forall k : \\ &\max(d-\delta^l, 0) \leq k \leq \min(K-1+d-\delta^l, K-1)\} \\ &\cup \{\langle V_j(k), V_i(k+d-\delta^u)\rangle | \forall k : \\ &\max(\delta^u-d, 0) \leq k \leq \min(K-1+d-\delta^u, K-1)\} \end{aligned} \tag{4.1}$$

where k is the vertex index number; δ^l and δ^u are inter-object separation constraints with $\delta^l \leq \delta^u$.

Nevertheless, it may be difficult to find corresponding columns between two regions of different topology. The approach presented in Chapter 6 offers one possible solution. Since more than two objects may be mutually interacting, more than one set of pairwise interactions may co-exist in the constructed graph.

4.4 Cost Function and Graph Optimization

The resulting segmentation is driven by the cost functions associated with the graph vertices. Design of vertex-associated costs is problem-specific and costs may

reflect edge-based, region-based, or combined edge–region image properties [35, 41]. After the step of cost translation [62], the constructed interacting graph reflecting all surface and object interactions is a directed graph $\tilde{G}$ derived from a properly-ordered multi-column graph G. As stated before, a V-weight net problem in G can be converted to finding the minimum non-empty closed set in $\tilde{G}$. This can be done by an s-t cut algorithm, e.g. [4]. As a result of the single optimization process, a globally optimal solution provides all segmentation surfaces for all involved interacting objects while satisfying all surface and object interaction constraints.

4.5 Chapter Summary

We designed a multi-object multi-surface segmentation method based on graph search based optimal surface detection algorithm. We call that LOGISMOS approach which is a general approach for optimally segmenting multiple surfaces that mutually interact within individual objects or between objects. We provided the theory of LOGISMOS in this chapter. However, when implement this theory into real applications, the following things need to be done: 1) Build a graph structure to incorporate multi-surface and multi-object relationships in medical image segmentation tasks. 2) Find corresponding graph columns at interacting regions between mutually coupled object pairs. 3) Design robust graph cost. In the following three chapters, I will show how these three tasks were achieved.

CHAPTER 5
OPTIMAL SURFACE DETECTION IN IMAGE SEGMENTATION

The key segmentation technique in LOGISMOS is graph-search based optimal surface detection approach with embedded prior shape information. Graph-search based optimal surface detection algorithm has been successfully implemented in many medical image segmentation applications ranging from 2D to 4D (3D+time) [35, 59, 61, 84, 101, 105].

The theory of the optimal surface detection algorithm has been introduced in the Chapter 4. Here, we will show some examples explaining how to create optimal surface detection graphs for single surface, multiple surface, closed surface and multiple object detection in image segmentation applications. Although the examples are in 2D, the logic behind them can be easily extended into n-dimensional.

5.1 Single Surface Detection Graph

To detect black (pixel value: 0) and white (pixel value: 1) boundary in a 4×4 image (Fig. 5.1a), an optimal graph can be build as shown in Fig. 5.1b with each pixel as a graph node. The base graph is formed by the bottom row of pixels in the image. The pixel columns form graph columns and the inter-column graph links constrain the solution boundary smoothness [62]. In this case, the smoothness constraint is two, which reflects the maximum boundary changes between adjacent graph columns. The graph node cost is computed as $C = e^{-|\nabla I|/2}$ where ∇I is the gradient of the pixel value I. After cost translation and graph optimization [62], the graph finds the black-white boundary (red) which has globally minimum cost.

When we perform optimal region delineation between black and white regions, the node costs are assigned as the differences of the unlikeness probabilities for lower (black) and upper (white) regions (Fig. 5.2c). The computation of unlikeness probabilities for black changes all black pixels to have cost 0 and all white pixels to have cost 1 (Fig. 5.2a). On the contrary, the computation of unlikeness probabilities for

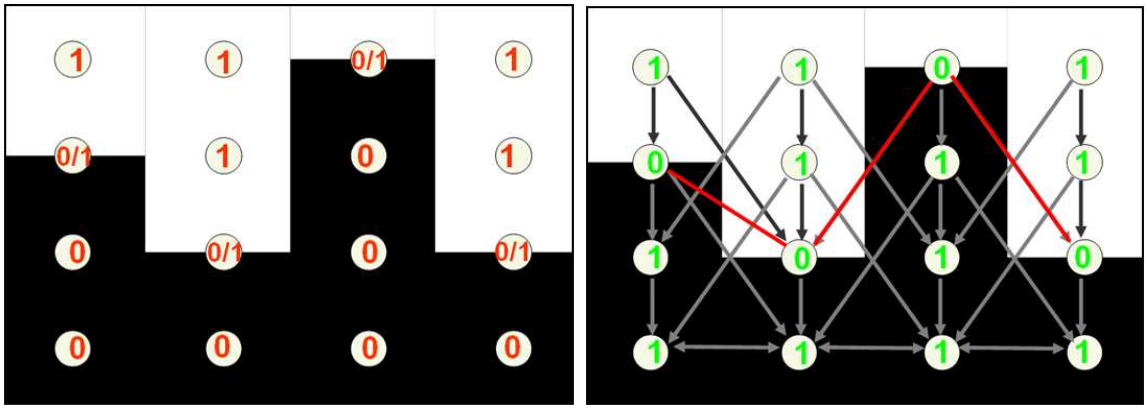

(a) (b)

Figure 5.1: The graph structure for optimal single surface detection with surface cost in an image. (a) A 2D example image with clear black-white boundary. (b) The single surface detection graph with gradient-based surface cost is built to detect red black-white boundary with globally minimum cost.

white changes all black pixels to have cost 1 and all white pixels to have cost 0 (Fig. 5.2b). The global optimal black-white region delineation is performed by directly finding minimum-cost closed set in the graph in Fig. 5.2c. This is an optimal region delineation approach using regional cost [35].

5.2 Multi-Surface Detection Graph

Optimal surface detection algorithm is suitable to detect multiple coupled surfaces [62]. In that case, two subgraphs are built and they are connected by inter-subgraph (inter-surface) graph edges between corresponding columns to constrain minimum and maximum distances between the coupled surfaces detected in each subgraph.

As an example shows in Fig. 5.3a where the gradient-based costs have been computed and assigned to each pixel. In order to simultaneously detect the two coupled black-white boundaries, we build two sub-graphs and constrain the distances between the solution surfaces by inter-surface graph arcs (pink and green arrows) at the corresponding graph columns. The new graph will detect the two desired surfaces

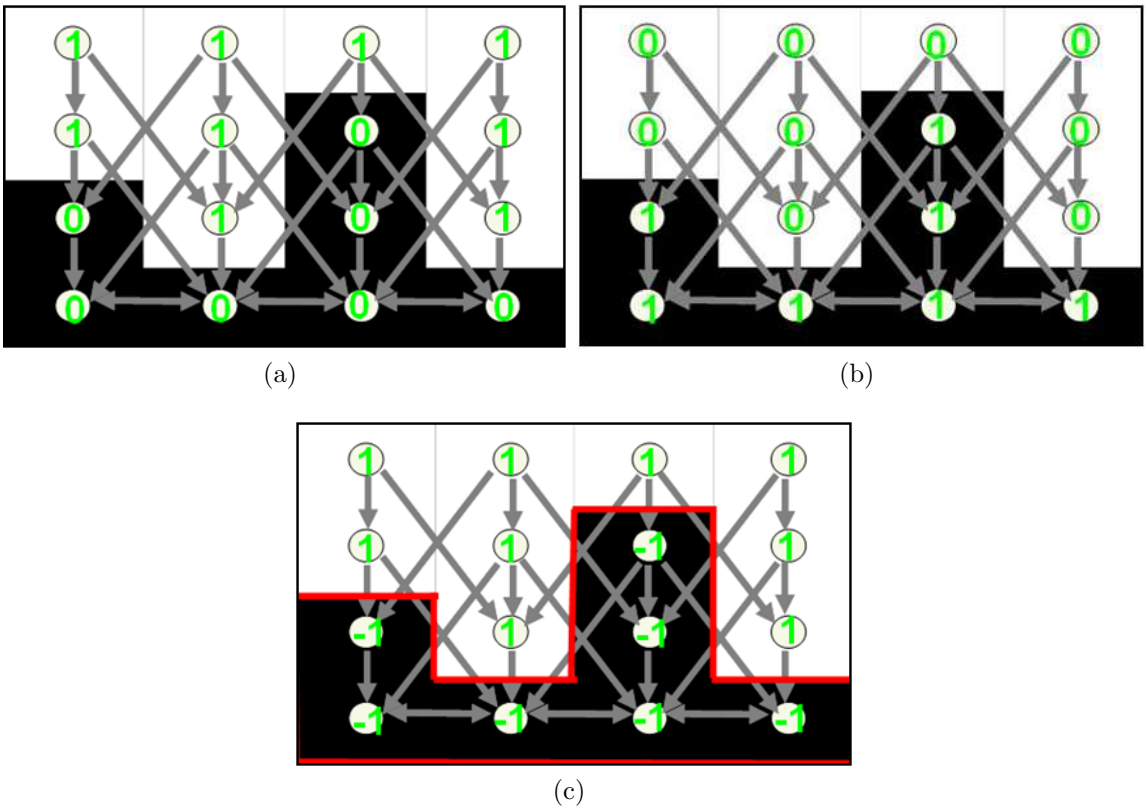

Figure 5.2: The graph structure for optimal region delineation with regional cost in an image.(a) Graph cost assigned as unlikeness probabilities for lower (black) region. (b) Graph cost assigned as unlikeness probabilities for upper (white) region. (c) Black-white region delineation performed by finding minimum-cost closed set on a graph with cost assigned as cost difference between (a) and (b).

simultaneously and optimally.

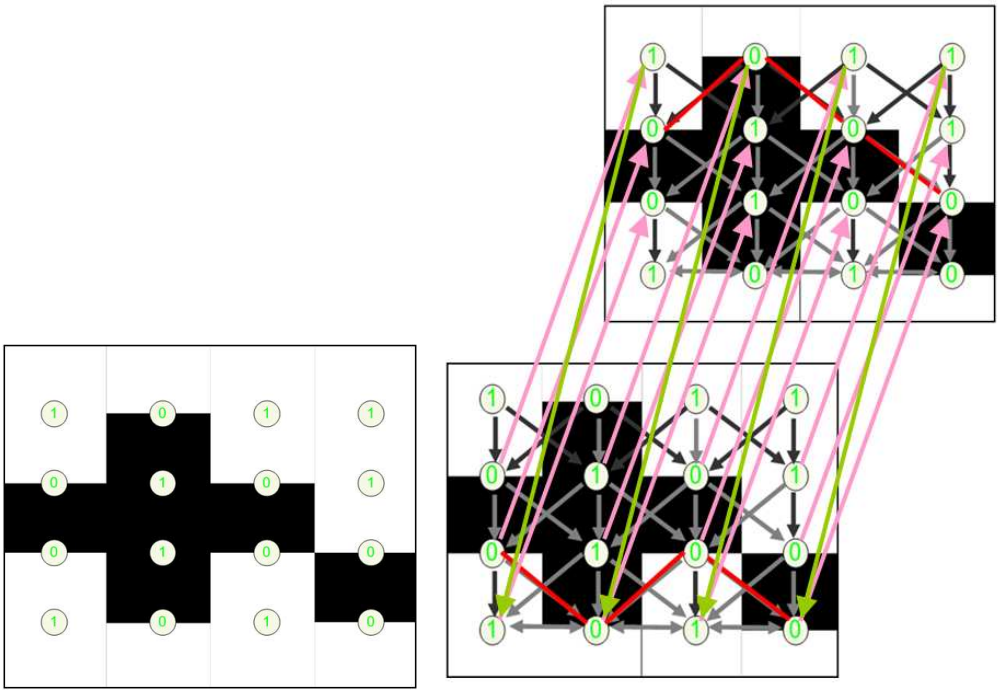

(a) (b)

Figure 5.3: The graph structure for optimal multiple coupled surface detection in an image. (a) An image with two black-white boundaries and the gradient-based costs have been assigned to each pixel. (b) The two boundaries are simultaneously detected. The distances between them are constrained by inter-surface graph arcs.

5.3 Closed Surface Detection Graph

In shape model based variant of this technique, a graph is built to mimic the initial shape: the graph nodes on each column are search points along each search direction; and the graph column adjacency is equal to the vertex neighboring relationships of the initial shape [61]. The graph edges between the graph columns constrain the solution surface smoothness according to the initial shape thus preserving the a priori shape information. With different surface or regional cost function design, this graph can

be used for globally minimum-cost surface detection [62] or globally minimum-cost region delineation [35] under the smoothness constraints (Fig. 5.4).

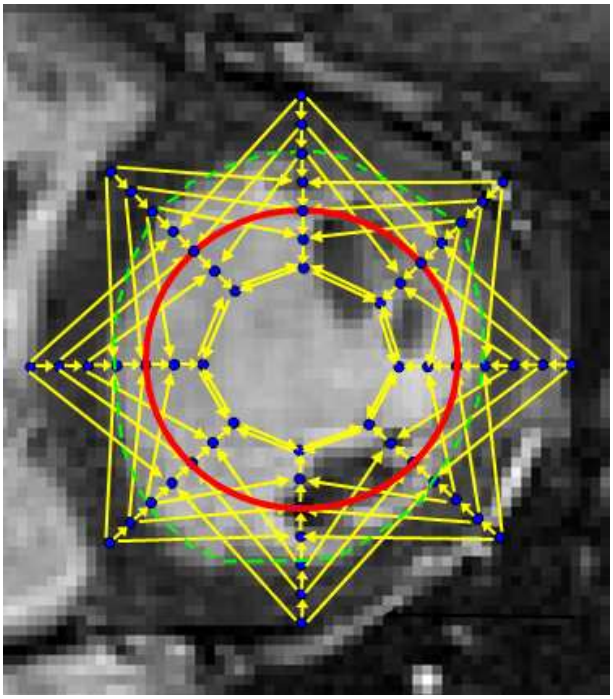

Figure 5.4: A graph was constructed along the red initial shape and the optimal search resulted in the green solution surface considering the blue candidate locations.

5.4 Multi-Object Detection Graph

In order to constrain surfaces on multiple coupled objects, the corresponding graph columns based on different initial shapes must be found, and the inter-object graph arcs (equation 4.1) can be used to constrain the distances of the solution surfaces [101]. As seen in Fig. 5.5 two subgraphs are build based on the two solid surfaces respectively, the overlapping problem between the two dotted solution surfaces are avoided by building inter-object graph edges between the two subgraphs. This kind of structure proved to be successful to constrain coupled objects for knee cartilage

segmentation [101–103] and bladder-prostate segmentation [84].

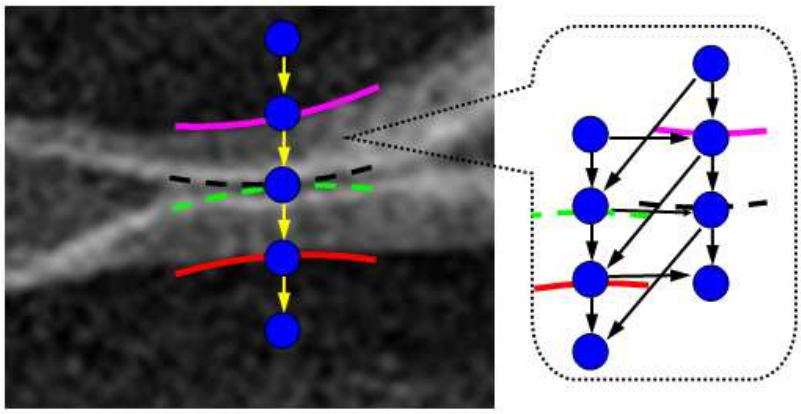

Figure 5.5: The overlapping problem of the interacted solution surfaces is avoided by inter-object graph edges.

5.5 Chapter Summary

Recently, Li *et al.* added elasticity constraint for 3D liver tumors segmentation [60]. The optimal surface detection algorithms were also embedded into a ASM framework for 3D soft tissue segmentation [45]. Interestingly, despite the successful usage in medical image segmentation, the graph structure had also proved to be helpful for image/video resizing [42] and solving optimal matrix orthogonal decomposition problem in intensity-modulated radiation therapy [96].

The solution of the graph search guarantees global optimality given the graph constraints and cost functions. The optimal solution can be computed via finding minimum-cost closed set by a s-t cut algorithm. Currently, push-relabel [8, 37], augmenting path [25] and Boykov's *graph cut* method [4] are widely used for s-t cut computation. Our experiment showed that the Boykov's graph cut method was the fastest to perform s-t cut under the graph structure.

While multi-surface detection graph is very suitable to incorporate coupling information between multiple highly correlated surfaces (e.g. inner and outer vescular walls), multi-object detection graph can constrain the distances between coupled objects (e.g. bladder and prostate). If we combine both of these structures into one graph and use it for knee cartilage segmentation, the new graph will have the strength to incorporate correlation relationship between coupled bone and cartilage surfaces as well as avoid adjacent cartilage surface overlapping. Nevertheless, it may be difficult to find corresponding columns between two regions of coupled objects with different topologies. Finding corresponding columns by nearest distance criteria [101] may help, but it cannot guarantee one-to-one and all-to-all column mapping at interacting regions since nearest distance is not robust for local shape changes. In the next chapter, I will introduce a more robust mapping technique called constraint-point cross-object surface mapping technique [100]. The idea is inspired by electric field theory.

CHAPTER 6
ELECTRIC FIELD THEORY BASED APPROACH TO SEARCH-DIRECTION LINE DEFINITION IN IMAGE SEGMENTATION

Many shape-based image segmentation techniques identify final segmentation solution along normals constructed from a preliminary segmentation. Examples include shape-based deformable model segmentation [70, 81, 91], atlas registration-based segmentation [97], graph-search based optimal closed surface segmentation [61, 62, 65, 84, 101, 105], etc.

While the solution-finding processes of these approaches differ significantly, all of them may suffer from the sensitivity of the employed normal directions to the local surface shapes, especially in areas of rapid shape changes. Due to the lack of their directional robustness, surface normals may intersect. As a result, the segmentation solution may warp and result in segmentation failure. Some techniques were adopted to handle this problem, for example, checking collision for each vertex [81], searching along maximum distance descendant directions or medial axes based resampling directions [65]. However, each of these methods has its own limitations.

We present a general solution to this problem based on an electric field motivated construction of lines, along which the search for the final segmentation solution shall be performed. This approach guarantees that such lines will not intersect and can thus replace the normal searching directions for many segmentation approaches. Utilizing optimal graph search approach as a sample segmentation strategy, the usage of the approach for graph construction and cross-object surface mapping for coupled-surface segmentation is reported and its value shown for a broad range of applications ranging from a relatively simple single-surface detection to very complex multi-surface multi-object graph based image segmentation.

6.1 Method

Starting with the initial shape, the search direction along which the final segmentation solution is identified must be defined for each location along the initial segmentation instance. Our method uses electric field theory for robust and very general definition of such search direction lines.

6.1.1 A new search direction

Recall the Coulomb's law in basic physics

$$E_i = \frac{1}{4\pi\varepsilon_0}\frac{Q}{r^2}\hat{\mathbf{r}} \,, \tag{6.1}$$

where E_i is the electric field at point i. Q is the charge of point i; r is the distance from point i to the evaluation point; $\hat{\mathbf{r}}$ is the unit vector pointing from the point i to the evaluation point. ε_0 is the vacuum permittivity.

Since the total electric field E is the sum of E_i's

$$E = \sum_i E_i \,, \tag{6.2}$$

the electric field has the same direction as the electric line(s) of force (ELF).

When multiple source points are forming an electric field, the electric lines of force exhibit a non-intersection property, which is of major interest in the context of our research task.

When computing ELF for a computer generated 3D triangulated surface, two things need to be considered: the surface is composed of a limited number of vertices and the vertices of the surface are usually not uniformly distributed. These two conditions may greatly reduce the effect of charges with short distances. In order to compensate, we assigned different positive charge Q_i to each vertex v_i. The value of Q_i is determined by the area sum of triangles t_j where $v_i \in t_j$. Note that if we change

r^2 to r^m ($m > 2$), the non-intersection property still holds. The difference is that the vertices with longer distances will be penalized in ELF computing. Therefore, a slightly larger m will increase the robustness of local ELF computation. Discarding the constant term, we defined our electric field as

$$\hat{E} = \sum_i \frac{\sum_j AREA(t_j)}{{r_i}^m} \hat{\mathbf{r}}_i \ , \tag{6.3}$$

with $v_i \in t_j$ and $m > 2$.

Assuming there is a closed surface in an n-D space, the point having a zero electric field is the solution of equation $\hat{E} = 0$. In an extreme case, the closed surface will converge to the solution points when searching along the ELF. Except for these points, the non-intersecting ELF will expand to any positions in the space that potentially avoid mis-segmentation of any object due to the searching direction.

Since ELF are non-intersected, it is easy to interpolate ELF at non-vertex locations on a surface. The interpolation can greatly reduce total ELF computation load when upsampling a surface. In 2D surface, linear interpolation from two neighboring vertices and their corresponding ELF can be implemented. In 3D, use of barycentric coordinates is better to interpolate points within triangles.

When ELF are computed from a closed surface, the iso-electric-potential surfaces can be found. Except for the solution points for equation $\hat{E} = 0$, any other point belongs to one iso-electric-potential surface, so the ELF path passing through this point can be easily interpolated. The interpolated ELF also intersects the initial closed surface. This technique can be used to create connection between a point in space to a closed surface. Therefore it leads to another important usage of ELF direction: cross-object surface mapping.

6.1.2 Cross-object surface mapping

The non-intersection property of ELF is very useful to map multiple objects with different surface topologies. The mapping can be used for optimal multi-object segmentation [49, 102]. We have identified two kinds of behavior to compute interrelated ELF of two coupled surfaces:

- Push forward: This is a regular ELF path computation using Equation (6.3) for an individual object.
- Trace back: This is an interpolation process to form an ELF path from a point in space to a closed surface. This method has been outlined in the previous section.

Fig. 6.1a shows ELF pushed forward from a surface and traced back from a point to that surface.

The general idea of mapping two coupled surfaces using ELF include 5 steps as shown in Fig. 6.1b. They are:

1. Pushing forward ELF: green and red ELF are pushed forward from surface 1 and 2, respectively.
2. Checking medial points: the intersections between the green ELF and medial separating sheet projects the orange triangle on surface 1 as a blue triangle on medial separating sheet and the intersection between red ELF and medial separating sheet is a point.
3. Tracing back ELF from medial points to the opposite surface: The red point is traced back along dotted red line to surface 1.
4. Generating constraint point on the opposite surface: when the dotted red line intersects surface 1, it forms a light-blue constraint point on surface 1.

5. Connecting the constraint point with other vertices at the opposite surface: the constraint point is connected at surface 1 by yellow edges.

This technique is called constraint-point mapping [99]. Fig. 6.1b shows an example of mapping two coupled surfaces in 3D.

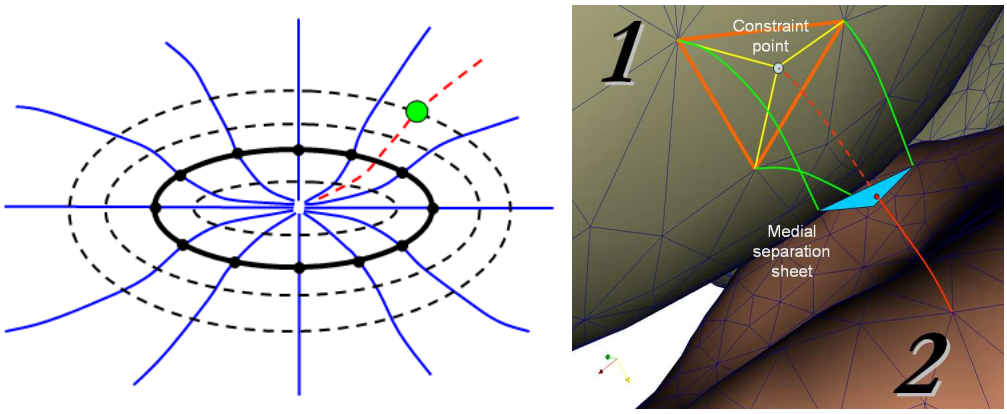

(a) (b)

Figure 6.1: Cross-object surface mapping by ELF (a) The ELF (blue lines) are pushed forward from a surface composed of black vertices. The dashed black surfaces indicate the location of iso-electric-potential contours. The red-dashed ELF is the traced-back line from a green point to the solid black surface. The traced-back line is computed by interpolating two neighboring pushed-forward ELF. (b) Constraint-point mapping of coupled 3D surfaces.

Note that each vertex in the contact area can therefore be used to create a constraint point affecting the coupled surface. Importantly, the corresponding pairs of vertices (the original vertex and its constraint point) from two interacting objects in the contact area identified using the ELF are guaranteed to be in a one-to-one relationship and all-to-all mapping, irrespective of surface vertex density. As a result, the desirable property of maintaining the previous surface geometry (e.g., the orange triangle in Fig. 6.1b) is preserved. Therefore, the mapping procedure avoids surface regeneration and merging [49] (which is usually difficult) and enhances robust-

ness regarding to local roughness of the surface when comparing with our previously introduced nearest point based mapping techniques [101, 102].

In the following section, we will show how the properties of ELF can be used for bifurcation detection, inter-surface mapping and multiple surfaces on multiple coupled objects segmentation.

6.2 Application

6.2.1 3D bifurcation detection

In airway segmentation, measuring the thickness of airway wall is desired. In CT images, the contrast of inner airway wall boundary is usually much higher than that of the outer boundary. A reasonable approach is to segment inner boundary first which is called pre-segmentation. The final segmentation can detect outer boundary based on the pre-segmented inner boundary [65, 81]. However, because of the topological complexity, segmentation along normal directions may cause surface self-intersections and therefore lead to segmentation failures at bronchial airway bifurcations.

Non-intersected ELF won't have that problem. We created an airway bifurcation phantom with inner and outer boundaries in a 3D image and we provided a perfect pre-segmented inner boundary surface. The center slice of the image with the pre-segmented surface is shown in Fig. 6.2a. Based on the pre-segmented surface, we used graph-search based optimal surface detection algorithm [61, 62] to identify the outer boundary. The graph search along the surface-normal direction will corrupt the surface due to the sharp corner as shown in Fig. 6.2b. However, when employing the directionality constraints specified by ELF, the directionality of the "normal" lines along the surface is orderly and the search can avoid the otherwise inevitable corruption of the surface solution (Figs. 6.2c, 6.2d, 6.2e).

We note that other techniques like checking collision for each vertex [81], searching along the maximum distance descendant directions, or medial axes based resampling directions [65] are also possible to avoid surface self-intersection. However, except for

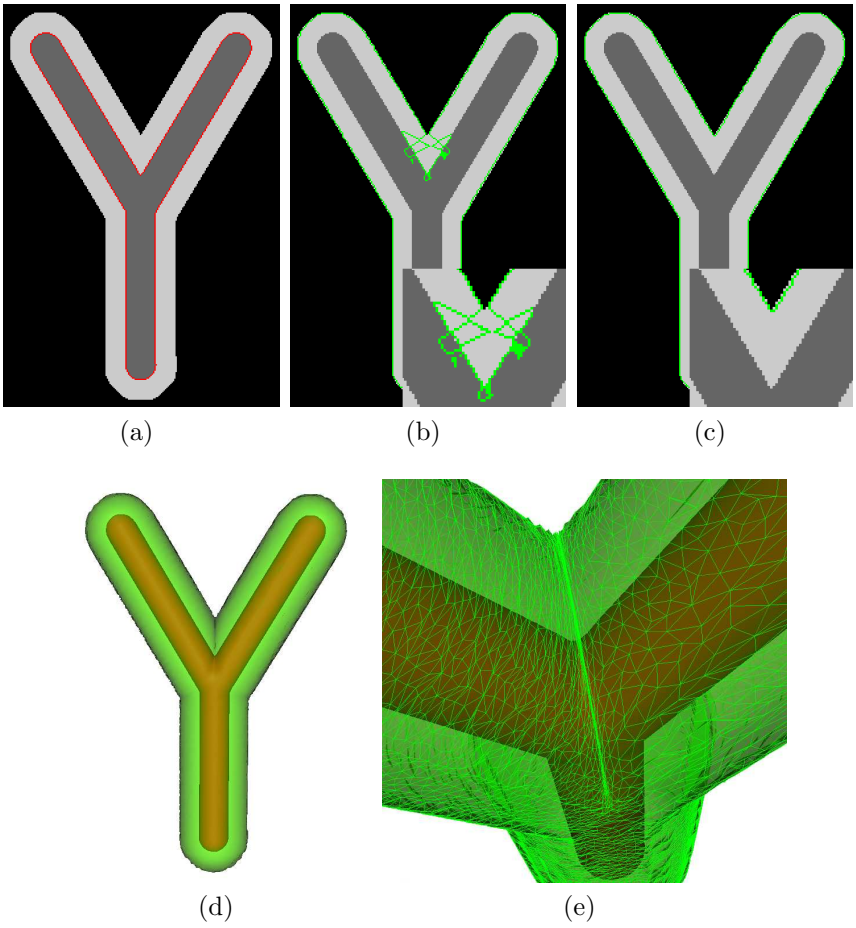

Figure 6.2: 3D bifurcation model demonstrating segmentation of the outer surface. Note that the bifurcating object consists of a tubular structure with inner and outer surfaces. (a) Pre-segmentation (red line) of the inner boundary surface is used to guide segmentation of the outer border; the center slice is shown. (b) The center slice view of graph searching result (green line) performed along normal directions of the pre-segmentation surface using our previous approach – notice the severe corruption of the surface along inner area of the bifurcation. The zoomed bifurcation part is shown at the bottom right corner. (c) The center slice view of graph searching result (green line) using graph constructed along ELF directions shows that no surface corruption is present. The zoomed bifurcation part is shown at the bottom right corner. (d) 3D view of the pre-segmented inner surface (red) and the final-segmented non-intersected outer surface (green). (e) The enlarged bifurcation part on the outer surface.

ELF search direction, these techniques may have difficulties when the initial mesh has locally concave shape as indicated in the following example.

6.2.2 Inter-surface mapping

Similar to the previous example, we search for a 3D sphere outer surface from an internal initial shape as shown in Figs. 6.3a and 6.3e. Here, the initial shape phantom marked in red color has both concave and convex local shapes which simulate shape variances of some organ structures (e.g. human eyes, bone condyle, etc). Fig. 6.3b shows searching along the normal directions that will cause a segmentation failure. This problem cannot be solved by searching along distance directions as indicated in Fig. 6.3c, because distance transform and medial-axis-based directions will be trapped in concave shapes. In contrary, the ELF direction does not have that problem (Figs. 6.3d and 6.3f). One-to-one vertex mapping of a 3D shape to a sphere as in Figs. 6.3e and 6.3f is also called surface parametrization which has many medical applications, for example, describing brain shapes [57] or visualizing protein surface properties [77]. Interestingly, if the sphere has its own topology, applying the trace-back idea, this topology can be mapped back to the initial shape as shown in Fig. 6.3g and Fig. 6.3h. This can be potentially used for automated landmarking, texture mapping and shape motion analysis [53].

6.2.3 Graph based knee cartilage delineation in 3D

The last example is a much more complicated 3D multi-object multi-surface graph search segmentation of mutually interacting femoral and tibial cartilage as well as femoral and patellar cartilage. The results of our previous attempt to solve this task were reported in 2009 [101]. We introduced a general framework to solve so-called multi-object multi-surface segmentation problem. This framework includes: 1) Model formation, 2) bone pre-segmentation, 3) cross-object surface mapping, and 4) final bone-cartilage segmentation. Here we will show how the ELF theory can be utilized in

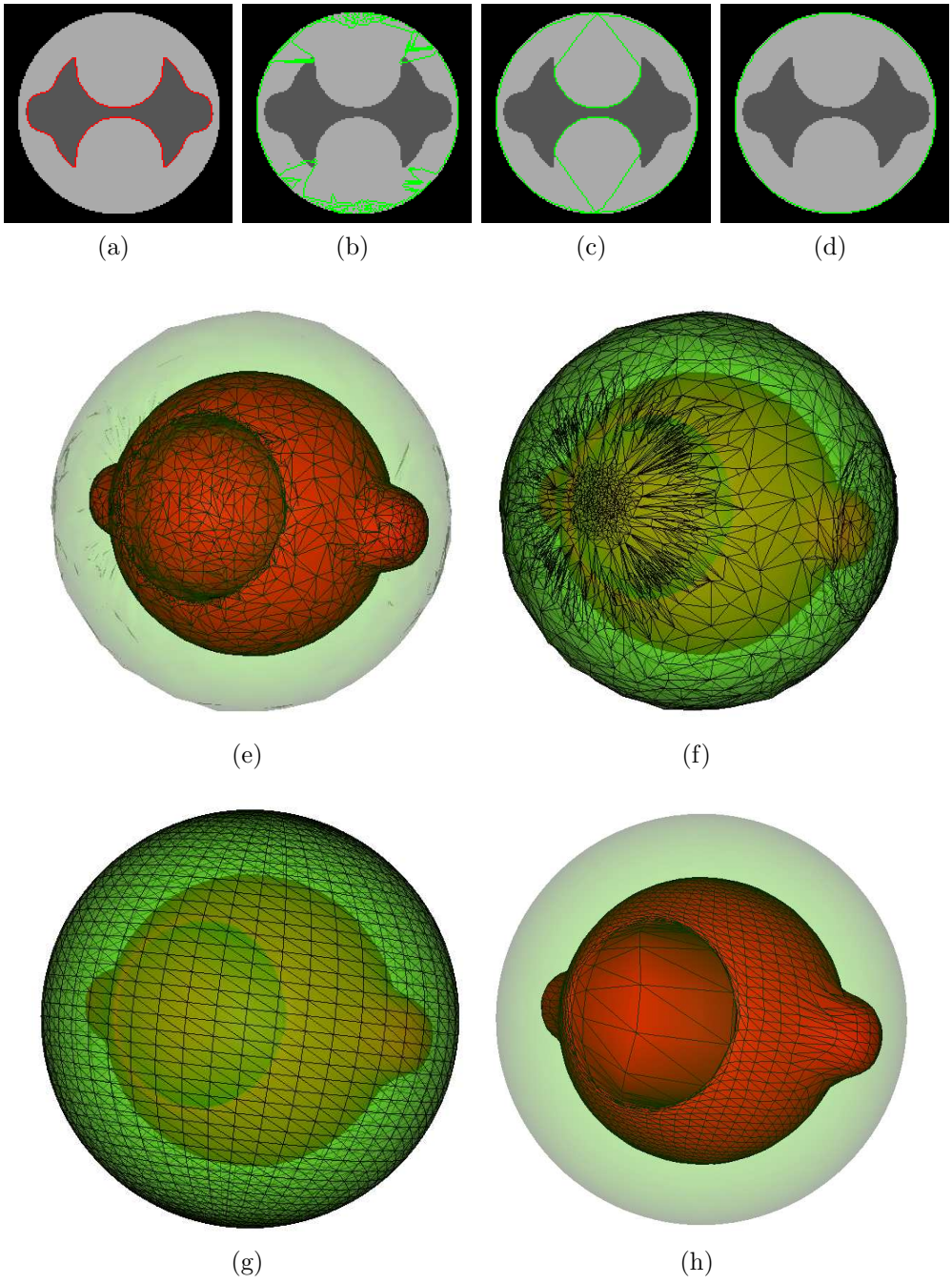

Figure 6.3: Inter-surface mapping examples. (a) Pre-segmentation (red line) of the initial shape lies within a sphere. (b) Graph searching result (green line) performed along normal directions of the pre-segmentation surface. Segmentation failure occurs. (c) Graph searching result (green line) using graph constructed along distance directions. It still cannot provide correct segmentation. (d) Graph searching result (green line) using graph constructed along ELF directions shows a good estimation of the outer sphere boundary. (e) The initial shape with its topology in 3D. (f) One-to-one vertex mapping the initial shape in (e) to outer sphere along ELF directions results in the outer sphere surface having the same topology as the initial shape. (g) A outer sphere having independent topology. (h) The topology of sphere in (g) can be traced back to the initial shape, resulting in a new topology for the initial shape.

this framework, specifically, in the steps of pre-segmentation and cross-object surface mapping.

The purpose of model formation is to create mean-shape models of each bone and identify cartilage, non-cartilage and transitional regions on them. There are about 2000 vertices for each mean shape model. In addition, we collected cartilage statistic information by training a Random Forest classifier [6] based on intensity, gradient, distance to the bone, eigenvalue and corresponding local model coordinate features for each cartilage voxel in nine training images.

For the bone pre-segmentation, a 3D bounding box containing bone and cartilage for each femur, tibia and patella is first specified by users. After that, the corresponding mean shape model is fitted to the image according to the user-selected bounding boxes. The robust optimal closed surface detection algorithm with ELF searching direction was then applied iteratively yielding the pre-segmented bone surfaces. The details of graph construction for optimal closed surface detection can be found in [61]. Searching along ELF can achieve high robustness for this initial pre-segmentation step. For instance, in Fig. 6.4a, an initial tibia mean shape is positioned on a 3D image of human tibial bone. The initial mean shape may not be well positioned and after several iterations along normal directions, the solution wraps around itself near the tibial cartilage. If we want to segment cartilage based on this pre-segmentation result, a segmentation failure will likely result. Incorporating ELF paradigm in the graph construction overcomes this problem and substantially increases the robustness of the pre-segmentation step (Fig. 6.4c).

After pre-segmentation, one more vertex with ELF is interpolated at the middle of each edge on femoral and tibial bone surfaces, which up-sampled these two surfaces to about 8000 vertices each. Then, one-to-one and all-to-all correspondent pairs are generated between femur-tibia contact area as well as femur-patella contact area by constraint-point mapping technique. The correspondent pairs and their ELF direc-

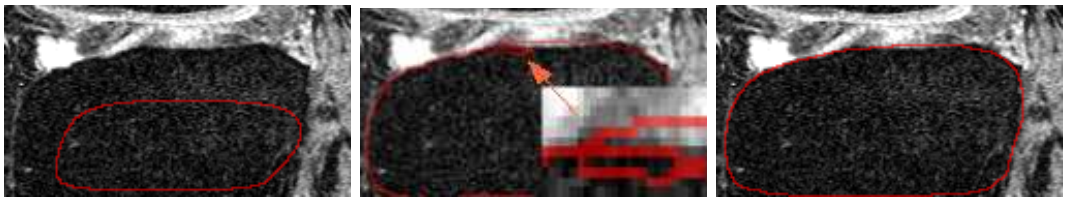

(a) (b) (c)

Figure 6.4: Tibia bone-cartilage interface segmentation in 3D performed using iterative graph searching. (a) An initial 3D contour (red line) placed on the 3D MR image of human tibia. (b) Iterative volumetric graph searching result (red line) performed along normal directions, notice the surface wrapping near the tibial cartilage that is detrimental to consequent cartilage segmentation. (c) Iterative volumetric graph searching result (red line) performed along ELF directions, no surface wrapping present – using the same initialization and the same number of iterations.

tion connections are used for inter-object graph link construction [101,102]. For graph cost design, we use gradient information as surface cost at non-cartilage region and Random Forest output unlikeness as regional cost [41] at transitional and cartilage regions. The global minimum cost solution for this graph gives optimal bone-cartilage delineation for all bones simultaneously. If no cross-object relationships are considered, the final-segmented femoral and tibial as well as femoral and patellar cartilage may overlap as shown in Fig. 6.5a and 6.5b respectively. As a comparison, Fig. 6.5c and 6.5d show the result when the proposed surface mapping is applied.

6.3 Chapter Summary

The presented method is not free of several limitation. The most significant is that the ELF definition is computationally demanding for surfaces with high vertex density. In our experiment, computing 40 points along each ELF for 2000 vertices consumes 13 seconds on our PC, which is comparable to computing Danielsson distance transform [14] for a $200 \times 200 \times 200$ volume. However, ELF computation time increases exponentially with the increase in the numbers of vertices. One of the possibilities is to merge multiple far-away vertex charges to one "larger" vertex charge

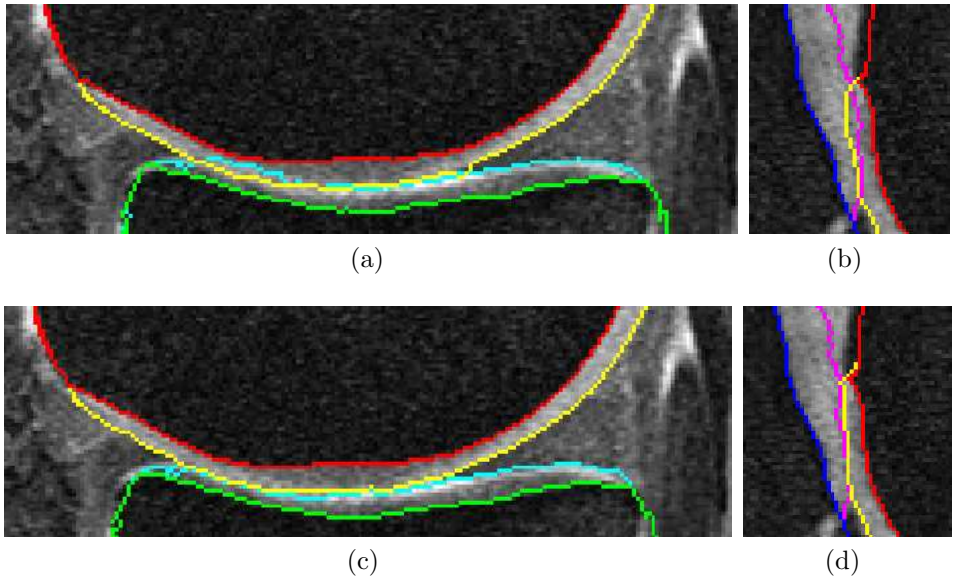

Figure 6.5: Graph-based femur-tibia-patella cartilage delineation in 3D. (a) and (b) Graph searching result not utilizing corresponding vertex pairs. Note the intersection of the identified surfaces. (c) and (d) Graph searching result using the constraint-point corresponding vertex pairs.

when computing local ELF, which will greatly decrease the total amount of vertices involved in the computation.

We have reported a new method for multiple object/multiple surface image segmentation and graph construction. In this approach, the solution-searching directions are defined according to the directions identified by the electric line field paradigm. Consequently, the search columns are formed for which the non-intersection property of the ELF guarantees non-wrapping surface segmentation outcome even when dealing with complex local surface shapes or rapid shape changes. Based on the non-intersection property, a constraint point cross-surface mapping technique was designed not requiring surface merging and preserving the surface geometry. Consequently, one-to-one and all-to-all mapping is obtained for the coupled-surface contact area. This property makes our mapping technique superior to those previously presented [49, 101, 102].

After successfully defined a non-intersected search direction as well as a one-to-one, all-to-all vertex mapping technique, a multi-object, multi-surface graph can be build with the graph columns along proposed ELF direction and inter-object graph arcs connecting corresponding vertex pairs acquired from constrained-point surface mapping. However, our work doesn't finish here. We need to design good graph cost to get accurate graph opimazation solutions.

CHAPTER 7
PATTERN RECOGNITION TECHNIQUES FOR GRAPH COST DESIGN

In graph-search based image segmentation tasks, the graph solution is driven by the cost function design. Gradient information based cost and intensity Gaussian model based cost were frequently used in the previous optimal surface detection applications [35, 84, 105]. However, notice that the anatomic structure under the same scanning protocol usually has same texture information. Using the texture information in a pattern recognition framework can greatly increase the robustness and performance of the segmentation.

7.1 Pattern Recognition Techniques

Extracting features containing desired object information to train classifiers from ground-truth-available images and using the trained classifiers to segment new images are the ideas of supervised-learning pattern recognition. This technique is widely used in medical image segmentation, because well tuned classifiers can provide robust prediction for new patterns. The classifiers can learn different kind of information from training features by combining them in a reasonable way. Moreover, the segmentation process can be fully automatic.

7.1.1 Feature collection

Theoretically, any useful information which can be evaluated quantitatively can be used as a feature. Here we introduce some typically used features in image analysis field.

7.1.1.1 Intensity-based texture features

Original image intensity, or intensities from different Gaussian kernel smoothed images contains local object appearance and texture information in different scales. Intensity information can be simply converted into local histogram measurements

and local standard deviation or other higher order of deviations (e.g. skewness or kurtosis) measurements. Gray-Level Co-occurrence Matrices (GLCM) features [43] can be also derived from local histograms.

Haar wavelet feature is defined as the differences of area intensity sums in different directions, which can be easily computed from "integral" images [90]. Due to the computation efficiency, Haar feature is successfully utilized in real-time face tracking applications [90]. Local Binary Pattern (LBP) also proved to be a useful feature for texture classification. The idea of LBP is to compare the intensity of a pixel with other pixels around a pre-defined circle and use the comparison code sequence (e.g. no less than: 1, less than 0) to create a rotation invariant codeword. The codeword works as a feature [71].

Gradient and other higher-order of derivatives of an image are well known operators to compute textures such as edges. Zheng *et al.* introduced steerable features which include a set of local intensity and gradient based features under a steerable sampling pattern [107].

7.1.1.2 Local shape-based measurements

Other commonly used features include principal components (λ values) of a Hessian image which describes local object shape appearances. For example, in 3D images, if the principle components are ordered as $|\lambda_1| \leq |\lambda_2| \leq |\lambda_3|$, then a blob-like structures may have large values of all the λ's; tubular structures have a small value for λ_1 but large values for λ_2 and λ_3; plate-like structures have small values for both λ_1 and λ_2 but a large value for λ_3. Furthermore, with different signs of λ's, the above patterns can be defined with bright objects and dark objects measurement. Based on the observation, Frangi *et al.* combine the λ values to enhance specific structures [26]. Here, a measurement R_B is used to accounts for the deviation of a blob-like structure

and distinguish it from a line- and a plate-like pattern:

$$R_B = \frac{|\lambda_1|}{\sqrt{|\lambda_2 \lambda_3|}} \tag{7.1}$$

The radio of λ_2 and λ_3 is essential for distinguishing between plate-like and line-like structures:

$$R_A = \frac{|\lambda_2|}{|\lambda_3|} \tag{7.2}$$

Finally, the normal of a Hessian matrix is helpful to eliminate background pixels:

$$S = \sqrt{\lambda_1^2 + \lambda_2^2 + \lambda_3^2} \tag{7.3}$$

Combining R_A, R_B and S into a probability-like estimation in a specific scale s may result a formula as follows:

$$v(s) = (1 - \exp(-\frac{R_A^2}{2\alpha^2})) \exp(-\frac{R_B^2}{2\beta^2})(1 - \exp(-\frac{S^2}{2c^2})) \tag{7.4}$$

where α, β and c are thresholds to adjust the sensitivity to measure R_A, R_B and S, thus to discriminate blob-like, line-like and plate-like structures. Note that $v(s)$ will be set to zero if $\lambda_2 > 0$ or $\lambda_3 > 0$ when measuring bright objects and if $\lambda_2 < 0$ or $\lambda_3 < 0$ when measuring dark objects.

$v(s)$ can be evaluated in a scaling range between s_{min} to s_{max}, the largest responds V is a good feature for specific local shape representation across a range of scales:

$$V = \max_{s_{min} \leq s \leq s_{max}} v(s) \tag{7.5}$$

7.1.1.3 Global shape-based features

While global shape information is crucial for object-oriented medical image segmentation, most features are designed to retrieve local image properties. Defining

global shape information and quantitatively assigning it to single pixel or voxel are usually not easy things. Some of the following features may carry some global shape information.

If an object is properly aligned and positioned in an image, the n-dimensional physical positions of each pixel/voxel from a set of such images contain the expansion range information of the object. As a similar feature, the voxel location is proved to be useful for cartilage segmentation [24]. If a reference object is available in an image, then the distance from a pixel/voxel to the object reflects the deviation to the reference. Still in cartilage segmentation, the reference objects can be chosen as the pre-segmented bone surfaces [32]. In deformable mesh based segmentation, if segmented meshes can be mapped to a global common reference mesh (which could be a mean shape or a unit sphere), then the corresponding coordinate on the mean shape supports local appearance discrimination ability under different global positions [63].

7.1.2 Classifier design

After collecting features, the next step for pattern recognition is to select and train classifiers. Machine learning is a very active research area in recently years. Many researchers contribute different kinds of classifier design. Some commonly used classifiers may include: *K-means* [69], *K-nearest neighbors* [12], *decision trees* [76], *neural networks* [74], *naive bayes* [17], *support vector machine* [18], *Adaboost* [29] and *Random Forest* [6].

When choosing classifiers from them, we should consider the characteristics of 3D medical image segmentation tasks:

1. The number of features collected from an image is usually between 10 to 20.

2. The number of manually labeled samples in a 3D image can be in a level of one to several million.

3. Fast online testing time is desired, while the offline training time is usually not

concerned.

4. Outliers exist in the training data due to the limitation of manual tracing accuracy.

5. The classifiers should provide good and robust classification/regression result.

In short, we should select classifiers which can handle large training dataset, robust, accurate and with fast testing speed. Adaboost and Random Forest are two classifiers satisfying the above requirements.

7.1.2.1 Adaboost classifier

The *Adaboost* classifier [29] is composed of a set of weak classifiers (e.g. one node decision tree – *Decision Stumps* [76]). In training process, the training samples are initialized with the same weights. The weak classifiers are trained one-by-one by finding the minimum weighted error. The weights for samples are adjusted after each weak classifier is trained, so that the next weak classifier will more concentrate on the wrongly segmented samples. In testing process, the output of an Adaboost classifier is a weighted sum of each weak classifier's output. Algorithm 1 shows the training and testing process of Adaboost. The Adaboost classifier can efficiently decrease generalization errors for training samples and generate robust and fast estimations. Furthermore, the Adaboost classifier can process large amount of training samples; and it provides feature selection result by avoiding correlations between features. The number of weak classifiers is the only parameter needed to be determined during the classifier design. However, because Adaboost does not tend to be over-trained with the increase of weak classifiers, the selection of this parameter is robust.

7.1.2.2 Random Forest classifier

Random Forest [6] is a more sophisticated classifier design. It uses *Decision Tree* [76] as weak classifiers. Each tree is trained by a new training set generated

Algorithm 1 Adaboost training and testing process

Adaboost Training:

Input: training samples $S = \{(x_1, y_1) \dots (x_N, y_N)\}$ where x_n is feature, $y_n \in \{-1, +1\}$ is label, number of iterations T

Initialization: sample weight $d_n^{(1)} = 1/N$ for all $n = 1, 2 \dots N$

for $t = 1$ to T **do**

Train a weak classifier with respect to the weighted sample set $\{S, d^t\}$ and obtain classification rules h_t, $h(x) \in \{-1, +1\}$

Calculate the weighted training error z_t for h_t:

$$z_t = \sum_{n=1}^{N} d_n^{(t)} \text{ for all } h_t(x) \neq y_n$$

Break if $z_t = 0$ or $z_t \geq 1/2$ and set $T = t - 1$

Set weak classifier weight α_t:

$$\alpha_t = \frac{1}{2} \log \frac{1 - z_t}{z_t}$$

Update sample weight:

$$d_n^{(t+1)} = d_n^{(t)} \exp\left(-\alpha_t y_n h_t(x_n)\right)$$

Normalize sample weights such that $\sum_{n=1}^{N} d_n^{(t+1)} = 1$

end for

Adaboost Testing:

Input: testing feature x

Output: estimation $\hat{y} = \sum_{(t=1)}^{T} \frac{\alpha_t}{\sum_{t=1}^{T} \alpha_t} h_t(x)$

by uniformly sampling the original training set with replacement (samples in original training set allowed to be selected multiple times). The generated new training set has the same number of samples as the original training set. This is called a *Bootstrap aggregating* (*Bagging*) [6] process. The Bagging process can increase the stability and robustness and decrease the variance and overfitting of the global classifier. Moreover, each leaf of a tree is trained by a number of randomly selected features and the whole tree is trained without pruning. The output of a Random Forest is the average of the total decision tree's outputs. The training and testing processes are shown in Algorithm 2. This classifier can also handle large training dataset and produce robust estimation. In certain medical image segmentation applications, Random Forest classifier performs better than other classifiers [98]. There are two parameters to be determined: the number of trees and the number of features to train each leaf. Similar with Adaboost, the number of trees is a robust parameter regarding to overfitting; and the number of features can be selected in a large range, usually as a square root of total features for probability predication Random Forest.

Algorithm 2 Random Forest training and testing process

Random Forest Training:

Input: training samples $S = \{(x_1, y_1) \dots (x_N, y_N)\}$ where x_n is feature, $y_n \in \{-1, +1\}$ is label, number of trees T, number of features m to train each leaf on a tree.

for $t = 1$ to T **do**

Uniformly sampling original training set with replacement to generate new training set.

Train a binary decision tree with generated training set and without pruning. Each leaf of the tree is trained only by randomly selected m features.

end for

Random Forest Testing:

Input: testing feature x

Output: the average of all T decision tree output

7.2 Chapter Summary

Although quite powerful, pattern recognition technique also has bottleneck in incorporating global shape information and suffers slow speed for voxel-based classification in medical image segmentation applications. As a solution, many researchers design classifier outputs as the external force for shape model-based segmentation.

Due to the flexibility of cost design, the inverse of the probability provided by classifiers can be directly embedded into a graph-search based optimal surface detection framework to perform globally optimal surface and region detection under a priori shape constrain. In the next chapter, I will show how to use this idea as well as LOGISMOS utility to build a fully automated knee cartilage segmentation system.

CHAPTER 8
LOGISMOS-BASED SEGMENTATION OF CARTILAGES FOR ALL BONES IN THE KNEE JOINT

Following the general outline of our LOGISMOS approach, a method for simultaneous segmentation of bone and cartilage surfaces in the femur, tibia, and patella, which all articulate in the knee joint, is reported. Problem-specific details of the individual processing steps outlined above are given in the next sections.

Three bones articulate in the knee joint: the femur, the tibia, and the patella. Each of these bones is partly covered by cartilage in regions where individual bone pairs slide over each other during joint movements. For assessment of the knee joint cartilage health, it is necessary to identify six surfaces: femoral bone, femoral cartilage, tibial bone, tibial cartilage, patellar bone, and patellar cartilage. In addition to each connected bone and cartilage surface mutually interacting on a given bone, the bones interact in a pairwise manner – cartilage surfaces of the tibia and femur and of the femur and patella are in close proximity (or in frank contact) for any given knee joint position. Clearly, the problem of simultaneous segmentation of the six surfaces belonging to three interacting objects is well suited for application of the LOGISMOS method.

8.1 Method

8.1.1 Bone pre-segmentation

Fig. 8.1 shows the flowchart of our method. As the first step, the volume of interest (VOI) of each bone, together with its associated cartilage, is identified using an Adaboost approach in 3D MR images (Fig. 8.1a). Following application of a 3D median filter (radius one voxel) to remove local noise, image intensities are normalized as suggested in [32]. Inspired by the facial recognition work of Viola and Jones [90], their idea was extended to 3D. Nine types of 3D Haar-like features were designed as shown in Fig. 8.2, in which the total voxel intensity sum in the white area is subtracted

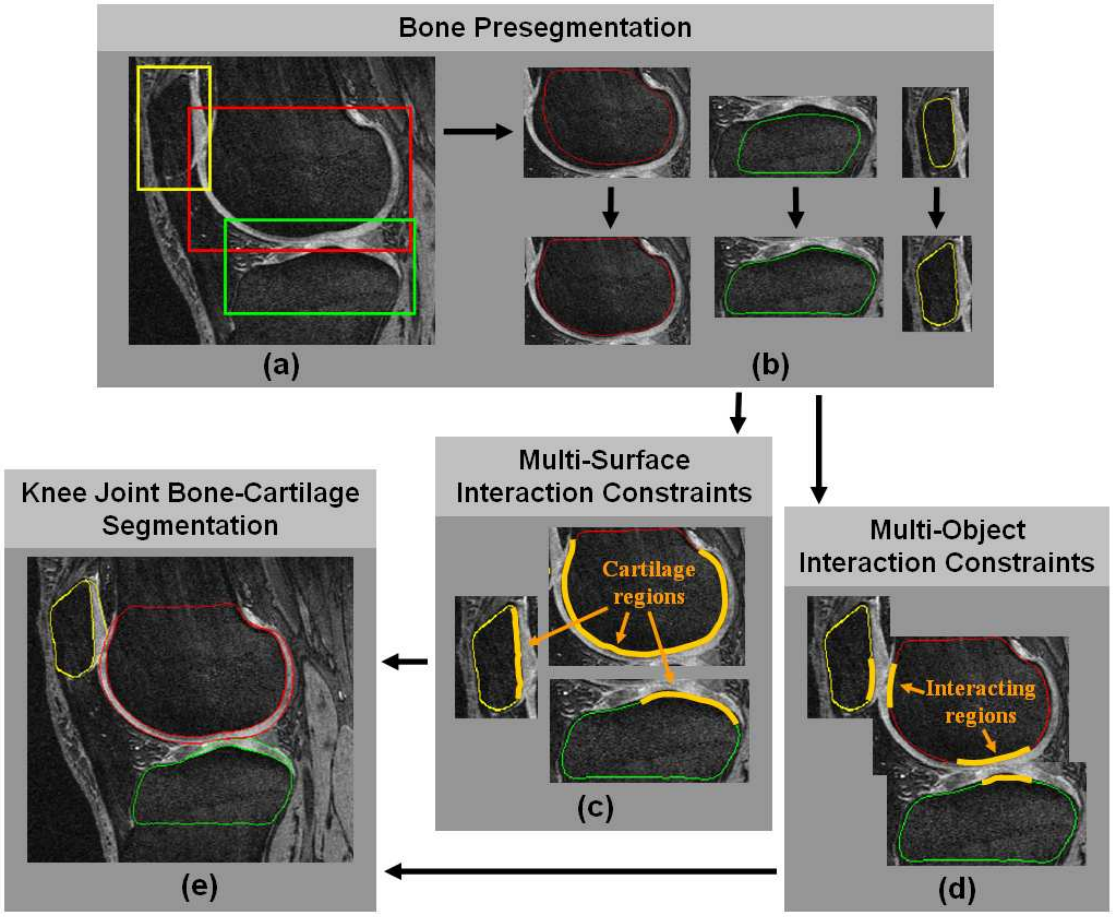

Figure 8.1: The flowchart of LOGISMOS based segmentation of articular cartilage for all bones in the knee joint. (a) Detection of bone volumes of interest using Adaboost approach. (b) Approximate bone segmentation using single-surface graph search. (c) Generation of multi-surface interaction constraints. (d) Construction of multi-object interaction constraints. (e) LOGISMOS-based simultaneous segmentation of 6 bone & cartilage surfaces in 3D.

from the total voxel intensity sum in the gray area. It is efficient to compute these features in an integral image [90] using 12, 16, and/or 18 index references (types $a \sim c$, $d \sim f$, and $g \sim i$, respectively). Furthermore, computing the Haar-like features in multiple resolutions can be achieved by rescaling the box sizes shown in Fig. 8.2, which avoids re-sampling the entire image and thus leads to a single cross-scale classification process. The goal of the bone localization is to determine three VOIs per knee joint image within which the individual bones (femur, tibia, patella) are located.

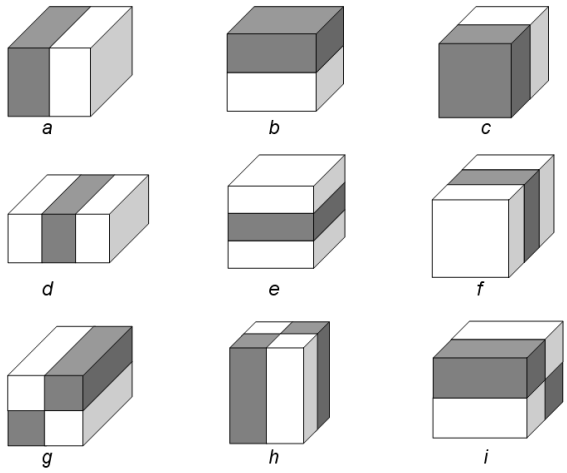

Figure 8.2: Nine types of 3D Haar-like features, employed in a multi-scale manner.

To learn VOI-related 3D Haar-like features from a training set of images, example VOIs were manually identified in a TRAIN-1 dataset (Section 8.2.2) that was completely separate from any testing image sets used later. The example VOIs included the femoral, tibial, and patellar bone and cartilage structures (Fig. 8.1a). After scaling to the mean size for each bone, the bone VOIs were used as representative bone class (foreground) samples. A large number of 3D Haar-like features (∼150,000) of different types and scales were computed inside the foreground VOI location in each

training image. The mean±standard deviation (std) of the VOI sizes were computed for each bone, as well. To determine VOI-related features for non-bone (background) VOI locations, these VOI positions were perturbed – randomly shifted nine times for each axis and each training image within an experimentally set 2.8 – 21 mm range – to produce background class samples. In the course of Adaboost training, the 500 most appropriate features were identified. Three Adaboost classifier results were obtained separately for each of the three bones.

To detect the femur, tibia, and patella bones in 3D MR images, the selected 500 features are computed within each VOI in all possible VOI positions in a multi-resolution fashion (VOI sizes ranging within mean±3 std of the learned VOI size). Detection of the three bones is sequential and starts with the femur, since it has the most recognizable appearance. The tibia is then localized as inferior of the femur, and the patella to the anterior of the femur as shown in Fig. 8.1a.

After localizing the object VOIs, approximate surfaces of the individual bones must be obtained (Fig. 8.1b). For the purpose of accurate delineation of knee bone and cartilage structures as imaged by MR, the bone surfaces alone provide an initial approximation of the pair of inter-related bone and cartilage surfaces. Using a separate training set TRAIN-2 (Section 8.2.2) for which complete manual tracings of all three bones were available in all image slices, mean shapes of the three bones were constructed and represented as closed surfaces, of about 2000 mesh vertices each. Using the volumetric bone surface meshes, a random forest classifier [6] was trained to distinguish the bone surface from the rest of the image. The utilized features included intensity, intensity gradient, and second order intensity derivatives calculated in Gaussian-smoothed images constructed using 0.5 mm, 1.0 mm, and 2.0 mm smoothing kernels. Additional features were derived from the distances between the geometric center of the bone VOI and the true bone surface, and served as shape-bearing information. All these features formed the input to the random forest

classifier.

The approximate bone surfaces were identified in previously unseen images by first roughly fitting the mean bone shape models obtained from the TRAIN-2 training set directly to the automatically-identified VOIs (upper panels of Fig. 8.1b). A single surface detection graph was constructed based on the fitted mean shapes – graph columns were built along non-intersecting electric lines of force to increase the robustness of the graph construction (Chapter 6). The surface costs were associated with each graph node based on the inverted surface likelihood probabilities provided by the random forest classifiers. After repeating this step iteratively until convergence (usually 3–5 iterations were needed), the approximate surfaces of each bone were automatically identified, without considering any bone-to-bone context, see lower panel of Fig. 8.1b.

8.1.2 Multi-surface interaction constraints

Image locations adjacent to and outside of the bone may belong to cartilage, meniscus, synovial fluid, or other tissue, and they thus exhibit different image appearance (Fig. 8.1c). For example, the cartilage and non-cartilage regions along the knee bone surface differ dramatically in texture. Features utilized in a respective cartilage/non-cartilage tissue classifier include those used previously (intensity, intensity gradient, and second order derivatives of Gaussian-smoothed images). Additional features were added, including the physical distances of a location from the bone surface [32] and three eigenvalues of the Hessian image. To reveal the cartilage shape properties in different locations, each graph node was mapped back to the mean bone shape along a given search direction. The original vertex coordinates of the corresponding vertex on the mean bone shape were used as yet another feature [63].

Using the cartilage features collected from the training dataset TRAIN-2 for all cartilage/non-cartilage locations, a new Adaboost classifier was trained for each bone. When segmenting the bone surface, these Adaboost classifiers quickly classify the

graph nodes into one of the cartilage/non-cartilage classes. If any node along a search direction is identified as cartilage, the search path is identified as passing through the cartilage region.

The overall goal of this work is to extract from MR images the bone and cartilage surfaces of each of the three bones forming the knee joint (6 surfaces in total). Since the cartilage generally covers only those parts of the respective bones which may articulate with another bone, two surfaces (cartilage & bone) are defined only at those locations, while single (bone) surfaces are to be detected in non-cartilage regions. This also reflects the distinction between truly external bone surfaces versus the subchondral bone surface, which marks the interface between bone and cartilage where they are joined. To facilitate a topologically robust problem definition across a variety of joint shapes and cartilage disease stages, two surfaces are detected for each bone, and the single–double surface topology differentiation reduces into differentiation of zero and non-zero distances between the two surfaces. In this respect, the non-cartilage regions along the external bone surface were identified as regions in which zero distance between the two surfaces was enforced so that the two surfaces collapsed onto each other, effectively forming a single bone surface. In the cartilage regions, the zero-distance rule was not enforced, providing for both a subchondral bone and articular cartilage surface segmentation.

8.1.3 Multi-object interaction constraints

In addition to dual-surface segmentation that must be performed for each individual bone, the bones of the joint interact in the sense that cartilage surfaces from adjacent bones cannot intersect each other, cartilage and bone surfaces must coincide at the articular margin, the maximum anatomically feasible cartilage thickness shall be observed, etc. The regions in which adjacent cartilage surfaces come into contact are considered the interacting regions (Fig. 8.1d). In the knee, such interacting regions exist between the tibia and the femur (tibiofemoral joint) and between

the patella and the femur (patellofemoral joint). It is also desirable to find these interacting regions automatically.

For this purpose, an iso-distance medial separation sheet is identified in the global coordinate system midway between adjacent pre-segmented bone surfaces. If a vertex is located on an initial surface while having a search direction intersecting the sheet, the vertex is identified as belonging to the region of surface interaction. The separation sheet can be identified using signed distance maps even if the initial surfaces intersect. Following the ELF approach described above, femoral and tibial initial surfaces were up-sampled to approximately 8,000 vertices each in order to increase the surface resolution. Then, one-to-one and all-to-all corresponding pairs are generated between femur-tibia contact area as well as femur-patella contact area by constraint-point mapping technique. The corresponding pairs and their ELF connections are used for inter-object graph link construction [101, 102].

8.1.4 Knee joint bone-cartilage segmentation

After completion of the above steps, the segmentation of multiple surfaces of multiple mutually interacting objects can be solved as previously presented in [101]. Consequently, all surfaces are segmented simultaneously and globally optimally subject to the interaction constraints (Fig. 8.1e). Specifically, double surface segmentation graphs were constructed individually for each bone using that bone's initial surface. The three double surface graphs were further connected by inter-object graph arcs between the corresponding columns identified during the previous step as belonging to the region of close-contact object interaction. The minimum distance between the interacting cartilage surfaces from adjacent bones was set to zero to avoid cartilage overlap.

After the step of cost translation [62], the constructed interacting graph is a directed graph $\tilde{G}$ derived from a properly-ordered multi-column graph G. As stated before, a V-weight net problem in G can be converted to finding the minimum non-

empty closed set in $\tilde{G}$. This can be done by an s-t cut algorithm, e.g. [4], as a result of which all six surfaces (femoral bone-cartilage, tibial bone-cartilage and patellar bone-cartilage) are detected simultaneously.

8.1.5 Cost functions

Pattern recognition can substantially aid image segmentation. Due to the flexibility of the cost function design, pattern recognition techniques can be embedded directly in the optimal surface detection framework.

Inspired by the work of Folkesson and Fripp [24, 32], a random forest classifier [6] was trained for each bone using voxels surrounding the corresponding bone boundaries. Intensity, gradient and second order intensity derivatives under Gaussian smoothed images with 0.5 mm, 1.0 mm, 2.0 mm smoothing kernels were used as features. Furthermore, 3D distances from the center of the VOI were utilized as shape-information-bearing features, yielding a more robust behavior than using global 3D location as features [24]. All these features have already been described in Section 8.1.1. The surface cost was associated with each graph node based on the inverted surface probabilities provided by the Random Forest classifiers.

Three additional binary Random Forest classifiers were trained based on the training samples (labeled as either cartilage or other). For this training, only samples from the cartilage-present bone regions were utilized, obtained from the TRAIN-2 set. The same features as previously used for cartilage/non-cartilage detection were used (Section 8.1.2).

Once trained and applied to previously unseen to-be-segmented images, the classifiers provide localized information for each location of the graph nodes about the likelihood that this location belongs to a given tissue class (cartilage or other). Inverted tissue probabilities are therefore associated with each graph node and represent regional cost terms.

8.2 Experimental Methods

8.2.1 Image data

The goal of the performance assessment was to determine the surface segmentation accuracy obtained when simultaneously segmenting 6 bone and cartilage surfaces in the knee joint (femoral bone and cartilage, tibial bone and cartilage, patellar bone and cartilage) in full 3D. MR images utilized in this study were randomly selected from the publicly available Osteoarthritis Initiative (OAI) database, which is available for public access at http://www.oai.ucsf.edu/.

The knees of subjects in the OAI study exhibit differing levels of joint degeneration. By study design, subjects are enrolled into one of two cohorts, based on whether they have symptomatic knee osteoarthritis (OA) at the time of entry into the study (progression cohort) or they do not (incidence cohort). The MR images used were acquired with a 3T scanner following a standardized procedure. A sagittal 3D dual-echo steady state (DESS) sequence with water-excitation and the following imaging parameters: image stack of 384×384×160 voxels, with voxel size 0.365×0.365×0.70 mm.

8.2.2 Independent standard

The initial bone segmentation relied upon the TRAIN-1 training set, which consisted of 25 randomly selected OAI image datasets in which bone VOIs were manually identified. The remaining training steps were performed using a training set (TRAIN-2) that consisted of 9 image datasets, taken from the incidence cohort (4 subjects) and from the progression cohort (5 subjects). Complete volumetric bone and cartilage tracing was manually performed for the three bones of the knee joint in the TRAIN-2 datasets. The performance of the LOGISMOS method was tested in the TEST dataset of 60 OAI subjects for which volumetric tracings were available either in coronal orientation (1618 traced slices, 40.5±4.7 traced slices per dataset), or in sagittal orientation (2266 traced slices, 113.3±9.8 per dataset). In 20 of the 60 datasets,

the femoral, tibial and patellar bone and cartilage borders were expert-traced in all sagittal-view slices by one observer. In the remaining 40 datasets, femoral and tibial bone and cartilage borders were expert-traced in all of the coronal-view slices by two other observers. The independent standard thus resulted from fully manual tracing with no automated or semi-automated segmentation tool assistance, and expected inter-observer variability.

8.2.3 Parameters of the method

For preliminary segmentation, the surface smoothness was set as $\Delta = 3$ vertices. Due to anisotropic voxel sizes, Δ ranged from 1.04 to 2.1 mm based on the direction in the 3D volume. Similar directionality-caused ranges apply to other parameters. Following the bone pre-segmentation, the femoral and tibial surfaces were upsampled from about 2000 vertices to 8000 vertices each.

For the final-segmentation graph construction, vertices were sampled in a narrow band of [-5,20] voxels (-3.5 – 14 mm) along the ELF direction around the pre-segmented surface (upsampled to $K = 51$). The surface smoothness parameters were set to $\Delta = 3$ vertices (1.04–2.1 mm) for both the bone and cartilage surfaces. During the ELF computation, $m = 4$ was used in Equation (6.3). The inter-surface distance constraint values were set to $\delta_{lower} = 0$ to allow for denuded bone and $\delta_{upper} = 0$ at non-cartilage area to create coincident bone and cartilage surfaces. The inter-object surface smoothness parameter was $\delta^l = 0$ to prevent cartilage surface overlapping.

8.2.4 Quantitative assessment indices

To provide a detailed assessment of the cartilage segmentation accuracy, signed and unsigned surface positioning errors were assessed in each of the 60 images from the TEST set, and they are reported as mean ± standard deviation in millimeters. Surface positioning errors were defined as the shortest 3D distances between the independent standard and computer-determined surfaces. Similarly, local cartilage

thickness was measured as the closest distance between the cartilage and bone surfaces and compared to the independent standard.

To determine Dice Similarity Coefficients (DSC) [15] of cartilage segmentation performance, complete volumetric tracings of the entire joint must be available, as in the TRAIN-2 dataset. Therefore, DSC analysis of the cartilage volume was performed in the TRAIN-2 dataset following a leave-one-out training/testing strategy to maintain full training/testing separation.

8.3 Results

All testing datasets were segmented using the described fully automated framework. No user-interaction was allowed in any of the segmentation steps and no resulting surfaces were manually edited. The segmentation required roughly 20 minutes on average to segment one knee joint dataset, on a PC with Intel Core 2 Duo 2.6 GHz processor and 4 GB of RAM (single thread). Out of the 20 minutes, the bone VOI locating process takes about 6 minutes per dataset on average (all three bones) with no location errors observed. The subsequent step of pre-segmenting one bone surface requires about 2 minutes each and can be performed in parallel. All remaining steps of the multi-object multi-surfaces simultaneous segmentation need about 8 minutes to complete. Fig. 8.3 shows an example of a knee joint contact area slice from the 3D MR dataset. Note the contact between the femoral and tibial cartilage surfaces, as well as the contact between the femoral and patellar cartilage surfaces. Furthermore, there is an area of high intensity synovial fluid adjacent to the femoral cartilage that is not part of the cartilage tissue and should not be segmented as such. The right panel of Fig. 8.3 shows the resulting segmentation demonstrating very good delineation of all six segmented surfaces and correct exclusion of the synovial fluid from the cartilage surface segmentations. Since the segmentations are performed simultaneously for all 6 bone and cartilage surfaces in the 3D space, computer segmentation directly yields the 3D cartilage thickness for all bone surface locations. Typical segmentation results

are given in Fig. 8.10 and 8.11.

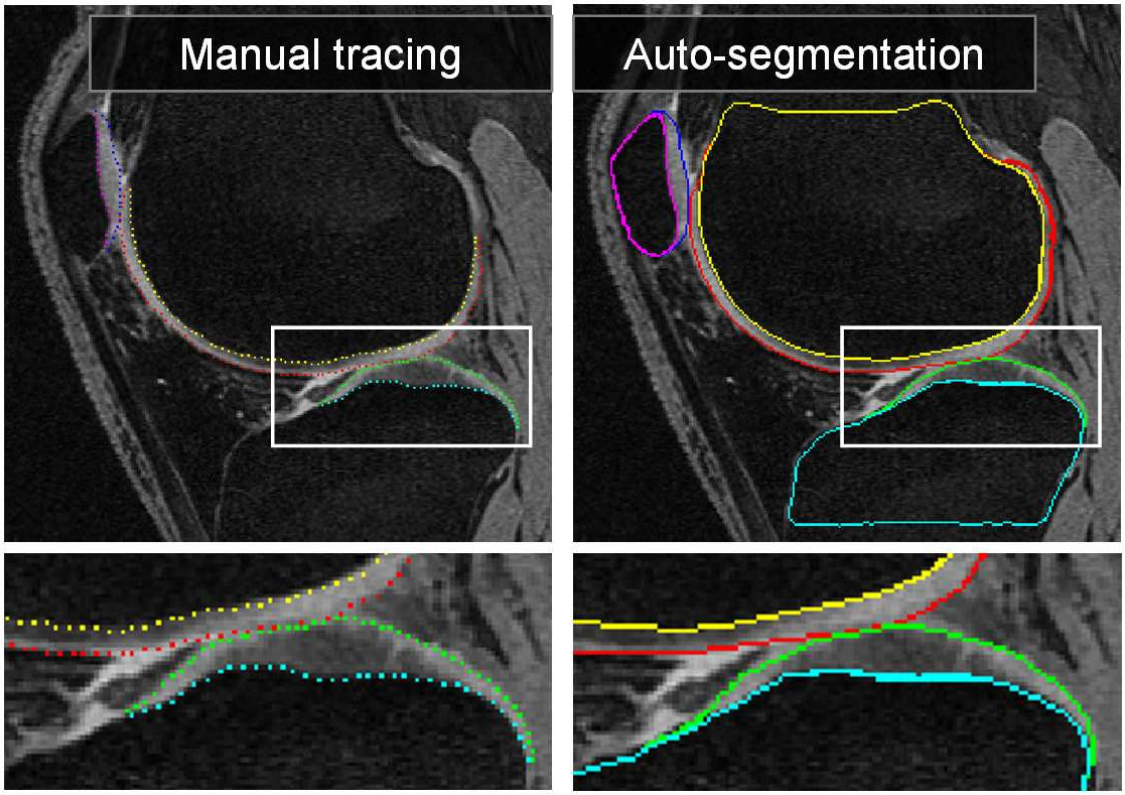

Figure 8.3: MR image segmentation of a knee joint – a single contact-area slice from a 3D MR dataset is shown. Segmentation of all 6 surfaces was performed simultaneously in 3D. (left) Original image data with expert-tracing overlaid. (right) Computer segmentation result. Note that the double-line boundary of tibial bone is caused by intersecting the segmented 3D surface with the image plane.

The signed and unsigned surface positioning errors of the obtained cartilage segmentations were quantitatively measured over the cartilage regions, and they are presented in Table 8.3. For these results, the femoral bone and cartilage errors, as well as tibial bone and cartilage errors, were evaluated in each of the 60 testing datasets. The patellar bone and cartilage errors were evaluated in the 20 testing datasets for which sagittal patellar tracings were available. The average signed surface positioning errors for the 6 detected surfaces ranged from 0.04 to 0.16 mm, while the average

unsigned surface positioning error ranged from 0.22 to 0.53 mm. The close-to-zero signed positioning errors attest to a very small bias of surface detection. The unsigned positioning errors show that the local fluctuations around the correct location are much smaller than the 3D diagonal of the MR image voxel (0.87 mm). Our results therefore show virtually no surface positioning bias and subvoxel local accuracy for each of the 6 detected surfaces. Signed positioning error maps for femoral and tibial bone and cartilage surfaces and for calculated cartilage thickness are shown in Fig. 8.15 demonstrating that the mean errors are small for all three cartilage areas across all central regions of greatest functional significance. The detailed surface positioning errors for all six surfaces in each dataset are plotted in Fig. 8.4 to 8.9.

Table 8.1: Mean signed and unsigned errors of computer segmentation in comparison with the independent standard in mm.

ERRORS (mm)	Signed Bone Positioning	Signed Cartilage Positioning	Unsigned Bone Positioning	Unsigned Cartilage Positioning	Signed Mean Cartilage Thickness
Femur	0.04 ± 0.12	0.16 ± 0.22	0.22 ± 0.07	0.45 ± 0.12	0.11 ± 0.24
Tibia	0.05 ± 0.12	0.10 ± 0.19	0.23 ± 0.06	0.53 ± 0.11	0.05 ± 0.23
Patella	0.09 ± 0.09	0.12 ± 0.21	0.23 ± 0.11	0.53 ± 0.14	0.03 ± 0.17

When assessing the performance using Dice coefficients, the obtained DSC values were 0.84, 0.80 and 0.80 for the femoral, tibial and patellar cartilage surfaces, respectively, as shown in Table 8.2. The detailed assessments for femoral, tibial and patellar cartilages for each dataset are in Fig. 8.12, 8.13 and 8.14 respectively.

8.4 Chapter Summary

In this section, we focus on three issues associated with the reported multi-object multi-surface segmentation framework: overall properties, novelty and generality of

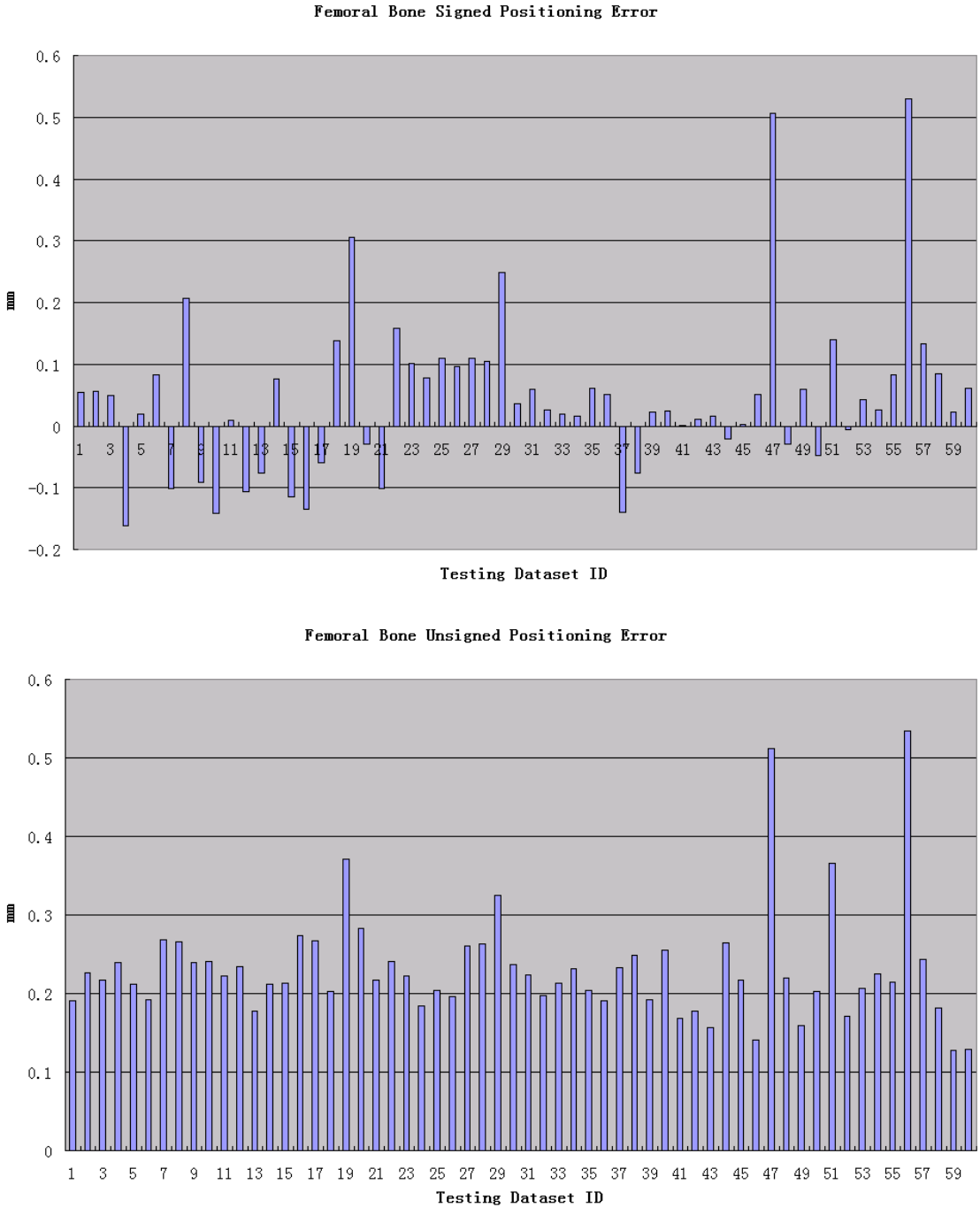

Figure 8.4: Charts for individual femoral bone surface positioning error measurements

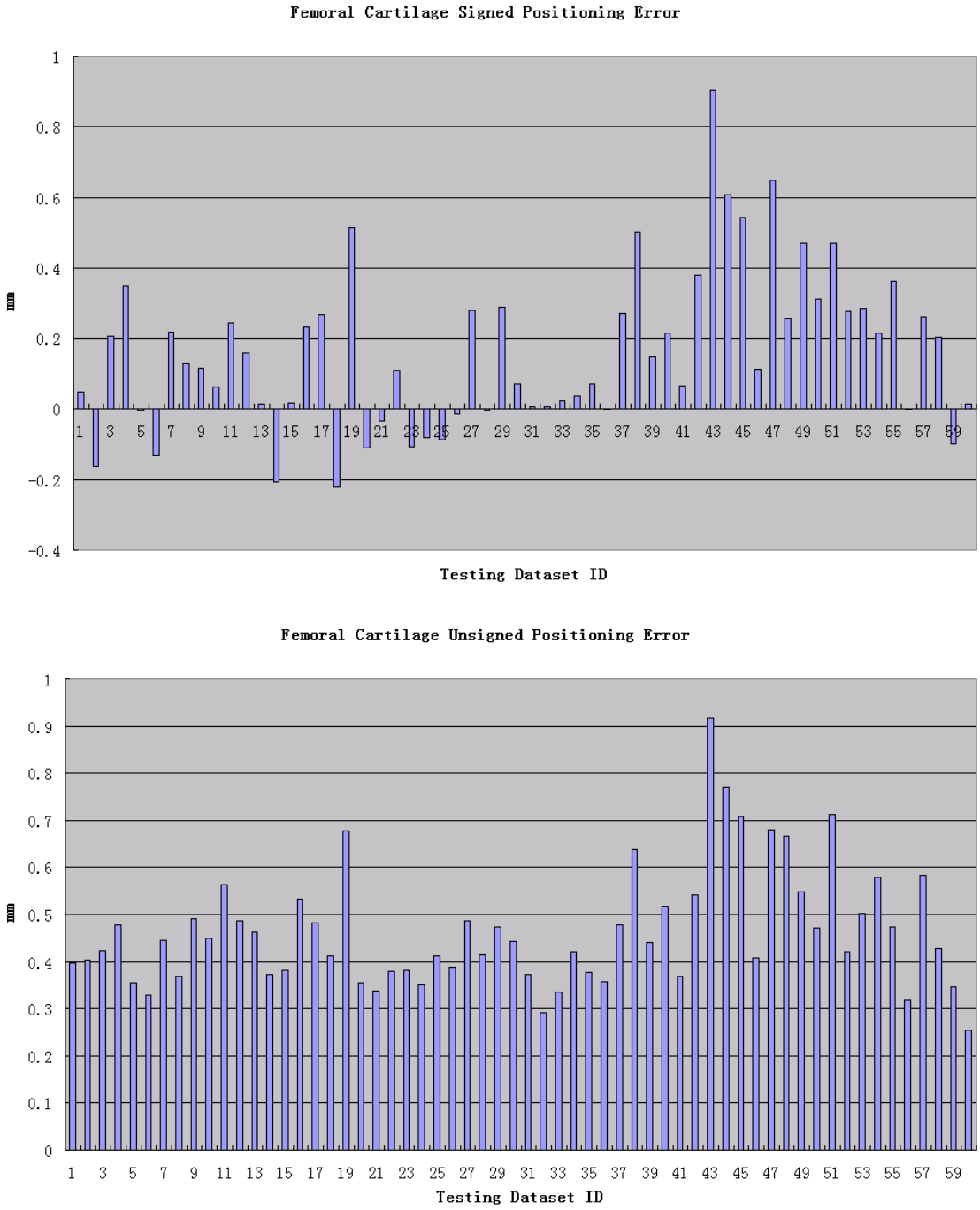

Figure 8.5: Charts for individual femoral cartilage surface positioning error measurements

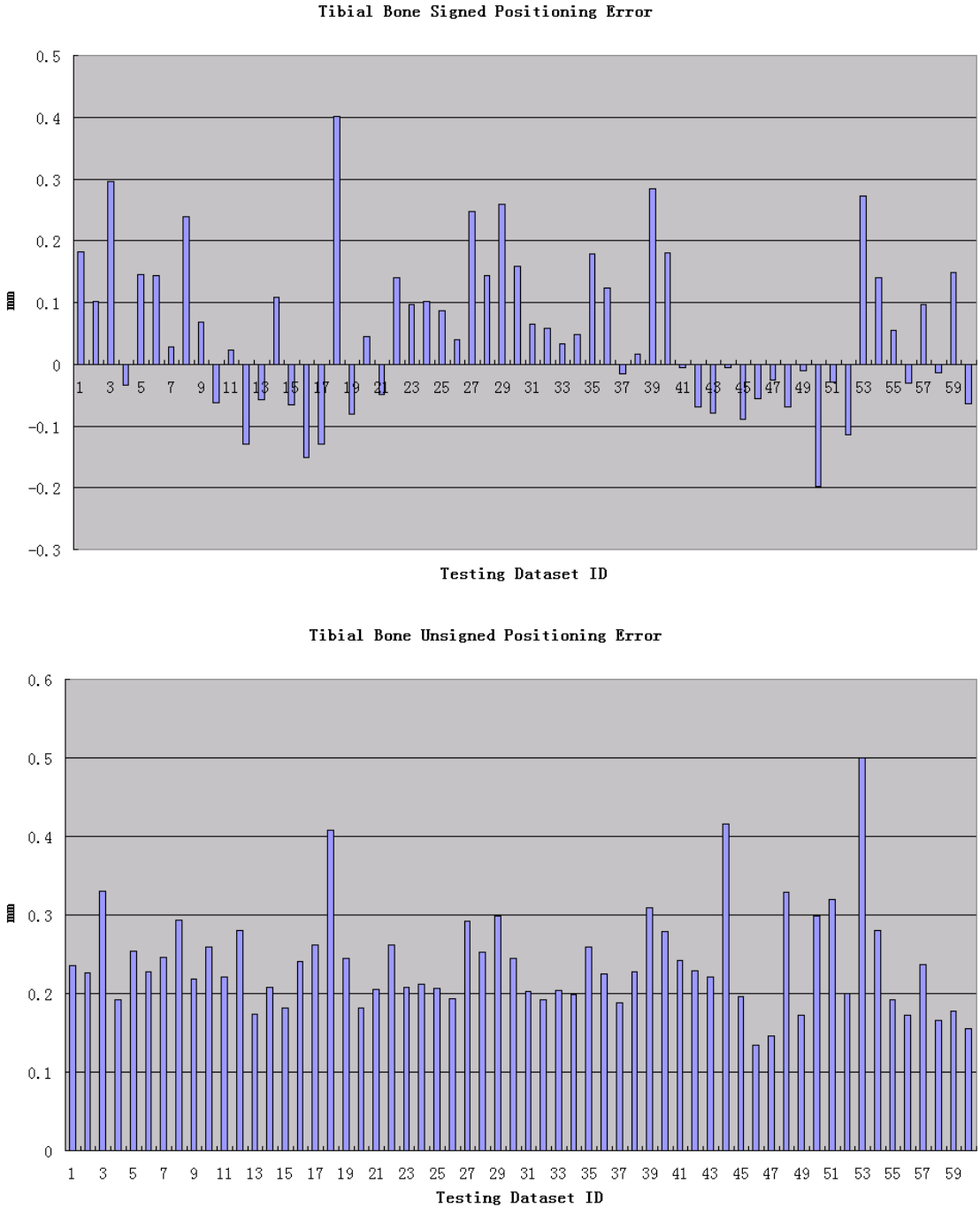

Figure 8.6: Charts for individual tibial bone surface positioning error measurements

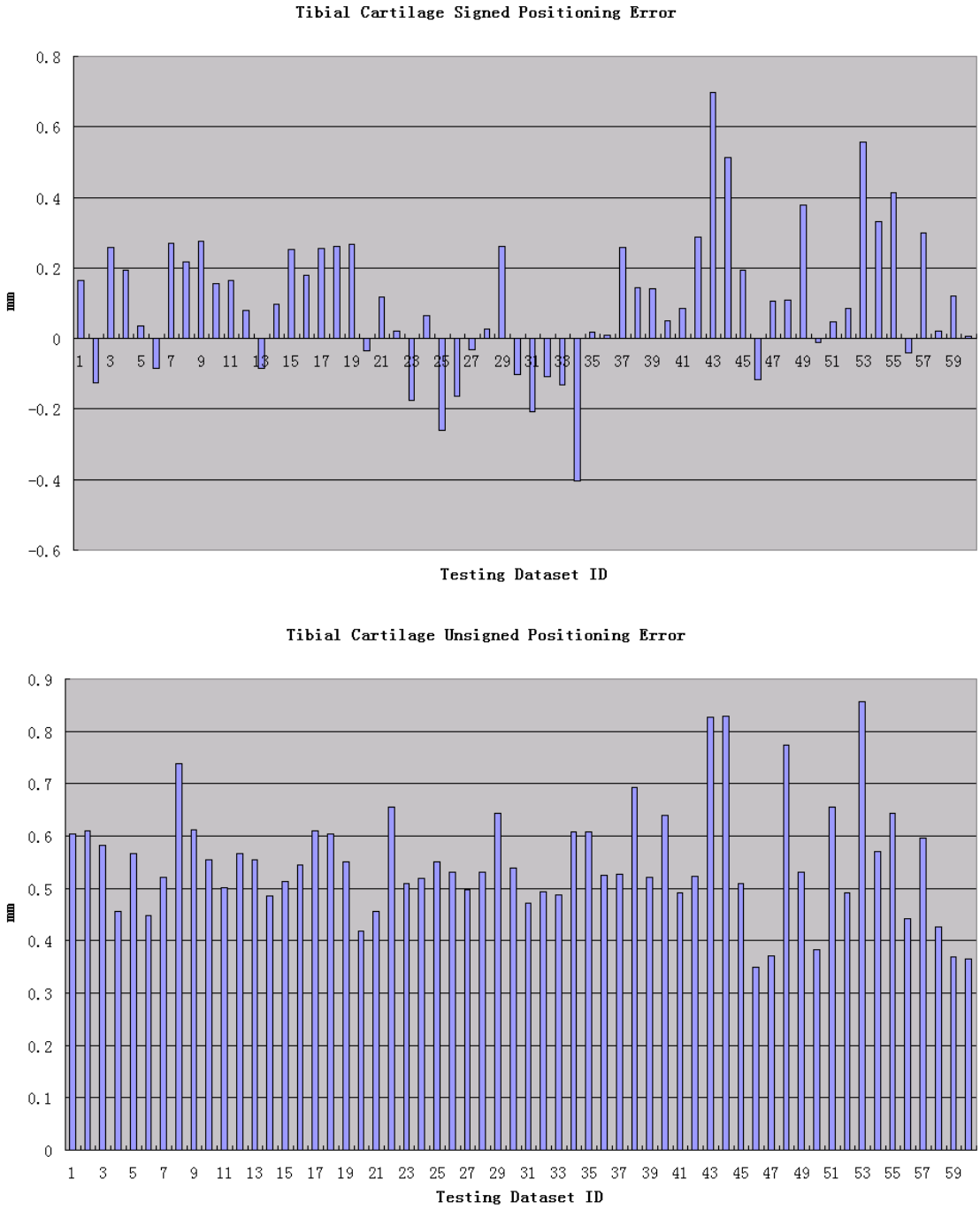

Figure 8.7: Charts for individual tibial cartilage surface positioning error measurements

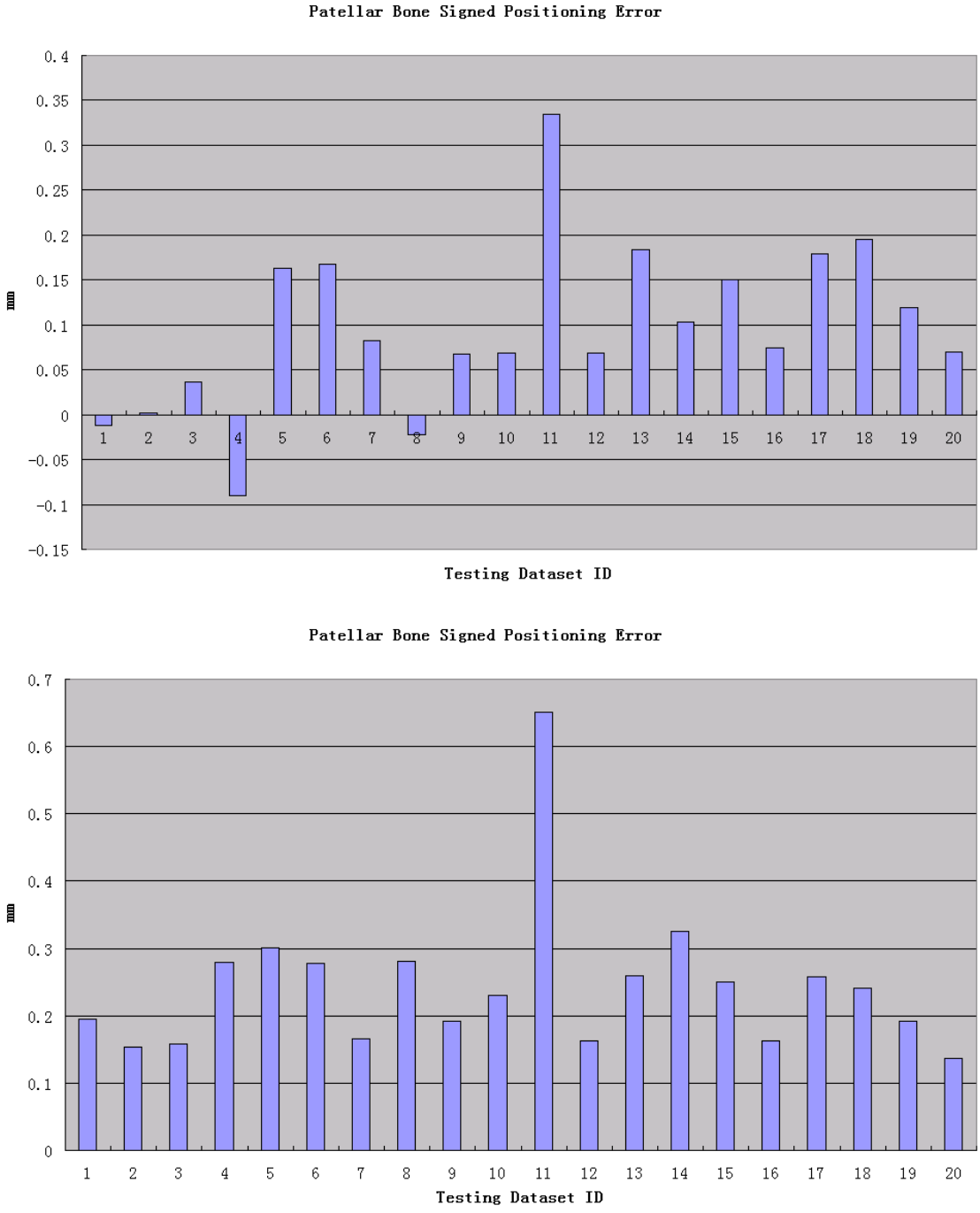

Figure 8.8: Charts for individual patellar bone surface positioning error measurements

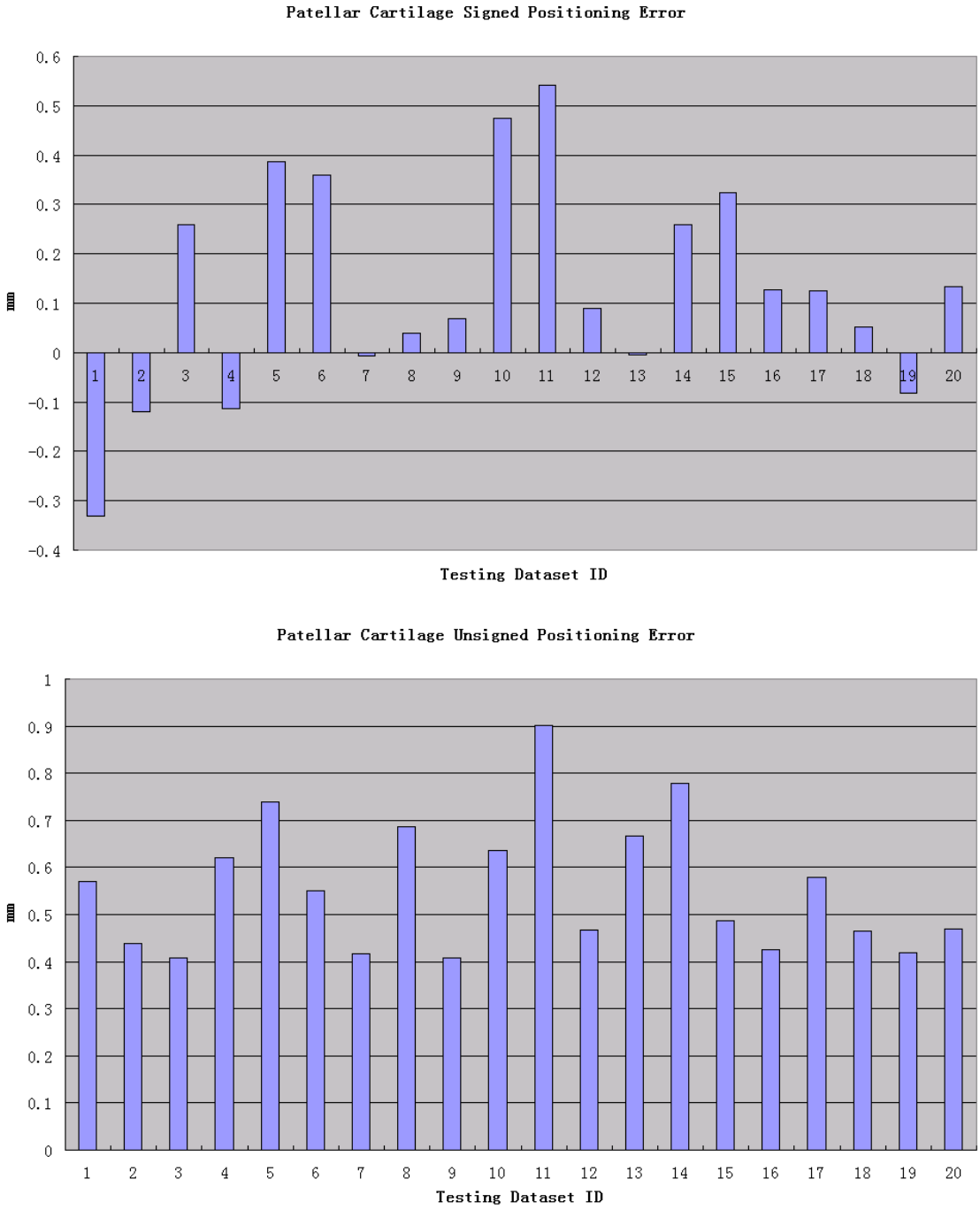

Figure 8.9: Charts for individual patellar cartilage surface positioning error measurements

Table 8.2: Volume measurement in comparison with the independent standard.

	DSC	Sensitivity	Specificity
Femoral cartilage	0.84 ± 0.04	0.80 ± 0.07	1.00 ± 0.00
Tibial cartilage	0.80 ± 0.04	0.75 ± 0.08	1.00 ± 0.00
Patellar cartilage	0.80 ± 0.04	0.76 ± 0.08	1.00 ± 0.00

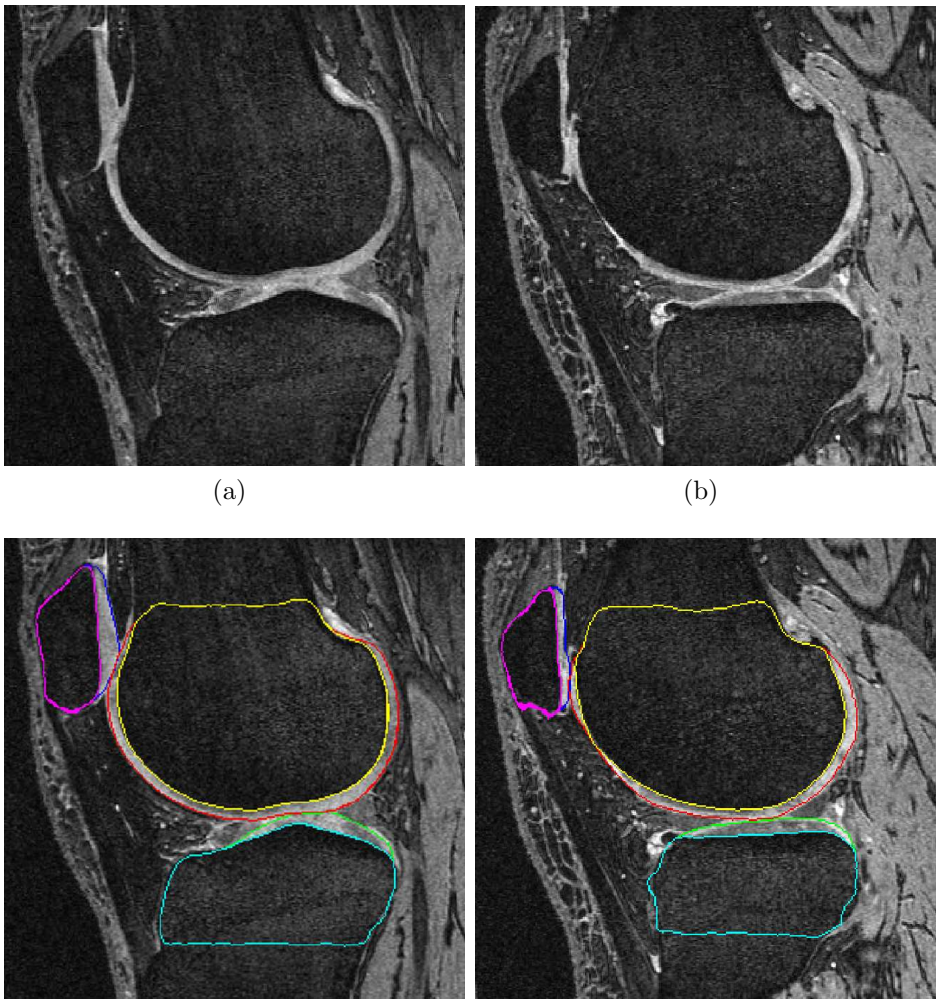

(a) (b)

(c) (d)

Figure 8.10: 3D segmentation of knee cartilages. Images from a knee minimally affected by osteoarthritis shown on the left. Severe cartilage degeneration shown on the right. (a,b) Original images. (c,d) The same slice with bone/cartilage segmentation.

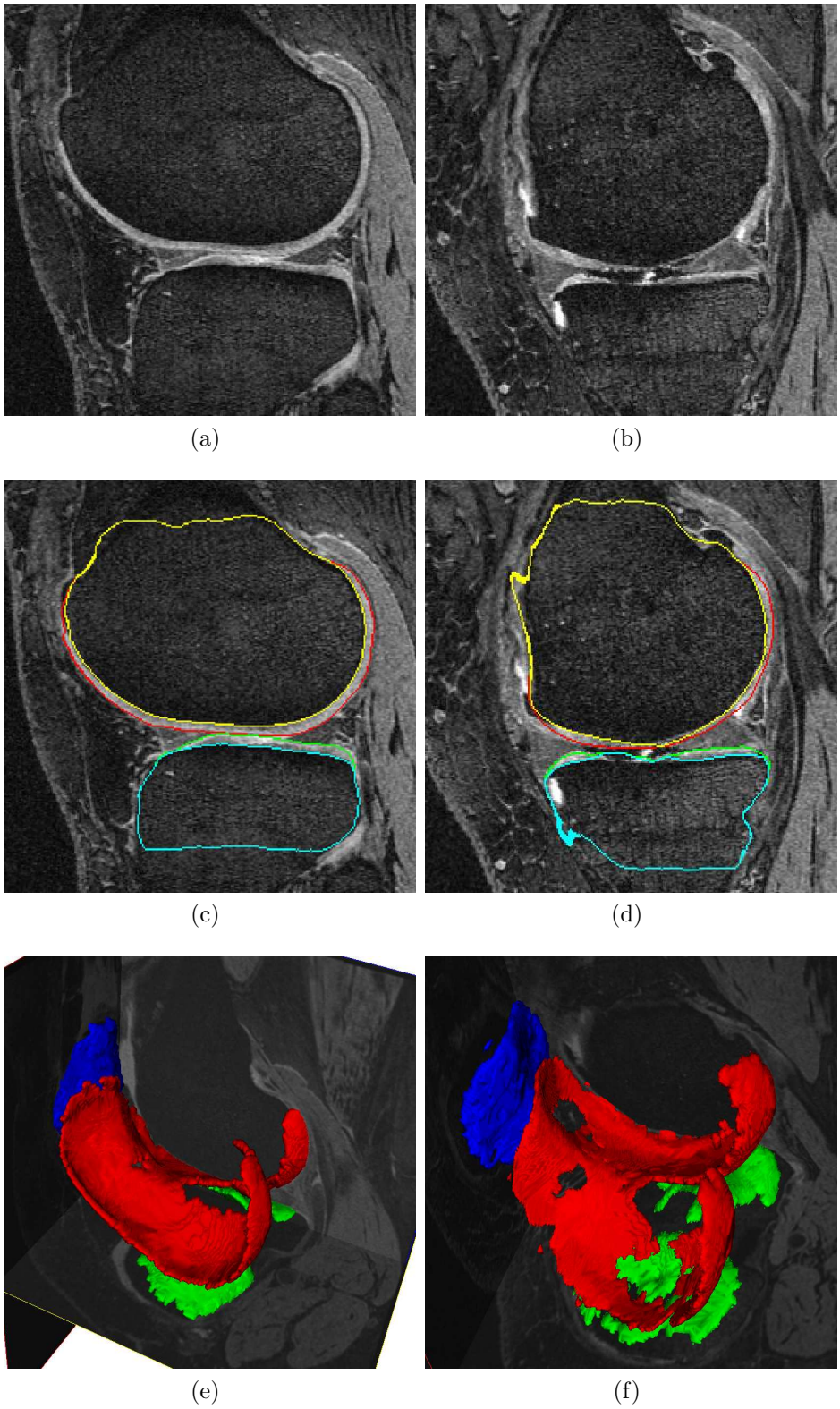

Figure 8.11: 3D segmentation of knee cartilages. Images from a knee minimally affected by osteoarthritis shown on the left. Severe cartilage degeneration shown on the right. (a,b) Original images. (c,d) The same slice with bone/cartilage segmentation. (e,f) Cartilage segmentation shown in 3D, note the cartilage thinning and "holes" in panel (f).

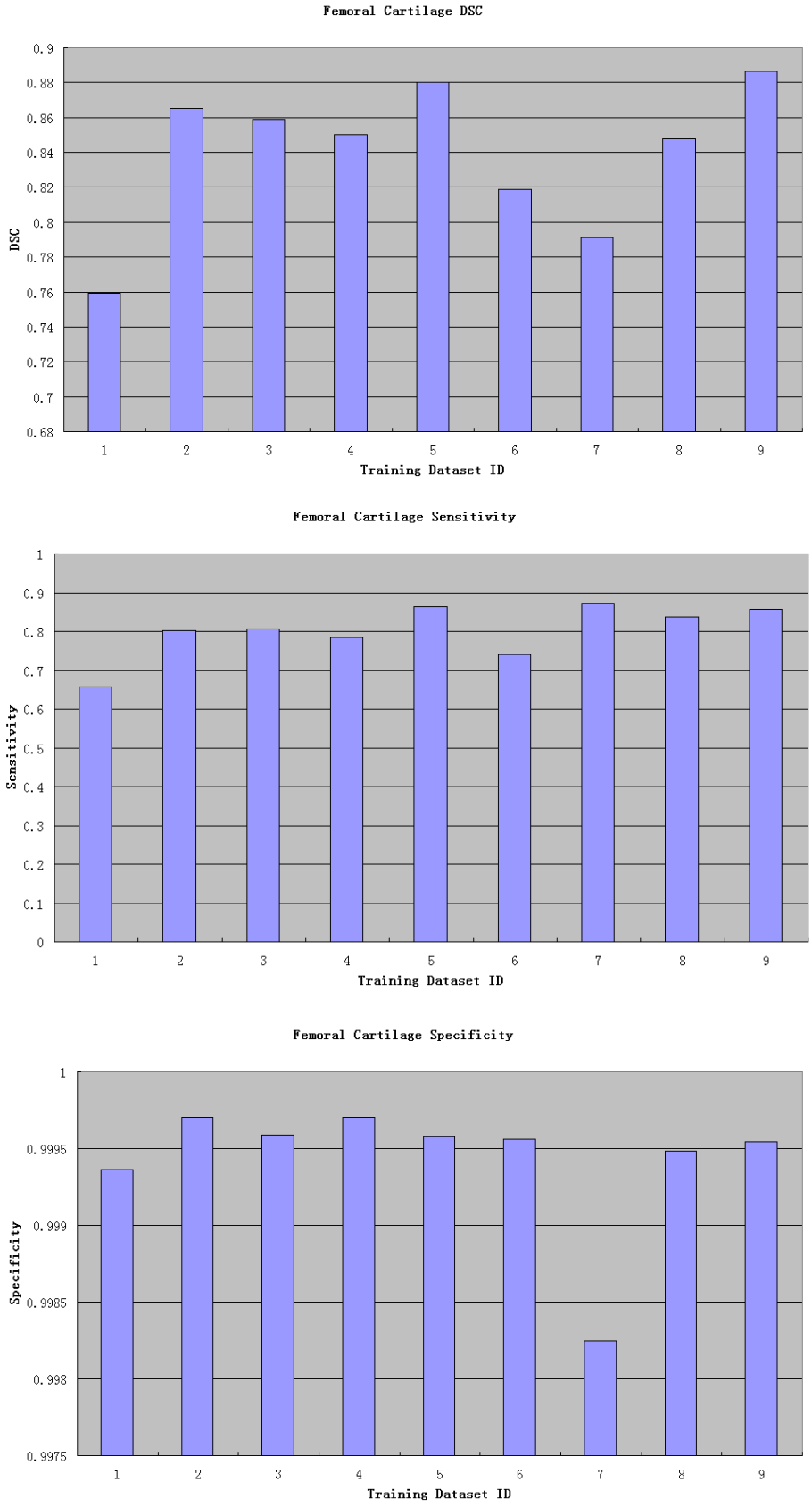

Figure 8.12: Charts for individual femoral cartilage volume measurements

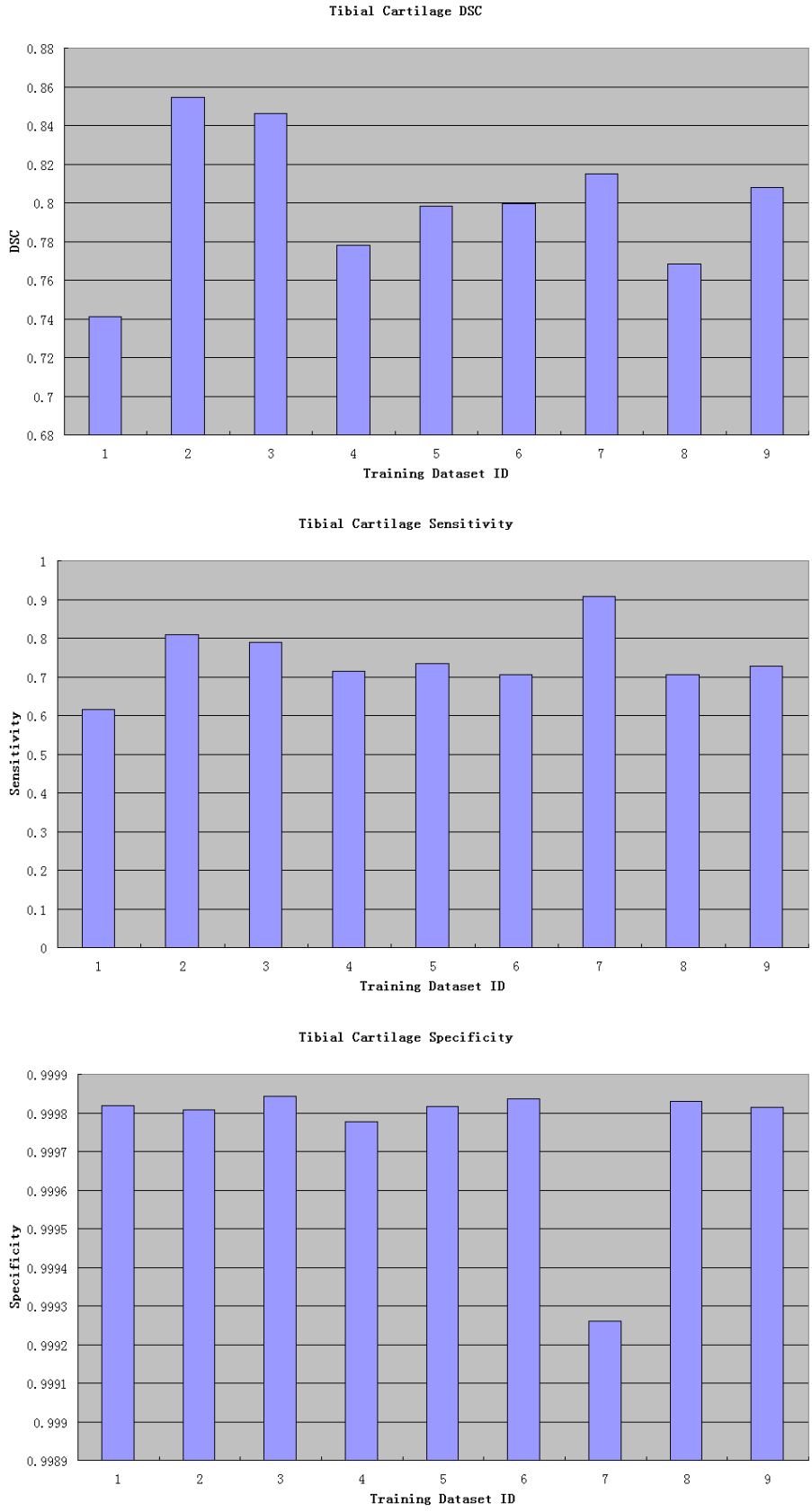

Figure 8.13: Charts for individual tibial cartilage volume measurements

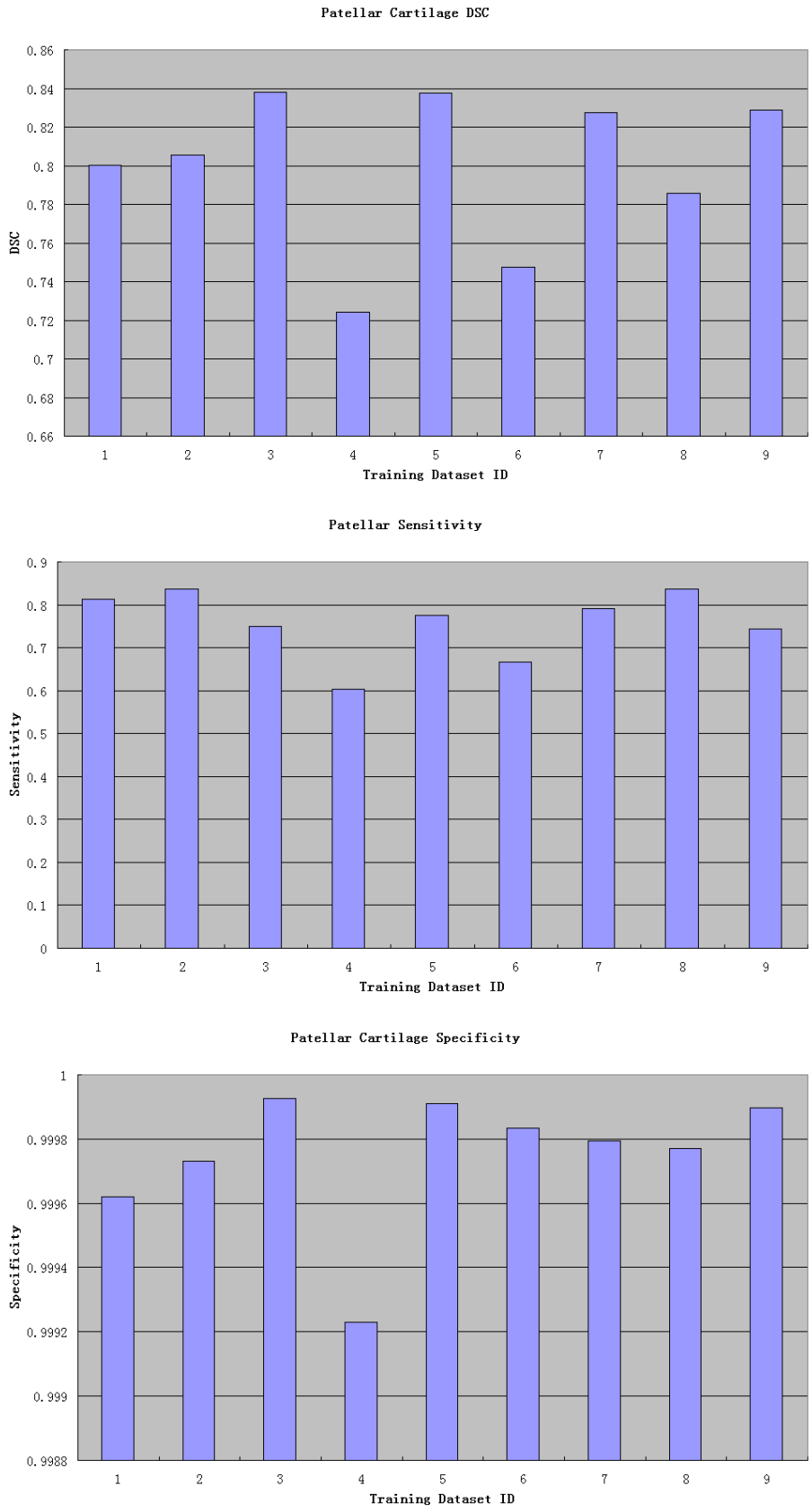

Figure 8.14: Charts for individual patellar cartilage volume measurements

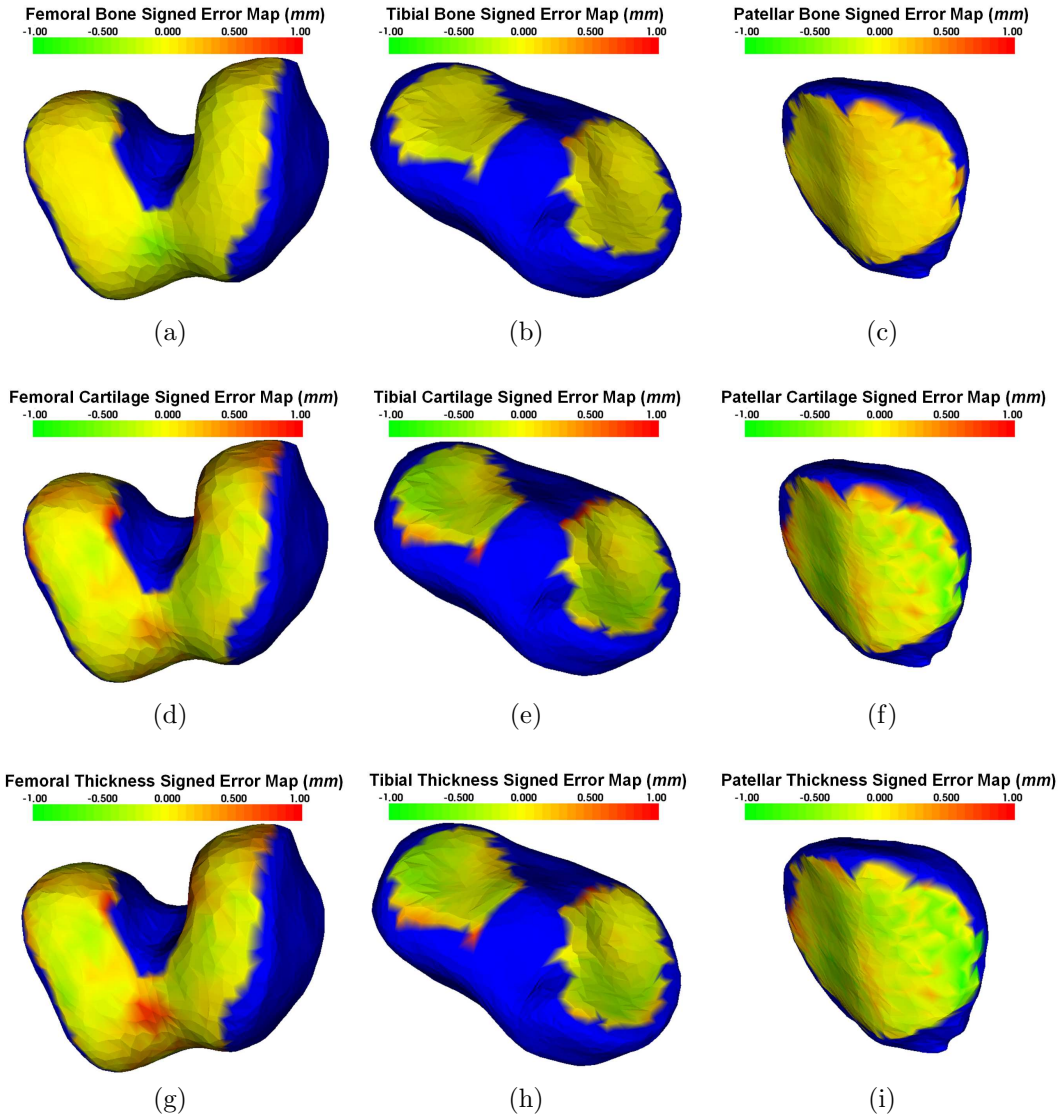

Figure 8.15: Distribution of mean signed surface positioning errors superimposed on mean shapes of the three bones forming the knee joint. In all panels, blue color corresponds to bone areas not covered by cartilage when mapped to mean shape. The range of colors from green to red corresponds to surface positioning errors ranging from -1 to +1 mm. Panels (a)–(c) show bone surface positioning errors, (d)–(f) show cartilage surface positioning errors, and (g)–(i) mean signed errors of computed cartilage thickness. Note that the yellowish color corresponds with zero error, visually demonstrating only a very small systematic segmentation and thickness assessment bias across all cartilage regions.

the presented method; its limitations; and causes and locations of errors in the knee cartilage segmentation.

8.4.1 Method properties, novelty and generality

To the best of our knowledge, this is the first paper in the archival literature to report the simultaneous segmentation of multiple objects with multiple surfaces per object. In the present application, the framework was applied to segment knee joint cartilage via simultaneous segmentation of the bone and cartilage surfaces of the femur, tibia, and patella. We have previously reported a general outline of this approach which required interactive initialization, used simplified cost functions, and lacked any validation [103]. The method is based on a layered-graph optimal image segmentation [62] that was extended to handle multiple interacting objects. This is a non-trivial extension that facilitates utilization of the optimal layered graph approach for segmentation of multiple objects for which the interaction properties may be based on surface proximity (as in the present application) as well as on any other general mutual relationships (e.g., relative distances of object centroids, orientation of the interacting objects in space, relative orientation of the interacting surfaces, etc.). The method can be directly extended to n-D, and the inter-object relationships can include higher-dimensional interactions, e.g., mutual object motion, interactive shape changes over time, and similar. Overall, the presented framework is very general and represents a new level of complexity that can be addressed using the layered surface graph optimization paradigm.

8.4.2 Limitations of the reported approach

While very general, our framework is not free of limitations. First, optimal layered surface graph segmentation approaches require availability of a meaningful preliminary segmentation (or localization) of the objects of interest prior to the optimal segmentation (or accurate delineation) step. Clearly, the quality of pre-segmentation

can affect the ability of the final graph-search segmentation to identify the desired borders. For example, if the pre-segmentation surfaces are too distant from the desired surfaces, their shape is inappropriate, or if the pre-segmentation fails for a variety of other reasons, the final graph may not contain the desired solution. In the multiple interacting object case, the pre-segmentation must be reasonable for all mutually interacting objects since it affects the cross-object context incorporated in the framework. Note however, that the reasonability requirement may allow substantial inaccuracy. For example, if segmenting 3D objects, all that may be required as a pre-segmentation result may be a topologically correct surface that is positioned within a range of possible distances from this pre-segmentation surface to the desired surface. As long as the desired surface occurs within the overall graph constructed from the pre-segmentation surfaces, the final simultaneous segmentation step may still yield the correct final segmentation – although with a dependency on the quality of the employed cost functions, surface smoothness constraints, possible shape priors, etc. In our knee joint segmentation application, the Adaboost localization followed by an iterative graph search approach for pre-segmentation of the individual bone surfaces was sufficiently robust and performed without any need for interaction or editing.

While ably solving the column-crossing problem, the ELF calculation utilized is computationally demanding for surfaces with high vertex density [99]. In our experiment, computing 40 points along each ELF for 2000 vertices consumed 13 seconds on our PC, which is comparable to computing Danielsson distance transform [14] for a $200 \times 200 \times 200$ volume. However, ELF computation time increases exponentially with the increase in the numbers of vertices. One possible way to address this potential limitation would be to merge multiple distant vertex charges to one "larger" vertex charge when computing local ELF, thereby greatly decreasing the total amount of vertices involved in the computation.

8.4.3 Cartilage segmentation errors

Complete 3D cartilage segmentation is a difficult problem. Our current method, while performing very well overall, exhibited local surface positioning inaccuracies as reflected in the reported unsigned surface positioning errors (Fig. 8.15). The difficult character of the cartilage MR segmentation task can be appreciated when assessing the inter-observer variability of bone and cartilage surface definition by human experts – manual tracings suffered from inter-observer variability of $0.5 \pm 0.5mm$ assessed on a set of 16 MR 3D datasets, with 10 slices manually traced per dataset by each of four expert observers. The inter-observer variability of cartilage thickness was $1.0 \pm 0.8mm$. Clearly, the performance of the presented segmentation system compares well with the inter-observer variability and is generally the same for all three bone and cartilage surfaces.

When considering the segmentation inaccuracy with respect to its location and underlying cause, a clear pattern can be observed, with errors mostly contained within the non-cartilage regions and therefore of less functional importance. Short of implementing better MR imaging sequences, interactive user guidance may be incorporated resulting in semi-automated multi-object multi-surface layered surface graph segmentation.

When assessing segmentation performance, it may be difficult to compare DSC-based segmentation performance directly with published results of others, since each study uses different images, training data sizes, and disease conditions. Note that the OA images are substantially more difficult to segment than images of healthy joints utilized in most published cartilage segmentation studies. The presented method obtains the segmentation relatively quickly and is much faster compared to the two previously reported methods of Dam and Fripp [13, 32]. Our approach required 20 minutes, compared with one to several hours of the earlier approaches on a comparable hardware when images of the same size are considered. Importantly, our novel

approach offers comparable if not better performance than the earlier approaches. For example, Folkesson achieved DSC values of 0.78 and 0.81 for the femoral and tibial cartilage based on 51 healthy and 63 OA low-field MR images [24]. Fripp reported DSC values of 0.85, 0.83 and 0.83 for the femoral, tibial and patellar cartilages from 20 healthy SPGR MR images [32].

The embedding of pattern recognition techniques within an optimal surface detection framework is the key new contribution of the presented methods. Notably, the presented approach has only one sensitive parameter to be determined – the surface smoothness constraint, and the selection of this parameter is very intuitive. Too-small constraint values will make the algorithm insensitive to sharp discontinuities of bone and cartilage surfaces while too-large values will contribute to surface noise, roughness, and loss of the a priori shape information. In the work reported here, a smoothness constraint of 3 voxels was utilized, based on empirical determination. Although trained only on a small training set, the algorithm segmented complicated knee bone and cartilage structures well. As more training data becomes available in the future, we believe that the performance of the system can be expected to further improve.

CHAPTER 9
MENISCUS SEGMENTATION: A PATTERN RECOGNITION APPROACH

The menisci of the knee has crescent shape which support and protect every healthy knee by minimizing contact stress within the tibiofemoral joint. Fig. 1.3 shows anatomic structure of meniscus. In OAI sagittal DESS MR WE images, it usually appears as dark regions between adjacent bright femoral and tibial cartilage (see Fig. 2.2.)

Many studies showed the association of meniscal pathology changes with cartilage loss in symptomatic knee osteoarthritis [1, 2, 16, 47], which has raised questions about meniscus segmentation. After comparison between specimen's meniscal volume measured in 3T MR images with those measured by water displacement, Bowers *et al.* indicated that 3D MR image is reliable for meniscal volume measurement [3].

Some fully- or semi-automated meniscal region segmentation approaches were reported. Out of them, some approaches were served as the first step to detect meniscal tears. For example, Köse *et al.* used a histogram-based method with edge detection filtering and statistical segmentation-based methods to locate the menisci at the knee joint in 2D MR images. After that, the menisci were extracted by a template matching technique [56]. Hata *et al.* registered T1-weighted and T2-weighted images manually, then determined meniscal region by fuzzy if-then rules in three 3D MR datasets [44]. Ramakrishna *et al.* extracted meniscal region by a 3-step process: cropping, thresholding and application of morphology constraints [78]. When evaluated for the 2D sagittal T1-weighted MR imaging sequences of the knee in 28 patients with diagnoses of meniscal tears, their automated meniscal tears CAD (Computer Aided Diagnosis) system showed promising result. However, the above works, in somehow, treated menisci segmentation as a pre-segmentation step for meniscal tear detection. A quite accurate estimation of meniscal region is usually not required; thus no detailed meniscal volume measurement was provided.

There were several works concentrating on meniscal volume assessment. Tamez-Pena *et al.* segmented femur, tibia and menisci using a region growing algorithm followed by region splitting and region merging rules [89]. Swanson *et al.* developed a semi-automated meniscal segmentation approach. In their approach, a Gaussian model was fitted according to manually selected meniscal seeds. Then the meniscal segmentation was performed using thresholding approach based on the Gaussian model. The segmentation results were further processed by conditional dilation and post-processing operations to increase accuracy [87]. The total segmentation time including user interaction is 2 to 4 mins for each of 3D volumes. Fripp *et al.* first found meniscus VOI from femoral and tibial cartilage surface segmentation results. Then, they estimated intensity distributions of meniscus and ligaments-synovial to form a Gaussian Mixture Model (GMM). After that, lateral and medial meniscal shape models were fitted to the image and the model-based segmentation process were implemented iteratively based on the estimated GMM. Their method got good DSC using 14 fat suppressed SPGR MR images [30].

9.1 Meniscus Segmentation Method

Although using shape models can easily incorporate shape information, the narrow sheet character of menisci may be sensitive to positioning errors from automated model localization. This would decrease robustness of the system. Furthermore, GMM seems not sufficient to capture all the texture and position information for menisci segmentation. In favor of our cartilage segmentation work, we decided to use pattern recognition technique to find meniscal region in a local and narrow rectangular meniscus VOI. The detailed processes are as follows:

9.1.1 VOI detection

We only detect possible meniscal region within 14 mm away from both segmented femoral and tibial cartilages. The candidate locations were restricted in a narrow

bounding box VOI as shown in Fig. 9.1.

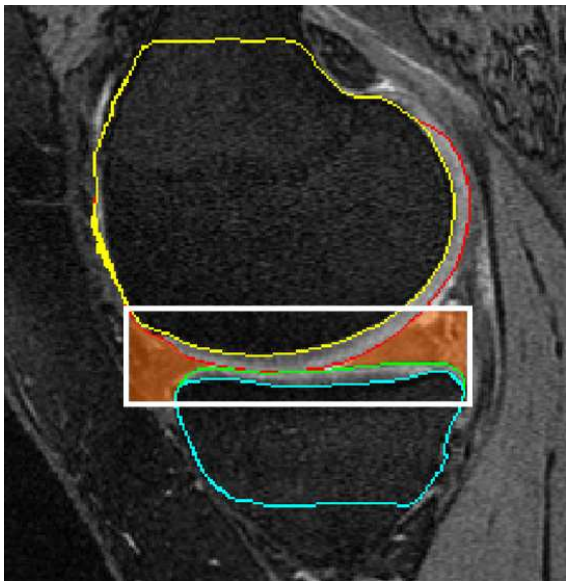

Figure 9.1: Volumetric region (in orange) of possible meniscal occurrence

9.1.2 Feature collection

The feature set included intensities and gradients from images smoothed by different Gaussian filters as local texture features. Principal components and blob-, line- and plate-like features were also included as local shape features. Finally, local physical positions, distance to the reference femoral and tibial cartilage surfaces were added global shape features were added as global shape features. These features have been illustrated in Chapter 7.

9.1.3 Classifier training

Again, Random Forest classifier described in Chapter 7 is also suitable for meniscus segmentation task. Instead of output probability, the trained classifier directly outputs classification result.

9.2 Experimental Method & Results

The meniscus volumns for all the nine images in TRAIN-2 set (Section 8.2.2) were manually labeled. We collected training samples from these images. In leave-one-out test, these manually labeled volumns are also independent standard. Furthermore, in the TEST set, meniscal boundaries for all the 60 images were traced by three observers. The detailed description of the datasets with independent standard can be found in Section 8.2.2. We used the same methods as described in Section 8.2.4 to assess DSC from TRAIN-2 set and signed and unsigned surface positioning errors from TEST set.

A typical meniscus segmentation result is shown in Fig. 9.2. Tab. 9.1 shows leave-one-out measurement from TRAIN-2 (Section 8.2.2). The detailed assessment for each dataset is shown in Fig. 9.3. Tab. 9.2 shows signed and unsigned surface positioning errors from TEST (Section 8.2.2) with details in Fig. 9.4.

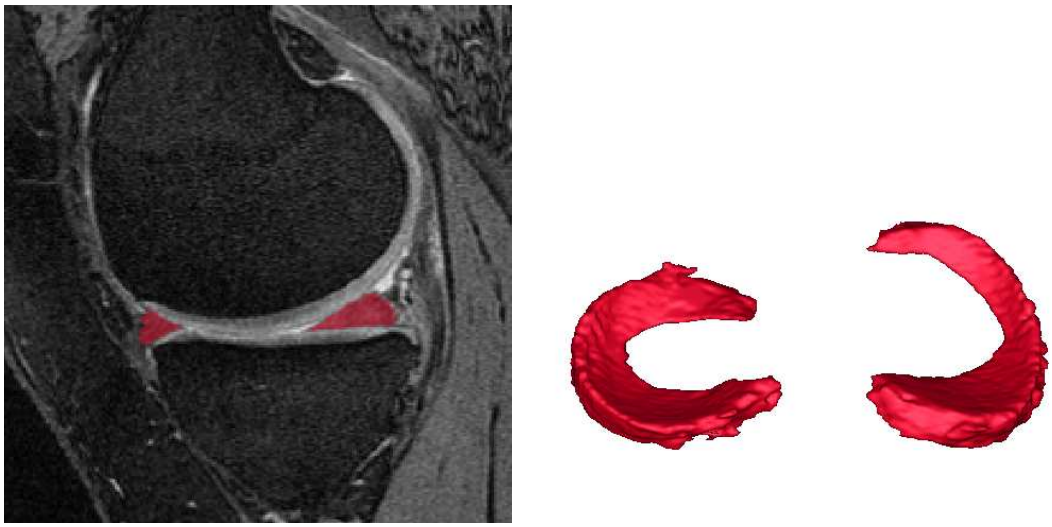

(a) (b)

Figure 9.2: 3D meniscus segmentation result. (a) Sample slice from a 3D segmentation result. (b) The segmentation result shown in 3D.

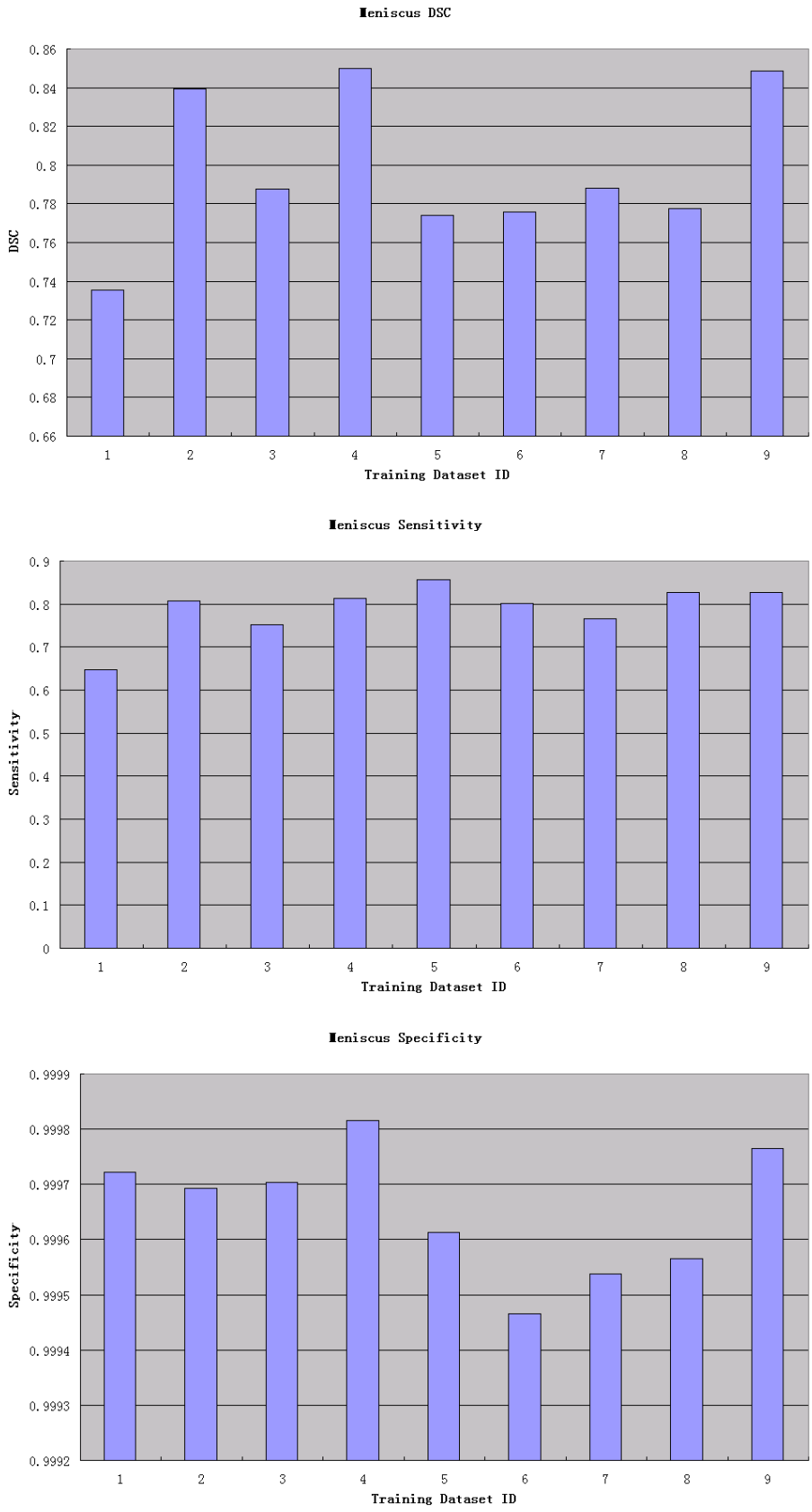

Figure 9.3: Charts for individual meniscus volume measurements

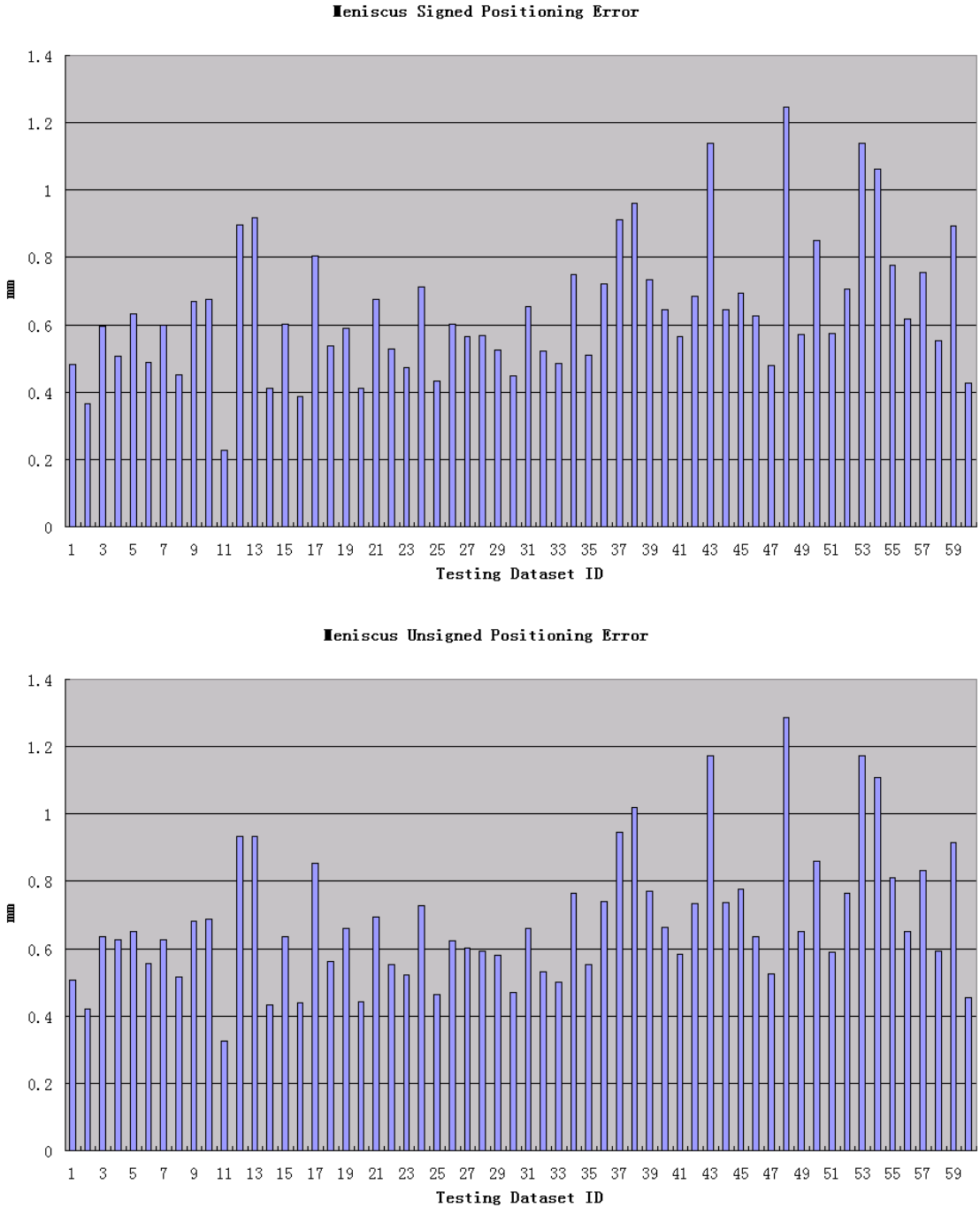

Figure 9.4: Charts for individual meniscus surface positioning error measurements

Table 9.1: Volume measurement in comparison with the independent standard.

	DSC	Sensitivity	Specificity
Meniscus	0.80 ± 0.04	0.79 ± 0.06	1.00 ± 0.00

Table 9.2: Mean signed and unsigned error of computer segmentation in comparison with the independent standard in mm.

ERRORS (mm)	Signed Positioning	Unsigned Positioning
Meniscus	0.65 ± 0.20	0.68 ± 0.20

9.3 Chapter Summary

Based on the fully automated cartilage segmentation results, we designed a pattern recognition technique based automated segmentation system for meniscus segmentation. In this work, we narrowed menisci searching range into a narrow bounding box VOI. Within the VOI, we selected a set of useful features and used them to train a Random Forest classifier. The output of this meniscus segmentation system was provided directly from the classifier.

The average time to segment one 3D meniscus volume in a 3D sagittal DESS MR image is about 1.5 mins. When tested in the TRAIN-2 set (which contains four images from incident cohort, and five images from progressive cohort in OAI) by leave-one-out strategy, our system outperformed other previously reported segmentation systems in DSC. For example, Tamez-Pena's approach got overlaps 53.73% and 59.1% for lateral and medial menisci respectively [89]. Swanson's semi-automated segmentation system resulted DSC 0.8 for 10 normal participants and 0.64 to 0.75 for 14 participants with established knee OA [87]. The images in his experiment were also from OAI.

Fripp's shape model based automated segmentation system reported DSC 0.75 and 0.77 for medial and lateral menisci respectively based on 14 healthy knee SPGR MR images [30].

The meniscus segmentation performance is highly related to the accuracy of cartilage segmentation result. Under-segmented cartilage surfaces may cause the meniscus classifier classify part of cartilage as menisci thus increasing false positive rate and over-segmented cartilage may reduce the possible meniscal occurrence region thus increasing false negative rate. An example of such error is shown in Section 10.2.

CHAPTER 10
CONCLUSION, ERROR ANALYSIS AND FUTURE WORK

10.1 Conclusion

The proposed aims of our research in Chapter 3 were fulfilled.

For aim 1: We reported a general multi-object multi-surface segmentation approach for optimally segmenting multiple surfaces that mutually interact within individual objects or between objects. The problem is modeled by a complex multi-layered graph in which solution-related costs are associated with individual graph nodes. Intra-surface, inter-surface, and inter-object relationships are represented by context-specific graph arcs. This method is called LOGISMOS–Layered Optimal Graph Image Segmentation of Multiple Objects and Surfaces and it includes four steps: (1) Object pre-segmentation (2) Construction of object-specific graphs (3) Incorporation of multi-object interactions and (4) Assignment of cost function and optimization of the graph.

For aim 2: Following the general outline of our LOGISMOS approach, a method for simultaneous segmentation of cartilages in the femur, tibia, and patella bones forming the knee joint is reported. Specifically, we extended Viola and Jones well-known face recognition work to 3D to detect VOI for each bone. Then single surface detection graphs were built and implemented iteratively yielding bone pre-segmentation surfaces. Based on the surfaces, we built multi-surface sub-graphs by incorporating bone-cartilage correlation relationship. The multi-object interaction information between adjacent surfaces were provided by constraint-point surface mapping technique. The information was incorporated into a global graph by connecting individual sub-graphs. The graph costs were designed by inverted probabilities provided by classifiers trained from a training dataset, and the graph optimization process segmented all six surfaces (femoral bone, femoral cartilage, tibial bone, tibial cartilage, patellar bone and patellar cartilage) simultaneously and global optimally. The experiment

and results showed that this fully-automated cartilage system was fast, robust and accurate.

For aim 3: Based on the cartilage segmentation, a pattern recognition based meniscus segmentation system was designed. The validation results also proved good performances of this system.

For aim 4: We assessed our bone-cartilage as well as meniscus segmentation systems by DSC and surface positioning errors from nine and 60 MR images from OAI dataset respectively. The reported measurement demonstrated very good performance of these two systems.

As a non-trivial extension of the previously reported method for optimal segmentation of multiple interacting surfaces [62], the following specific contributions were made beside the ones illustrated above.

Inter-object graph arcs were introduced for the first time to incorporate mutual interacting relationship between multiple objects by constraining the distances between them.

In order to avoid graph column intersection problem and find corresponding graph column pairs in the interacting regions between mutually interacted objects, we introduced a new search direction definition along ELF directions. The proposed search direction has non-intersection property and it can generate a robust one-to-one and all-to-all vertex pair mapping at interacting regions between objects when applied into a constraint-point cross-object surface mapping technique.

Due to the flexibility of cost design, pattern recognition technique was directly embedded into a graph-search based optimal surface detection framework to perform globally optimal surface and region detection under a priori shape constrain. A set of problem-specific features were collected for bone surface segmentation, cartilage region delineation and meniscus volume detection.

Comparing the cartilage segmentation performance presented in our SPIE pa-

per [101] and also showed in my proposal one year ago, we achieved similar mean errors but greatly decreased standard deviation (from 0.6 to 0.2 mm). Note that the independent standard used in SPIE and proposal only covered central cartilage regions which as shown in Fig. 8.15 has much smaller errors compared with an overall cartilage region measurement. Furthermore, the previous approach is semi-automated which requires users to select VOIs, while the approach presented here is fully automated. We also substantially increased the independent standard from 160 slices to about 4000 slices and adopted more robust pattern recognition technique based graph cost compared with simple Gaussian model based cost. Considering all of the above, we believe the approach presented here is more automated, robust and accurate than the one invented one year before.

10.2 Analysis of Segmentation Error

As stated before, our segmentation systems are not free of limitations. Here we will show some segmentation errors in slices. The MR images used here were picked from TEST dataset (Section 8.2.2) according to the individual error measurement results (Fig. 8.4, 8.5, 8.6, 8.7, 8.8, 8.9 and 9.4).

Slices in Fig. 10.1 are from image No.43 in TEST dataset. From Fig. 8.5 and 8.7 we can see the segmentation errors for this MR image for femoral and tibial cartilage surfaces are relatively larger than most others. This is because the patient has much thicker cartilage at some locations (as the femoral cartilage in Fig. 10.1a and tibial cartilage in Fig. 10.1b). These thickness variations were not captured by cartilage classifiers from the TRAIN-2 (Section 8.2.2) dataset. Including more MR images with different cartilage thickness in training dataset can help to overcome this problem. Furthermore, we may notice that the image quality can also affect the segmentation performance as the dark region in femoral cartilage in Fig. 10.1a resulted under-segmentation in Fig. 10.1c.

Slices in Fig. 10.2 are from image No.44 in TEST dataset. We see that the Ad-

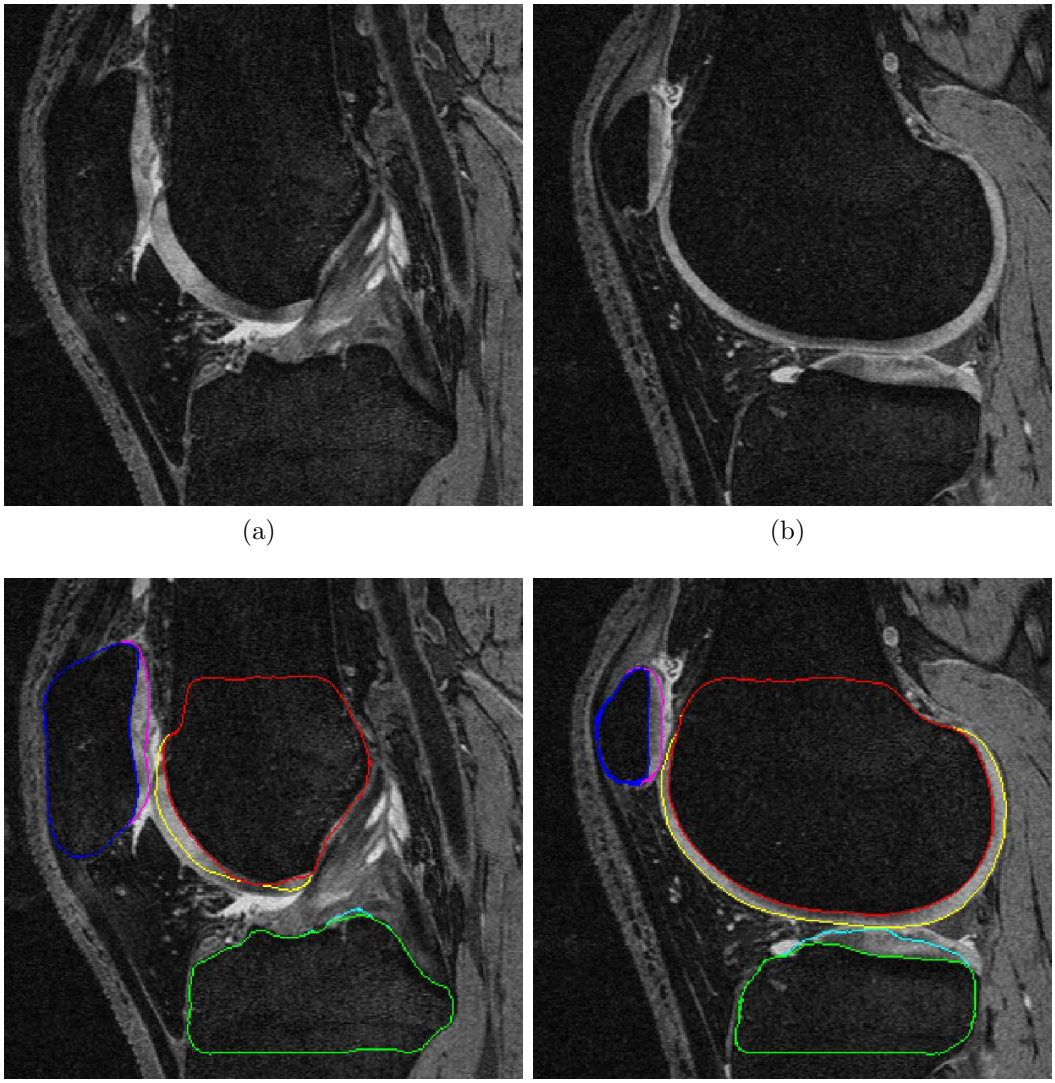

(a) (b)

(c) (d)

Figure 10.1: Segmentatation error generated from No.43 in TEST dataset. (a,b) Original images. (c,d) The same slice with bone/cartilage segmentation.

aboost cartilage/non-cartilage region classifers may generate some errors which caused over-segmentation of some synovial fluid and under-segmentation of the cartilage in the other side as in Fig. 10.2c. Some prior knowledge of the cartilage location may be helpful for solving this problem. Fig. 10.2d shows the inaccuracies of the tibial pre-segmented bone surface led to part of the tibial cartilage not segmented.

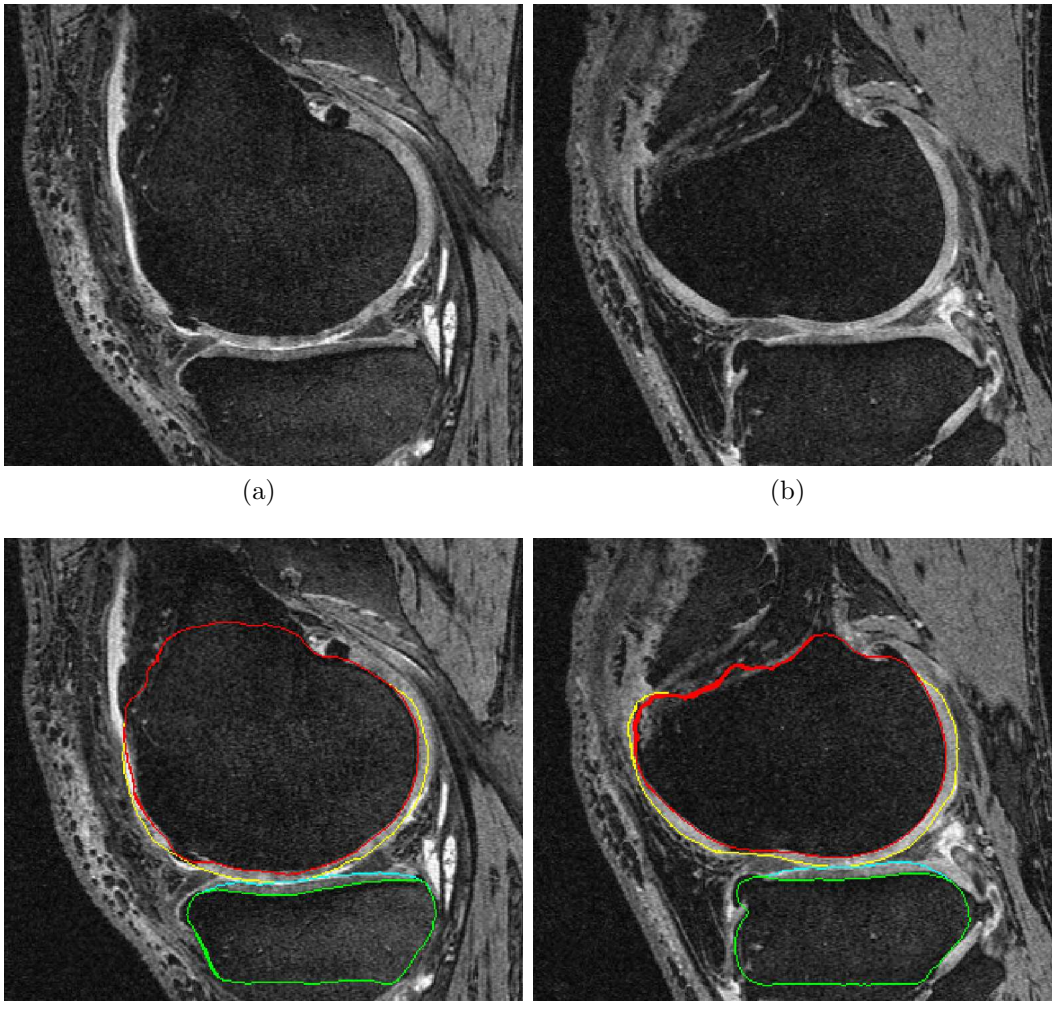

(a) (b)

(c) (d)

Figure 10.2: Segmentatation error generated from No.44 in TEST dataset. (a,b) Original images. (c,d) The same slice with bone/cartilage segmentation.

The major error for meniscus segmentation is from lateral boundary slices as shown in Fig. 10.3. The image is from the MR volume No. 48 in TEST dataset which has the largest surface positioning error. The causes of under-segmentation of menisci as shown in Fig. 10.3c is partly from the inaccurate cartilage segmentation as in Fig. 10.3b and varied intensity distributions of menisci in MR images.

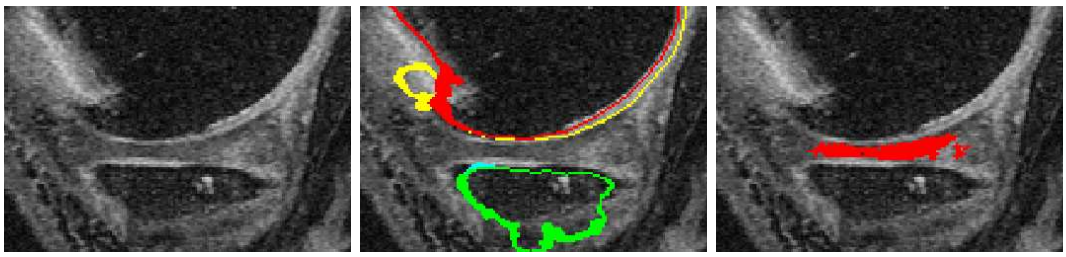

(a) (b) (c)

Figure 10.3: Segmentatation error generated from No.48 in TEST dataset. (a) Original images. (b) Cartilage segmentation result at lateral part with some error. (c) Meniscus segmentation result.

Regarding to some of the errors shown in this section, we will propose solutions to reduce them in the next section.

10.3 Future Work

Although overall quite successful, the system design and validation methods may still have some room for meaningful improvement.

For example, a weak classifier cascade strategy [90] in AdaBoost can efficiently reject a vast number of background samples using a small number of weak classifiers. That will increase the speed of our system in bone VOI location and cartilage/non-cartilage region detection steps.

We believe more training datasets can substantially further increase the segmentation performance. A validation result based on more independent standard released

by OAI would be more convincing. Moreover, providing measurement on different pre-defined cartilage regions [19] would provide useful information for radiologists. The region definition process can be automated [88]. Dividing test samples according to different OA symptoms are also desired. OAI dataset provides such evaluation into Incidence and Progression cohorts. More detailed analysis may be helpful (e.g. WORMS scoring [72], joint space narrowing [47], K-L grade [51]). Furthermore, building a segmentation system which can perform reliable progressive study (baseline v.s. n-year follow up) of OA in OAI might provide another interesting research tool for orthopedists [21, 46, 94].

Pattern recognition based meniscus segmentation may generate "small islands" false positives. If needed, a post-processing step will be helpful to remove these "islands". The post-processing may be as simple as a binary morphology operation (e.g. opening). A more reliable approach is by building *Markov Random Field* [52] or *Conditional Random Field* [58] based on the probability of each voxel provided by the Random Forest classifier and finding the global minimum energy solution using a *graph cut* segmentation approach [5, 54].

For large previously unseen dataset segmentation, the major errors of the cartilage segmentation system usually come from the inaccurate locating of VOIs, inaccurate detecting of bone pre-segmentation and inaccurate final bone-cartilage segmentation. The inaccurate VOI locating usually incurs low matching probabilities from AdaBoost VOI detection classifiers. An early warning procedure can be build regarding to the low matching probabilities, so that the user can manually correct the VOIs before the segmentation process. For the local errors produced in pre-segmentation or final segmentation, the local properties on the surface can be compared with the local properties around the surface. If cartilage properties are not presented on the surface but a distance away from the surface, the system can provide a local warning on the surface (e.g. mark the result surface into different colors). Currently there is no mesh

editting function in the system, but it is important to let user modify local errors after inspection.

REFERENCES

[1] L. D. Bennett and J. C. Buckland-Wright, "Meniscal and articular cartilage changes in knee osteoarthritis: a cross-sectional double-contrast macroradiographic study," *Rheumatology*, vol. 41, no. 8, pp. 917–923, 2002.

[2] M. Berthiaume, J. Raynauld, J. Martel-Pelletier, and et al, "Meniscal tear and extrusion are strongly associated with progression of symptomatic knee osteoarthritis as assessed by quantitative magnetic resonance imaging," *Annals of the Rheumatic Diseases*, vol. 64, no. 4, pp. 556–563, 2005.

[3] M. E. Bowers, G. A. Tung, B. C. Fleming, J. J. Crisco, and J. Rey, "Quantification of meniscal volume by segmentation of 3T magnetic resonance images," *Journal of Biomechanics*, vol. 40, pp. 2811–2815, 2007.

[4] Y. Boykov and V. Kolmogorov, "An experimental comparison of min-cut/max-flow algorithms for energy minimization in vision," *IEEE Trans. Pattern Anal. and Machine Intelligence*, vol. 26, pp. 1124–1137, 2004.

[5] Y. Boykov, O. Veksler, and R. Zabih, "Fast approximate energy minimization via graph cuts," *IEEE Trans. Pattern Anal. and Machine Intelligence*, vol. 23, no. 11, pp. 1222–1239, 2001.

[6] L. Breiman, "Random forests," *Machine Learning*, vol. 45, no. 1, pp. 5–32, 2001.

[7] M. Bruijne and M. Nielsen, "Multi-object segmentation using shape particles," in *Information Processing in Medical Imaging*, ser. Lecture Notes in Computer Science, vol. 3565. Springer, July 2005, pp. 762–773.

[8] B. V. Cherkassky and A. V. Goldberg, "On implementing push-relabel method for the maximum flow problem," *Algorithmica*, vol. 19, pp. 390–410, 1997.

[9] T. F. Cootes, G. J. Edwards, and C. J. Taylor, "Ieee trans. pattern anal. and machine intelligence," *Active Appearance Models*, vol. 23, no. 6, pp. 681–685, 2001.

[10] T. F. Cootes, C. J. Taylor, D. H. Cooper, and J. Graham, "Active shape models – their training and application," *Computer Vision and Image Understanding*, vol. 61, pp. 38–59, 1995.

[11] T. H. Cormen, C. E. Leiserson, R. L. Rivest, and C. Stein, *Introduction to Algorithms (2nd ed.)*. MIT Press, 2001.

[12] T. M. Cover and P. E. Hart, "Nearest neighbor pattern classification," *IEEE Trans. Information Theory*, vol. 13, no. 1, pp. 21–27, 1967.

[13] E. B. Dam and M. Loog, "Efficient segmentation by sparse pixel classification," *IEEE Trans. Med. Imaging*, vol. 27, no. 10, pp. 1525–1534, 2008.

[14] P. E. Danielsson, "Euclidean distance mapping,," *Computer Graphics and Image Processing*, vol. 14, pp. 227–248, 1980.

[15] L. R. Dice, "Measures of the amount of ecologic association between species," *Ecology*, vol. 26, pp. 297–302, 1945.

[16] C. Ding, J. Martel-Pelletier, J. P. Pelletier, and et al, "Knee meniscal extrusion in a largely non-osteoarthritic cohort: association with greater loss of cartilage volume," *Arthritis Res Ther*, vol. 9, no. 2, p. R21, 2007.

[17] P. Domingos and M. Pazzani, "On the optimality of the simple bayesian classifier under zero-one loss," *Machine Learning*, vol. 29, pp. 103–137, 1997.

[18] H. Drucker, C. J. C. Burges, L. Kaufman, A. Smola, and V. Vapnik, "Support vector regression machines," in *Advances in Neural Information Processing Systems (NIPS)*, 1997, pp. 155–161.

[19] F. Eckstein, G. Ateshian, R. Burgkart, D. Burstein, F. Cicuttini, B. Dardzinski, M. Gray, T. M. Link, S. Majumdar, T. Mosher, C. Peterfy, S. Totterman, J. Waterton, and C. S. Winalski, "Proposal for a nomenclature for magnetic resonance imaging based measures of articular cartilage in osteoarthritis," in *Osteoarthritis and Cartilage*, vol. 14, 2006, pp. 974–983.

[20] F. Eckstein, F. Cicuttini, J. P. Raynauld, J. C. Waterton, and C. Peterfy, "Magnetic resonance imaging (MRI) of articular cartilage in knee osteoarthritis (OA): Morphological assessment," *Osteoarthritis and Cartilage*, vol. 14, pp. A46–A75, 2006.

[21] F. Eckstein, S. Maschek, W. Wirth, M. Hudelmaier, W. Hitzl, B. Wyman, M.-P. Nevitt, and M. H. L. Graverand, "One year change of knee cartilage morphology in the first release of participants from the osteoarthritis initiative progression subcohort – association with sex, body mass index, symptoms, and radiographic oa status," *Ann Rheum Dis.*, vol. 7, 2008.

[22] J. Fleureau, M. Garreau, D. Boulmier, and A. Hernández, "3D multi-object segmentation of cardiac MSCT imageing by using a multi-agent approach," in *IEEE Engineering in Medicine and Biology Society, 2007. EMBS 2007. 29th Annual International Conference of the IEEE*, August 2007, pp. 6003–6006.

[23] ——, "A new 3D multi-object segmentation method in cardiac MSCT imaging using a multi-agent approach," in *IFMBE Proceedings*, vol. 18. Springer, November 2007, pp. 249–253.

[24] J. Folkesson, E. B. Dam, O. F. Olsen, P. C. Petterson, and C. Christiansen, "Segmenting articular cartilage automatically using a voxel classification approach," *IEEE Trans. Med. Imaging*, vol. 26, no. 1, pp. 106–115, 2007.

[25] L. Ford and D. Fulkerson, *Flows in Networks*. Princeton University Press, 1962.

[26] A. F. Frangi, W. J. Niessen, K. L. Vincken, and M. A. Viergever, "Multiscale vessel enhancement filtering," in *International Conference on Medical Image Computing and Computer Assisted Intervention (MICCAI)*, 1998, pp. 130–137.

[27] D. Freedman, R. J. Radke, T. Zhang, Y. Jeong, and G. Chen, "Model-based multi-object segmentation via distribution matching," *Computer Vision and Pattern Recognition Workshop (CVPRW)*, vol. 1, p. 11, 2004.

[28] D. Freedman, R. Radke, T. Zhang, Y. Jeong, D. M. Lovelock, and G. Chen, "Model-based segmentation of medical imagery by matching distributions," *IEEE Trans. Med. Imaging*, vol. 24, pp. 281–292, March 2005.

[29] Y. Freund and R. E. Schapire, "A decision-theoretic generalization of on-line learning and an application to boosting," *Journal of Computer and System Sciences*, vol. 55, no. 1, pp. 119–139, 1997.

[30] J. Fripp, P. Bourgeat, C. Engstrom, S. Ourselin, S. Crozier, and O. Salvado, "Automated segmentation of the menisci from MR images," in *Proceedings of the Sixth IEEE international conference on Symposium on Biomedical Imaging: From Nano to Macro*, 2009, pp. 510–513.

[31] J. Fripp, S. Crozier, S. K. Warfield, and S. Ourselin, "Automatic segmentation of articular cartilage in magnetic resonance images of the knee," in *International Conference on Medical Image Computing and Computer Assisted Intervention (MICCAI)*, ser. Lecture Notes in Computer Science, vol. 4792, 2007, pp. 186–194.

[32] ——, "Automatic segmentation of and quantitative analysis of the articular cartilage in magnetic resonance images of the knee," *IEEE Trans. Med. Imaging*, vol. 29, no. 1, pp. 55–64, 2010.

[33] J. C. Gamio, J. S. Bauer, R. Stahl, K. Y. Lee, S. Krause, T. M. Link, and S. Majumdar, "Inter-subject comparison of MRI knee cartilage thickness," *Medical Image Analysis*, vol. 12, pp. 120–135, 2008.

[34] M. K. Garvin, M. D. Abramoff, R. Kardon, S. R. Russell, X. Wu, and M. Sonka, "Intraretinal layer segmentation of macular optical coherence tomography images using optimal 3-D graph search," *IEEE Trans. Med. Imaging*, vol. 27, no. 10, pp. 1495–1505, 2008.

[35] M. K. Garvin, M. D. Abramoff, X. Wu, S. R. Russell, T. L. Burns, and M. Sonka, "Automated 3-D intraretinal layer segmentation of macular spectral-domain optical coherence tomography images," *IEEE Trans. Med. Imaging*, vol. 28, no. 9, pp. 1436–1447, 2009.

[36] S. Ghosh, O. Beuf, M. Ries, N. E. Lane, L. S. Steinbach, T. M. Link, and S. Majumdar, "Watershed segmentation of high resolution. magnetic resonance images of articular cartilage of the knee," in *Proceedings of the 22nd Annual EMBS International Conference*, July 2000, pp. 23–28.

[37] A. V. Goldberg and R. E. Tarjan, "A new approach to the maximum-flow problem," *Journal of the Association for Computing Machinery*, vol. 35, no. 4, pp. 921–940, 1988.

[38] J. C. Gower and G. B. Dijksterhuis, *Procrustes Problems*. Oxford University Press, 2004.

[39] L. Grady, "Random walks for image segmentation," *IEEE Trans. Pattern Anal. and Machine Intelligence*, vol. 28, no. 11, pp. 1–17, November 2006.

[40] V. Grau, A. U. J. Mewes, M. Alcaniz, R. Kikinis, and S. K. Warfield, "Improved watershed transform for medical image segmentation using prior information," *IEEE Trans. Med. Imaging*, vol. 23, no. 4, pp. 447–458, 2004.

[41] M. Haeker, X. Wu, M. Abramoff, R. Kardon, and M. Sonka, "Incorporation of regional information in optimal 3-D graph search with application for intraretinal layer segmentation of optical coherence tomography images," in *Information Processing in Medical Imaging*, vol. 4584. Springer, July 2007, pp. 607–618.

[42] D. Han, M. Sonka, J. Bayouth, and X. Wu, "Optimal multiple-seams search for image resizing with smoothness and shape prior," *The Visual Computer*, 2010, available online.

[43] R. M. Haralick, K. Shanmugam, and I. Dinstein, "Textural features for image classification," *IEEE Trans. Systems, Man, and Cybernetics*, vol. SMC-3, no. 6, pp. 610–621, 1973.

[44] Y. Hata, S. Kobashi, Y. Tokimoto, M. Ishikawa, and H. Ishikawa, "Computer aided diagnosis system of meniscal tears with T1 and T2 weighted MR images based on fuzzy inference," in *Computational Intelligence. Theory and Applications*, ser. Lecture Notes in Computer Science, vol. 2206. Springer, January 2001, pp. 55–58.

[45] T. Heimann, S. Munzing, H. Meinzer, and I. Wolf, "A shape-guided deformable model with evolutionary algorithm initialization for 3D soft tissue segmentation," in *Information Processing in Medical Imaging*, ser. Lecture Notes in Computer Science, vol. 4584. Springer, July 2007, pp. 1–12.

[46] D. J. Hunter, J. Niu, Y. Zhang, S. Totterman, J. Tamez, C. Dabrowski, R. Davies, M. H. L. Graverand, M. Luchi, Y. Tymofyeyev, and C. R. Beals, "Change in cartilage morphometry: a sample of the progression cohort of the osteoarthritis initiative," *Ann Rheum Dis.*, vol. 13, 2008.

[47] D. J. Hunter, Y. Q. Zhang, X. Tu, M. LaValley, J. B. Niu, S. Amin, A. Guermazi, H. Genant, D. Gale, and D. T. Felson, "Change in joint space width: Hyaline articular cartilage loss or alteration in meniscus?" *Arthritis & Rheumatism*, vol. 54, 2006.

[48] I. T. Jolliffe, *Principal Component Analysis (2nd ed.)*, ser. Springer Series in Statistics. Springer, 2002.

[49] D. Kainmueller, H. Lamecker, S. Zachow, M. Heller, and H. Hege, "Multi-object segmentation with coupled deformable models," in *Proc. of Medical Image Understanding and Analysis*, 2008, pp. 34–38.

[50] T. Kapur, P. A. Beardsley, S. F. Gibson, W. E. L. Grimson, and W. M. Wells, "Model based segmentation of clinical knee MRI," in *Proc. IEEE Intl. workshop on Model-Based 3D Image Analysis*, 1998, pp. 98–106.

[51] J. H. Kellgren and J. S. Lawrence, "Radiological assessment of osteo-arthrosis," in *Ann. rheum. Dis.*, vol. 16, 1957, pp. 494–502.

[52] R. Kindermann and J. L. Snell, Eds., *Markov Random Fields and Their Applications*. American Mathematical Society, 1980.

[53] T. Klinder, C. Lorenz, and J. Ostermann, "Free-breathing intra-and intersubject respiratory motion capturing, modeling, and prediction," in *Proc. SPIE*, vol. 7259, 2009, p. 72590T.

[54] V. Kolmogorov and R. Zabih, "What energy functions can be minimized via graph cuts?" *IEEE Trans. Pattern Anal. and Machine Intelligence*, vol. 26, no. 2, pp. 147–159, 2004.

[55] L. König, M. Groher, A. Keil, C. Glaser, M. Reiser, and N. Navab, "Semiautomatic segmentation of the patellar cartilage in MRI," in *Bildverarbeitung fur die medizin*, ser. Informatik aktuell. Springer, 2007, pp. 404–408.

[56] C. Köse, O. Gencalioglu, and U. Sevik, "An automatic diagnosis method for the knee meniscus tears in MR images," *Expert Systems with Applications*, vol. 36, no. 2, pp. 1208–1216, 2009.

[57] F. Kruggel, "Robust parametrization of brain surface meshes," *Medical Image Analysis*, vol. 12, no. 3, pp. 291–299, June 2008.

[58] J. Lafferty, A. McCallum, and F. Pereira, "Conditional random fields: Probabilistic models for segmenting and labeling sequence data," in *Proc. 18th International Conf. on Machine Learning*, 2001, pp. 282–289.

[59] K. Lee, R. K. Johnson, Y. Yin, A. Wahle, M. E. Olszewski, T. D. Scholz, and M. Sonka, "Three-dimensional thrombus segmentation in abdominal aortic aneurysms using graph search based on a triangular mesh," *Computers in Biology and Medicine*, vol. 6916, no. 3, pp. 271–278, 2010.

[60] K. Li and M. P. Jolly, "Simultaneous detection of multiple elastic surfaces with application to tumor segmentation in ct images," in *Proc. SPIE*, vol. 6914, 2008, pp. 69 143S–69 143S–11.

[61] K. Li, S. Millington, X. Wu, D. Z. Chen, and M. Sonka, "Simultaneous segmentation of multiple closed surfaces using optimal graph searching," in *Information Processing in Medical Imaging*, vol. 3565. Springer, July 2005, pp. 406–417.

[62] K. Li, X. Wu, D. Z. Chen, and M. Sonka, "Optimal surface segmentation in volumetric images – a graph-theoretic approach," *IEEE Trans. Pattern Anal. and Machine Intelligence*, vol. 28, no. 1, pp. 119–134, January 2006.

[63] H. Ling, S. K. Zhou, Y. Zheng, B. Georgescu, M. Suehling, and D. Comaniciu, "Hierarchical, learning-based automatic liver segmentation," in *Computer Vision and Pattern Recognition (CVPR)*, 2008, pp. 1–8.

[64] A. Litvin and C. Karl, "Coupled shape distribution-based segmentation of multiple objects," in *Information Processing in Medical Imaging*, ser. Lecture Notes in Computer Science, vol. 3565. Springer, July 2005, pp. 345–356.

[65] X. Liu, D. Z. Chen, X. Wu, and M. Sonka, "Optimal graph search based image segmentation for objects with complex topologies," in *SPIE Medical Imaging*, vol. 7259, 2009, p. 725915.

[66] C. Lorenz and J. Berg, "A comprehensive shape model of the heart," *Medical Image Analysis*, vol. 10, pp. 657–670, August 2006.

[67] J. A. Lynch, S. Zaim, J. Zhao, C. G. Peterfy, and H. K. Genant, "Automating measurement of subtle changes in articular cartilage from MRI of the knee by combining 3D image registration and segmentation," in *Proc. SPIE*, vol. 4322, 2001, pp. 431–439.

[68] J. A. Lynch, S. Zaim, J. Zhao, A. Stork, C. G. Peterfy, and H. K. Genant, "Cartilage segmentation of 3D MRI scans of the osteoarthritic knee combining user knowledge and active contours," in *Proc. SPIE*, 2000, pp. 925–935.

[69] J. MacQueen, "Some methods for classification and analysis of multivariate observations," in *Proc. Fifth Berkeley Symp. on Math. Statist. and Prob.*, 1967, pp. 281–297.

[70] J. Montagnat, H. Delingette, and G. Mal, "Cylindrical echocardiographic images segmentation based on 3D deformable models," in *International Conference on Medical Image Computing and Computer Assisted Intervention (MICCAI)*, 1999, pp. 168–175.

[71] T. Ojala, M. Pietikäinen, and T. Mäenpää, "Multiresolution gray-scale and rotation invariant texture classification with local binary patterns," *IEEE Trans. Pattern Anal. and Machine Intelligence*, vol. 24, no. 7, pp. 971–987, 2002.

[72] C. G. Peterfy, A. Guermazi, S. Zaim, P. F. J. Tirman, Y. Miaux, D. White, M. Kothari, Y. Lu, K. Fye, S. Zhao, and H. K. Genant, "Whole-organ magnetic resonance imaging score (worms) of the knee in osteoarthritis," in *Osteoarthritis and Cartilage*, vol. 12, 2004, pp. 177–190.

[73] C. G. Peterfy, E. Schneider, and M. Nevitt, "The osteoarthritis initiative: Report on the design rationale for the magnetic resonance imaging protocol for the knee," in *Osteoarthritis and Cartilage*, vol. 16, 2008, pp. 1433–1441.

[74] M. E. Petersen, D. Ridder, and H. Handels, "Image processing with neural networks - a review," *Pattern Recognition*, vol. 35, no. 10, pp. 2279–2301, 2002.

[75] C. D. Pirnog, "Articular cartilage segmentation and tracking in sequential MR images of the knee," Ph.D. dissertation, ETH Zurich, 2005.

[76] J. Quinlan, "Induction of decision trees," *Machine Learning*, vol. 1, no. 1, pp. 81–106, 1986.

[77] S. J. Rahi and K. Sharp, "Mapping complicated surface onto a sphere," *International Journal of Computational Geometry and Applications*, vol. 17, no. 4, pp. 305–329, 2007.

[78] B. Ramakrishna, W. Liu, N. M. Safdar, K. M. Siddiqui, W. Kim, K. Juluru, C. Chang, and E. L. Siegel, "Automatic CAD of meniscal tears on MR imaging: a morphology-based approach," in *Proc. SPIE*, vol. 6514, 2007, p. Paper ID 651437.

[79] J. P. Raynauld, C. Kauffmann, G. Beaudoin, M. J. Berthianume, J. A. Guise, D. A. Bloch, F. Camacho, B. Godbout, R. D. Altman, M. Hochberg, J. M. Meyer, G. Cline, J. P. Pelletier, and J. M. Pelletier, "Reliability of a quantification imaging system using magnetic resonance images to measure cartilage thickness and volume in human normal and osteoarthritic knees," *Osteoarthritis and Cartilage*, vol. 11, 2003.

[80] T. Rohlfing and C. R. M. Jr., "Multi-classifier framework for atlas-based image segmentation," in *Pattern Recognition Letters*, vol. 26. Elsevier, October 2005, pp. 2070–2079.

[81] A. Saragaglia, C. Fetita, and F. Preteux, "Assessment of airway remodeling in asthma: Volumetric versus surface quantification approaches," in *International Conference on Medical Image Computing and Computer Assisted Intervention (MICCAI)*, 2006, pp. 413–420.

[82] S. Solloway, C. Hutchinson, J. Waterton, and C. Taylor, "The use of active shape models for making thickness measurements of articular cartilage from MR images," *Magnetic Resonance in Medicine*, vol. 37, no. 6, 1997.

[83] S. Solloway, C. J. Taylor, C. E. Hutchinson, and J. C. Waterton, "Quantification of articular cartilage from MR images using active shape models," in *4th European Conference on Computer Vision*, 1996, pp. 400–411.

[84] Q. Song, X. Wu, Y. Liu, M. Smith, J. Buatti, and M. Sonka, "Optimal graph search segmentation using arc-weighted graph for simultaneous surface detection of bladder and prostate," in *International Conference on Medical Image Computing and Computer Assisted Intervention (MICCAI)*, vol. 5762, 2009, pp. 827–835.

[85] M. Sonka and J. M. Fitzpatrick, Eds., *Handbook of Medical Imaging, Volume 2: Medical Image Processing and Analysis*. SPIE–The International Society for Optical Engineering, 2000.

[86] M. Sonka, V. Hlavac, and R. Boyle, *Image Processing, Analysis, and Machine Vision (3rd ed.)*. Thomson Engineering, 2008.

[87] M. S. Swanson, J. W. Prescott, T. M. Best, K. Powell, R. D. Jackson, F. Haq, and M. N. Gurcan, "Semi-automated segmentation to assess the lateral meniscus in normal and osteoarthritic knees," *Osteoarthritis and Cartilage*, vol. 18, pp. 344–353, 2010.

[88] J. G. Tamez-Pena, M. Barbu-Mclnnis, and S. Totterman, "Unsupervised definition of the tibia-femoral joint regions of the human knee and its applications to cartilage analysis," in *Proc. SPIE*, vol. 6144, 2006, pp. 1465–1475.

[89] J. G. Tamez-Pena, S. Totterman, and K. J. Parker, "Unsupervised statistical segmentation of multispectral volumetric MR images," in *SPIE Medical imaging*, vol. 3661, 1999, pp. 300–311.

[90] P. Viola and M. Jones, "Robust real-time face detection," *International Journal of Computer Vision*, vol. 57, no. 2, pp. 137–154, 2004.

[91] S. Wang, W. Zhu, and Z. Liang, "Shape deformation: SVM regression and application to medical image segmentation," in *IEEE International Conference on Computer Vision (ICCV)*, 2001, pp. 209–216.

[92] S. K. Warfield, M. Kaus, F. A. Jolesz, and R. Kikinis, "Adaptive, template moderated, spatially varying statistical classification," in *Medical Image Analysis*. Springer, 2000, pp. 43–55.

[93] T. G. Williams, A. P. Holmes, J. C. Waterton, R. A. Maciewicz, C. E. Hutchinson, R. J. Moots, A. F. P. Nash, and C. J. Taylor, "Anatomically corresponded regional analysis of cartilage in asymptomatic and osteoarthritic knees by statistical shape modelling of the bone," *IEEE Trans. Med. Imaging*, p. In Press, 2010.

[94] W. Wirth, M. H. L. Graverand, B. Wyman, S. Maschek, M. Hudelmaier, W. Hitzl, M. Nevitt, and F. Eckstein, "Regional analysis of femorotibial cartilage loss in a subsample from the osteoarthritis initiative progression subcohort," *Osteoarthritis and Cartilage*, vol. 17, 2008.

[95] X. Wu and D. Z. Chen, "Optimal net surface problem with applications," in *Proc. of the 29th International Colloquium on Automata, Languages and Programming (ICALP)*, ser. Lecture Notes in Computer Science, vol. 2380. Springer, July 2002, pp. 1029–1042.

[96] X. Wu, X. Dou, J. E. Bayouth, and J. M. Buatti, "Efficient algorithm for optimal matrix orthogonal decomposition problem in intensity-modulated radiation therapy," *Int. J. Comput. Geometry Appl.*, vol. 19, no. 3, pp. 231–246, 2009.

[97] Z. Xie, J. T. Pena, M. Gieseg, S. Liachenko, S. Dhamija, and P. Chiao, "Segmentation by surface-to-image registration," in *Proc. SPIE*, vol. 6144, 2006, p. Paper ID 614405.

[98] Z. Yi, A. Criminisi, J. Shotton, and A. Blake, "Discriminative, semantic segmentation of brain tissue in MR images," in *International Conference on Medical Image Computing and Computer Assisted Intervention (MICCAI)*, 2009, pp. 558–565.

[99] Y. Yin, Q. Song, and M. Sonka, "Electric field theory motivated graph construction for optimal medical image segmentation," in *7th IAPR-TC-15 Workshop on Graph-based Representations in Pattern Recognition*, 2009, pp. 334–342.

[100] Y. Yin and M. Sonka, "Electric field theory based approach to search-direction line definition in image segmentation: application to optimal femur-tibia cartilage segmentation in knee-joint 3d mr," in *SPIE Medial Imaging*, 2010, pp. 7623–31.

[101] Y. Yin, X. Zhang, D. D. Anderson, T. D. Brown, C. V. Hofwegen, and M. Sonka, "Simultaneous segmentation of the bone and cartilage surfaces of a knee joint in 3D," in *SPIE Medical Imaging*, vol. 7258, 2009, p. 72591O.

[102] Y. Yin, X. Zhang, and M. Sonka, "Fully three-dimensional segmentation of articular cartilage performed simultaneously in all bones of the joint," in *Osteoarthritis and Cartilage*, vol. 15(3), 2007, p. C177.

[103] ——, "Optimal multi-object multi-surface graph search segmentation: Full-joint cartilage delineation in 3D," in *Proc. of Medical Image Understanding and Analysis*, 2008, pp. 104–108.

[104] H. Zhang, "Segmentation and computer-aided diagnosis of cardiac MR images using 4-D active appearance models," Ph.D. dissertation, The University of Iowa, Iowa City, Iowa, USA, 2007.

[105] F. Zhao, H. Zhang, A. Wahle, M. Thomas, A. Stolpen, T. Scholz, and M. Sonka, "Congenital aortic disease: 4D magnetic resonance segmentation and quantitative analysis," *Medical Image Analysis*, vol. 13, no. 3, pp. 483–93, 2009.

[106] F. Zhao, H. Zhang, N. E. Walker, F. Yang, M. E. Olszewski, A. Wahle, T. Scholz, and M. Sonka, "Quantitative analysis of two-phase 3D+time aortic MR images," in *SPIE Medical Imaging*, vol. 6144, 2006, pp. 699–708.

[107] Y. Zheng, A. Barbu, B. Georgescu, M. Scheuering, and D. Comaniciu, "Fast automatic heart chamber segmentation from 3d CT data using marginal space learning and steerable features," in *IEEE International Conference on Computer Vision*, 2007, pp. 1–8.